

**Far-ultraviolet Imaging Rocket Experiment (FIRE) and the  
imaging of star-forming regions in galaxies**

by

**Brennan L. Gantner**

B.S., Engineering Physics, Santa Clara University, 1999

M.S., Astrophysics, University of Colorado: Boulder, 2007

A thesis submitted to the  
Faculty of the Graduate School of the  
University of Colorado in partial fulfillment  
of the requirements for the degree of  
Doctor of Philosophy  
Department of Astrophysical and Planetary Sciences

2012

This thesis entitled:  
Far-ultraviolet Imaging Rocket Experiment (FIRE) and the imaging of star-forming regions in  
galaxies  
written by Brennan L. Gantner  
has been approved for the Department of Astrophysical and Planetary Sciences

---

Prof. James Green

---

Prof. John Stocke

---

Dr. Matthew Beasley

Date \_\_\_\_\_

The final copy of this thesis has been examined by the signatories, and we find that both the content and the form meet acceptable presentation standards of scholarly work in the above mentioned discipline.

Gantner, Brennan L. (Ph.D., Astrophysics)

Far-ultraviolet Imaging Rocket Experiment (FIRE) and the imaging of star-forming regions in galaxies

Thesis directed by Prof. Prof. James Green

I designed, built, tested and launched a sounding rocket payload to study the far-ultraviolet radiation of M51 (the Whirlpool Galaxy). This instrument, the Far-ultraviolet Imaging Rocket Experiment (FIRE, all acronyms are listed in Appendix B), produced the first ever astronomical image of 900-1000 Å light. It was designed to look at star forming regions in nearby galaxies by imaging the youngest, hottest O-type stars. Quantifying and locating the star forming regions within galaxies will directly aid galactic formation models. In addition, with the combination of the GALEX two-color images, FIRE was designed to investigate the intervening dust that significantly obscures these wavelengths. Since the accurate correction for dust is vital to measurements across the ultraviolet regime, improving dust extinction models aids a wide variety of both galactic and extra-galactic observations. Finally, FIRE demonstrated the successful use of two novel technologies, a silicon carbide imaging mirror and a pure indium filter.

In addition to FIRE, I also examined the absorption of neutral hydrogen in the intergalactic medium (IGM) along quasi-stellar objects (QSO) sightlines. The IGM is expected to contain a significant fraction of baryons at all epochs, but is difficult to detect and map since it is diffuse and emits radiation weakly. An ongoing IGM debate is whether clouds of gas detected through their Ly $\alpha$  absorption to QSOs are truly intergalactic or are extended halos of galaxies. A definitive answer would constrain estimates of baryonic density in the local universe and enhance our understanding of the formation of its structure. The CfA Great Wall of galaxies at redshifts of  $0.015 < z < 0.03$  offers an excellent locale to probe this question. This region is over-dense in galaxies and is surrounded by under-dense galactic voids, enabling us to compare absorbers' nearest galactic neighbors in highly contrasting density regions. I found 167 Ly $\alpha$  absorbers along eleven QSO sightlines and

used a galaxy database to examine the Ly $\alpha$  absorber-galaxy relationship. I compare these results to previous publications and determine that Ly $\alpha$  absorbers and galaxies cannot trace the same large-scale structures at the megaparsec scale.

## Dedication

*[It's] time for the human race to enter the solar system.*

– Vice President Dan Quayle

A rocket program is not just a scientific project, but a life choice for several years. And as such, other life commitments can sometimes get jealous. As well they should I say; odds are they won't hit Mach 7 anytime soon.

Thank you for waiting Kim. ...again...

## Acknowledgements

A sounding rocket project is the culmination of so many people's effort it is impossible to acknowledge everyone involved. However, numerous individuals and groups were truly indispensable to getting FIRE off the ground. Foremost was the VP of West Coast operations, Bobby "Work-wife" Kane. Other CU standouts were Mike "Pancake Dinner" Kaiser, Ted "The Neard" Schultz, Scott "Impossible" MacDonald, Dr. Matt Beasley and, of course, Dr. Jim Green for this opportunity. Around Boulder, the Hodgesons and JILA were crucial not only in making parts, but making part designs better. Of course, Dr. Oswald Siegmund saved us in a pressure situation, as he seems to do for every Colorado rocket. In Virginia, the NSROC team was led by some great individuals. Notably, Nic Cranor, a mission manager extraordinaire. Also crucial were Christian Amey, Eric Taylor, Gary Sneed, Charlie Kapelian, Keith Foster, Charlie Cathell, Danny Bowden, Cliff Murphy and Mackenzie Rennolet. In Alaska, Greg Walker and Kathe Rich made a trip to the frozen north an amazing experience. And finally, I know there were so many people behind the scenes that rarely get mentioned, but without them the rocket never flies. So for anyone not listed here, thank you.

Of course there was another half to this thesis. Hardy thank you's to Dr. John Stocke, Dr. Steven Penton and Dr. Charles Danforth for helping me through learning a whole new field so fast.

I owe my family a debt I can never repay. Thank you to my friends making life in Boulder so amazing. Thank you to so many teachers that kept pushing me to be better.

Finally, to the Chicken Pesto burrito. You kept me sane and full and this thesis is as much yours as mine. You are missed...

## Contents

Chapter	
<b>1</b> Star Formation in Nearby Galaxies	1
1.1 Star formation in galaxies . . . . .	1
<b>2</b> Far-Ultraviolet Imaging Rocket Experiment	8
2.1 Payload Overview and Mirror Design . . . . .	8
2.2 Canister Design . . . . .	14
2.3 Indium Filters . . . . .	19
2.3.1 Initial Results . . . . .	20
2.3.2 Plasma Cleaning . . . . .	21
2.3.3 Flight Filters . . . . .	22
2.4 Detector . . . . .	22
2.5 Pre-flight Expectations . . . . .	26
2.6 In-flight Specifics . . . . .	28
2.7 Post-flight Conclusions and Results . . . . .	31
2.8 FIRE summary . . . . .	36
<b>3</b> Ly $\alpha$ absorbers and nearby galaxies	38
3.1 Introduction to Ly $\alpha$ absorption in QSO sightlines . . . . .	38
3.2 Ly $\alpha$ absorption and galaxies . . . . .	42
3.2.1 Great Wall of galaxies . . . . .	42

3.2.2	Galaxy database . . . . .	43
3.2.3	COS spectra . . . . .	45
3.3	COS Data Reduction . . . . .	46
3.3.1	Co-adding Spectra, Continuum Fitting . . . . .	47
3.3.2	Noise and searching for absorption features . . . . .	47
3.3.3	Identifying galactic sources and multiple component absorbers . . . . .	49
<b>4</b>	<b>Analysis of Ly<math>\alpha</math> absorbers and their nearby galaxies</b>	<b>53</b>
4.1	The Ly $\alpha$ absorber population . . . . .	53
4.1.1	Ly $\alpha$ absorber column densities and evolution with redshift . . . . .	56
4.1.2	Two-point Correlation Function . . . . .	57
4.2	Hits and Misses in the Great Wall . . . . .	60
4.2.1	Expanding virial radii . . . . .	65
4.3	Ly $\alpha$ absorber and galaxy populations . . . . .	67
4.3.1	Ly $\alpha$ absorbers normalized . . . . .	67
4.3.2	Galaxies normalized . . . . .	68
4.3.3	Ly $\alpha$ absorber and galactic densities discussion . . . . .	69
4.4	Examination of Ly $\alpha$ absorbers and their nearest galactic neighbor . . . . .	74
4.4.1	Nearest galactic neighbor discussion . . . . .	80
4.5	Future work . . . . .	83
	<b>Bibliography</b>	<b>86</b>
	<b>Appendix</b>	
<b>A</b>	<b>COS spectra and Ly<math>\alpha</math> absorbers</b>	<b>89</b>
<b>B</b>	<b>Acronym list</b>	<b>107</b>

**C** Nearest Galaxy Neighbor List

## Tables

### Table

3.1	A list of the QSO sightlines used and their availability in UV spectra before COS. . . . .	46
3.2	A list of the galactic lines removed from the spectra. Higher Lyman series lines (Ly $\beta$ , Ly $\gamma$ , etc.) can be present but are not listed here. . . . .	50
3.3	A list of the Lyman and metal lines that I searched for at the same redshift as each Ly $\alpha$ absorber system. They are ordered from most likely to least likely to occur on a typical absorption feature. Higher order Lyman lines were checked when Ly $\beta$ or Ly $\gamma$ were present but are not listed here. . . . .	52
4.1	A comparison of Ly $\alpha$ absorbers found on QSO sightline PG1116+215 for this study, Penton et al. (2004), and Sembach et al. (2004). Note: Sembach et al. (2004) did not list SL, so their $\mathscr{W}$ is listed instead. . . . .	54

- 4.2 The number of “hits” of Ly $\alpha$  absorbers falling within the specified limits of the Great Wall along the QSO sightlines with the furthest extent of the Great Wall limited to 7000 km/sec. The results for all eleven sightlines are shown on the left, while a subset of the nine tightly grouped sightlines are shown on the right. Also shown are the results of a Monte Carlo uniform random population with the same restrictions and measurements. The results are split along the three definitions of the Great Wall range for each sightline. The peak is the maximum number of galaxies found for each sightline within  $0.015 < z < 0.035$ , while the percentages give the extent of the range by again following the number of galaxies and ending when the galaxy number drops below the peak value. The errors shown on the random samples are the  $1\sigma$  values of the gaussian distributed results. . . . . 65
- 4.3 The number of hits using the same Great Wall extent definitions (see Table 4.2) for nine random sightlines (repeated 1,000 times and averaged) within the same region of space as the grouped nine QSO sightlines. “Hits” are determined by stepping along the sightline and examining each galaxy nearby. If that galaxy is less than the number of virial radii away for that cutoff regime (left column), then it is a “hit”. Thus, the larger the number of virial radii allowed, the higher the covering factor. Starred rows are the virial radii cutoffs that produce the same number of hits as the actual measurement of the nine QSO sightlines (final row, taken from Table 4.2). As before, the restriction of the Great Wall extent does not change the end results much. This table shows that  $0.5 L_{\star}$  (and greater) galaxies would need material at 6-9 virial radii away dense enough to produce a absorption feature of  $Log(N_{HI}) > 12.9$  to match the results found in the actual measurement. In addition, a cutoff of  $0.25 L_{\star}$  is also shown. While a portion of the space ( $\approx 33\%$ ) examined is not complete to  $0.25 L_{\star}$  (the entire region is complete to  $0.5 L_{\star}$ ), this does not show a significant change in the number of virial radii needed for the same covering factor. . . . . 66

4.4	The Pearson correlation coefficient for subsets of the Ly $\alpha$ absorber-galaxy dataset. The absorbers are split into weak and strong column densities by $\text{Log}(N_{HI})= 13.0$ and the population is limited by the galactic criteria $0.1L_*$ , $0.5L_*$ and $L_*$ . The left half of the table uses Ly $\alpha$ absorbers that had a galaxy within the $3 h_{70}^{-1}$ Mpc cutoff and correlates between $N_{HI}$ and nearest neighbor galactic distance. The right half of the table are the opposing void absorbers that had no galaxy within $3 h_{70}^{-1}$ Mpc. For these, since there is no galactic distance, the correlation is between column density and the number of void absorbers in $\Delta\text{Log}(N_{HI})=0.2$ bins. The values in parentheses are the number of Ly $\alpha$ absorbers in each subset. . . . .	80
A.1	A list of all the Ly $\alpha$ absorbers identified in this study. The $\mathscr{W}$ listed is the measured equivalent width, not the rest frame equivalent width. . . . .	102
A.2	A list of all the Ly $\alpha$ absorbers identified in this study (continued). . . . .	103
A.3	A list of all the Ly $\alpha$ absorbers identified in this study (continued). . . . .	104
A.4	A list of all the Ly $\alpha$ absorbers identified in this study (continued). . . . .	105
A.5	A list of all the Ly $\alpha$ absorbers identified in this study (continued). . . . .	106
B.1	A list of acronyms used in this thesis. . . . .	107
C.1	A list of all Ly $\alpha$ absorbers and their nearest galactic neighbor. . . . .	109
C.2	A list of all Ly $\alpha$ absorbers and their nearest galactic neighbor (Continued). . . . .	110
C.3	A list of all Ly $\alpha$ absorbers and their nearest galactic neighbor (Continued). . . . .	111
C.4	A list of all Ly $\alpha$ absorbers and their nearest galactic neighbor (Continued). . . . .	112
C.5	A list of all Ly $\alpha$ absorbers and their nearest galactic neighbor (Continued). . . . .	113

## Figures

### Figure

- 1.1 An averaged attenuation curve of the Milky Way galaxy in color magnitudes versus wavelength (reprinted from Fitzpatrick, 2004). The solid lines represent measured data, while the dashed lines are predicted values for unobserved regions of the spectrum. Notice the increasing attenuation with shorter wavelengths and the lack of data of wavelengths shorter than  $\approx 1150 \text{ \AA}$ . . . . . 3
- 1.2 Attenuation between pairs of stars within M31 (reprinted from Bianchi et al., 1996). As in Figure 1.1, the attenuation of signal rises sharply in the FUV. My instrument would add additional data points to similar measurement at  $1/\lambda \approx 10.5$  on this scale. 6
- 1.3 M51 (the Whirlpool galaxy) in visible light taken by the Hubble Space Telescope. Produced under NASA contract NAS5-26555. . . . . 7
- 2.1 The FIRE primary mirror installed within the telescope (bottom left, identified by the 5 inch hole in its center). . . . . 10
- 2.2 The FIRE telescope cutaway drafting model. Note the mirror in the upper left and the internal skins (14 inches diameter) and external skins (17.25 inches diameter) and the electronics (red boxes) that fit in the space between them. The grey bars that run along the internal skin are the lexan “safety rails” that protect wires and electronics during assembly. The vacuum canister discussed in §2.2 is hidden within the inner skin behind the red electronic boxes. . . . . 11

2.3	The final focus results for FIRE. Notice the residual coma that could not be corrected for in alignment. The final precision of this instrument was 8 arcseconds per resolution element. . . . .	12
2.4	The reflectance of silicon carbide across the FUV wavelengths. The dots show a long duration study of its reflectance, 8.5 years. Silicon carbide has an average reflectance of 40% across the telescope's 900-1000 Å passband. Plot reprinted from Keski-Kuha et al. (1995). . . . .	13
2.5	One of the indium filters used in FIRE. . . . .	15
2.6	A cross-section of the space available that was not in the telescope's light path. In this view, the light enters from the bottom and the mirror is above focusing light back downward. The yellow annulus shows the incoming unfocused light that would be moderately harmful to block, while the red cone shows the focused light that would be extremely detrimental to block. The remaining space, a cylinder five inches across, had to contain the detector, filter, star tracker, vacuum pump, vacuum canister, canister door opening/closing mechanism and all accompanying wires. The measurements shown are of the diameter of the mirror (13.291 inches) and the canister system (5.288 inches), thus the canister extends 0.144 inches into the interior edge of the incoming lightpath. See Figure 2.8 for the entire canister system upon completion. . . . .	17
2.7	Wax actuator used as the motor power to close the canister vacuum door in pre-flight preparations. See Figure 2.8 for placement on the canister. . . . .	18
2.8	The vacuum canister that holds the detector and indium filter. The model on the left shows the wax actuators (tubes on lower right), vacuum door (top right) and detector (at base of yellow light cone in center). The real image on the right shows the door more clearly (top), the solenoid that opens the door (center left) and the ion pump (box back left with single large cable). . . . .	20

2.9	Transmission of first indium filter produced for FIRE. Note that in contrast to the final flight filter and the theoretical filter from Figure 2.10, this filter is only 1000 Å thick, making its transmission even worse in comparison. The goal was 10% transmission at 900 Å. . . . .	21
2.10	Transmission of the flight filter for FIRE, as well as the theoretical transmission for a 2000 Å thick filter and an early FIRE filter (pre-plasma cleaning) for comparison. While the goal was a 2000 Å thick filter, the fact that the Ly $\alpha$ transmission is higher than predicted indicates the filter is thinner than 2000 Å. . . . .	23
2.11	An example of the process of charge multiplication in a MCP. Electrons strike the walls of the pores, leading to more electrons being released and a cascade event that results in increased signal. . . . .	24
2.12	The quantum efficiency of a RbBr photocathode in a MCP detector (red line) (Siegmund, 2009). . . . .	25
2.13	The recorded response of the initial detector MCPs when recording collimated radiation through a circular 10 $\mu\text{m}$ pinhole; each pixel is 25 $\mu\text{m}$ . The elongation occurs in the direction of the pore bias and was seen across all the Hamamatsu plates I obtained. . . . .	27
2.14	Expected counts for M51 (top) and the expected S/N (bottom) during the first flight of FIRE. This is based on a combination of previous spectra taken in our wavelength range with other UV images from GALEX and the efficiencies of the FIRE system. . . . .	29
2.15	The recorded +28V instrument main power line monitor (left) in digital numbers (DN) and the current monitor on the same line (right). The anomaly start (77 sec) and stop (553 sec) times are marked as well as the high voltage system on/off. . . . .	32
2.16	The recorded +5V instrument monitor in digital numbers (DN) during flight, with the start and stop times of the anomaly marked (left) and the altitude of the payload versus time, again with the anomaly and high voltage systems marked (right). . . . .	33

- 2.17 FIRE flight image of the B3 star Alkaid, the first ever astronomical image from 900-1000Å. Artifacts from the voltage ripple are apparent in the blocks around the star, the streaks leading down and left, as well as the blurring of the star itself. . . . . 35
- 2.18 The counts per second for the end of the FIRE flight (top) and the attenuation of UV signal as a function of altitude (bottom). Region A marks the majority of the flight with a stable count rate. B shows the attenuation effects, dropping the count rate to zero at C. The spike upward at D shows the detector has enough ambient atmosphere to arc and helpfully demonstrates that the system was still working at this time. . . . . 37
- 3.1 A map of the local universe with nearby galaxies drawn from Dr. Penton’s database. Solid lines show the sightlines to the 11 QSO under study. Each galaxy in the CfA catalog is designated by a “c”, while each galaxy unique to the Sloan catalog is denoted by an “s”. The redshift analysis range,  $0.0035 < z < 0.07$ , is equivalent to  $1,050 < cz < 21,000$  km/second. The CfA Great Wall stretches from approximately 10,000 km/sec on the left, down through the middle to 6,000 km/sec in the lower right. Note the regions of low galactic density (voids) in the lower left, lower middle, upper left and upper right. Note: the declination wedge shown does not cover every sightline drawn on the plot. . . . . 44
- 3.2 A sky map of the QSO sightlines and the galaxies within the 3 Mpc cylinder with them (red dots). Each sightline is labeled with the number of Ly $\alpha$  absorbers in parentheses. Ton236 is left off the plot for scaling reasons. . . . . 46

- 3.3 The  $0.0035 < z < 0.07$  (1220-1300 Å) range of the HS1102+3441 spectrum. Solid green vertical lines mark (and are labeled) Ly $\alpha$  absorbers, while dashed blue lines (also labeled) mark other Lyman or metal lines from Ly $\alpha$  absorber systems at higher redshifts. Ly $\alpha$  absorber green lines with a red marker at the bottom are “marginal” ( $3\sigma < SL < 4\sigma$ ). Red dashed and dotted vertical lines show the location of common galactic absorption lines, which are not always present. The red continuum fit is augmented by the voigt profile fit of each absorber. Finally, each non-Ly $\alpha$  feature is surrounded by a yellow box that denotes the region in which a Ly $\alpha$  absorber could not be found due to the obscuration. Note the large number of non-Ly $\alpha$  absorbers within the target wavelength region. Without the extended coverage of COS to larger wavelengths, absorption features such as these may be spuriously labeled Ly $\alpha$  and distort the population. The same plot for each QSO absorber can be found in the appendix. . . . . 51
- 4.1 The distribution of rest frame equivalent widths ( $\mathscr{W}$ , top), doppler parameters ( $b$ , center) and column densities ( $N_{HI}$ , bottom) in the Ly $\alpha$  absorber population. Note: two equivalent widths (767.26 and 1977.28 mÅ) and one column density ( $\text{Log}(N_{HI})=18.75$ ) have been left off their respective plots for scaling purposes. . . . . 55
- 4.2 The distribution of column densities ( $N_{HI}$ ) in the Ly $\alpha$  absorber population per unit redshift and column density,  $n(N_{HI}) = \int \int (\partial^2 \mathcal{N} / \partial z \partial N_{HI}) dz dN_{HI}$ . The absorber population is truncated below  $\text{Log}(N_{HI}) < 12.9$  to adjust for the limiting detection sensitivity of the spectra. The fit to this data (black) is compared to the fit to Penton et al. (2004) data (red). . . . . 57

- 4.3 The distribution of  $b$  (top) and  $N_{HI}$  (bottom) versus redshift. Absorbers have been split into strong ( $\text{Log}(N_{HI}) > 13.0$ ) and weak ( $\text{Log}(N_{HI}) < 13.0$ ) based on the median value of the population ( $\text{Log}(N_{HI}) = 13.01$ ) marked with the red dashed line. Note: One column density point (PG0832 1236.9Å) has been left off the bottom plot for scaling purposes. . . . . 58
- 4.4 The Two-Point Correlation Function (TPCF) for the number of pairs of observed absorbers (black) and a random population (red) against velocity separation ( $\Delta v$ ) bins of 100 km/sec. The red and blue dashed lines represent the  $1\sigma$  and  $2\sigma$  limits respectively. When bin sizes other than 100 km/sec are used, the spike at  $\approx 15,000$  km/sec drops to near or below the  $2\sigma$  cutoff. . . . . 61
- 4.5 The same data as Figure 4.4 on a log scale (left) and the same measurement taken by Penton et al. (2000a) (right) (a subset of the Penton et al. (2004) data). Penton et al. (2000a) shows an excess of pairs  $\Delta v < 500$  km/sec, while my data has no significant excess at any separation. . . . . 61
- 4.6 The Two-Point Correlation Function (TPCF)  $\xi$  for the data presented in Figure 4.4. The red dashed line emphasizes the value where the random and observed populations match in the  $\xi$  function. The red and blue lines represent the  $1\sigma$  and  $2\sigma$  significance level cutoff respectively of each bin. While the values above  $\approx 14,000$  km/sec appear large, they are dominated by low number statistics and none passes the  $2\sigma$  confidence level. . . . . 62
- 4.7 TPCF  $\xi$  function for all strong Ly $\alpha$  absorbers from my data (left) and Penton et al. (2004) (right plot, middle segment). While not as pronounced as the Penton et al. (2004) data, there is a significant excess of strong Ly $\alpha$  absorbers (by both measures) at  $\Delta v < 250$  km/sec in my data. In addition, when a higher equivalent width cut is made (blue line), the excess becomes even more pronounced. . . . . 62

- 4.8 Three sightlines through the Great Wall region with Ly $\alpha$  absorbers with  $Log(N_{HI}) > 12.9$ . The solid black lines are the number of galaxies within  $3h_{70}^{-1}$  Mpc cylinders as you move outward in redshift space. The vertical green lines are Ly $\alpha$  absorbers specific to that sightline. As discussed in the text, a “hit” of a Ly $\alpha$  absorber aligned with the Great Wall is based on the number of galaxies to determine the exact extent and location of the Great Wall along that specific sightline. Here, HS1102+3441 counts as a “hit” for the two looser restrictions, FBQS1010+3003 is a “hit” for all three restrictions, and TON580 is only a “hit” for the loosest restriction. . . . . 64
- 4.9 The combined pathlength of all eleven QSO targets that is available to search for Ly $\alpha$  absorbers. Dips are due to obscuring galactic lines, non-Ly $\alpha$  absorbers and changes in the  $\mathcal{W}$  detection limit. In addition, one QSO (Mrk421) is located at  $z = 0.03$  and its pathlength ends there. . . . . 68
- 4.10 The combined pathlength of all eleven QSO sightlines after correcting for absorbers that obscure Ly $\alpha$  and the redshift limits imposed by the galactic survey luminosity limits,  $0.1L_{\star}$  (top),  $0.5L_{\star}$  (middle),  $L_{\star}$  (bottom). While the  $0.1L_{\star}$  pathlength is significantly diminished, the  $L_{\star}$  limit is almost unchanged from an uncorrected sample. 70
- 4.11 The number of Ly $\alpha$  absorbers per redshift (black) and the number of galaxies per redshift as a function of their co-moving distance to the QSO line-of-sight (colors) of the eleven QSO sightlines with redshift limits imposed by the galactic survey luminosity limits,  $0.1L_{\star}$  (top),  $0.5L_{\star}$  (middle),  $L_{\star}$  (bottom). The larger number of galaxies from  $0.015 < z < 0.035$  is the CfA Great Wall, while the lack of galaxies and  $z = 0.04$  and  $0.045 < z < 0.06$  are the following galactic voids. The increasing density of galaxies at  $z > 0.06$  is the beginning of the Sloan Great Wall. The Ly $\alpha$  absorbers have been limited to to  $Log(N_{HI}) > 12.9$  to match sightline sensitivity. 71

- 4.12 The adjusted galaxies and Ly $\alpha$  absorbers per redshift including only the strong absorbers ( $\text{Log}(N_{HI}) > 13.0$ ) on the top,  $\text{Log}(N_{HI}) > 13.5$  in the middle and  $\text{Log}(N_{HI}) > 14.0$  on the bottom. Increasing column density cutoffs show a better correlation with the background galaxy density for  $z < 0.04$ . All the plots are  $1.0 L_{\star}$  limited. Note that each plot has a different y-axis scale for absorbers per redshift. 73
- 4.13 The luminosity of nearest neighbor galaxy to each Ly $\alpha$  absorber versus its distance from said absorber. Those absorbers that do not have a galaxy within  $3 h_{70}^{-1}$  Mpc are not shown. The sample is split between strong and weak Ly $\alpha$  absorbers. . . . . 76
- 4.14 The nearest galactic neighbor for each Ly $\alpha$  absorber and this spatial separation of them for the three luminosity cutoff regimes,  $0.1L_{\star}$  (top),  $0.5L_{\star}$  (center), and  $L_{\star}$  (bottom). The data points are split between strong and weak Ly $\alpha$  column densities ( $\text{Log}(N_{HI})= 13.0$ ). . . . . 77
- 4.15 The nearest galactic neighbor for each Ly $\alpha$  absorber and this spatial separation based on the number of virial radii of each galaxy for the three luminosity cutoff regimes,  $0.1L_{\star}$  (top),  $0.5L_{\star}$  (center), and  $L_{\star}$  (bottom). The data points are split between strong and weak Ly $\alpha$  column densities ( $\text{Log}(N_{HI})= 13.0$ ). . . . . 78
- 4.16 The column density ( $N_{HI}$ ) and nearest neighbor galaxy distance, if the absorber has one, of each Ly $\alpha$  absorber. The luminosity limits are  $0.1L_{\star}$  (top),  $0.5L_{\star}$  (middle) and  $L_{\star}$  (bottom). The median column density ( $\text{Log}(N_{HI})= 13.0$ ) that divides strong and weak absorbers is marked with a dashed vertical line. . . . . 81
- 4.17 The column density ( $N_{HI}$ ) and nearest neighbor galaxy, if the absorber has one, distance in units of the individual galaxy's virial radius. The luminosity limits are  $0.1L_{\star}$  (top),  $0.5L_{\star}$  (middle) and  $L_{\star}$  (bottom). The median column density ( $\text{Log}(N_{HI})= 13.0$ ) that divides strong and weak absorbers is marked with a dashed vertical line. . . . . 82

4.18	The same map as Figure 3.1 with the eleven QSO sightlines of this thesis (blue lines) and the twenty-seven addition QSO sightlines that could be added to the sample (dashed lines). Adding in all twenty-seven sightlines would increase the number of Ly $\alpha$ absorbers by an estimated 250%. I suggest that this expansion of the sample should be one of the next steps taken in the continued study of the Ly $\alpha$ absorber-galaxy examination. Note: the declination wedge shown does not cover every sightline drawn on the plot. . . . .	85
A.1	The $0.0035 < z < 0.07$ (1220-1300 Å) range of the FBQS1010+3003 spectrum. Solid green vertical lines mark (and are labeled) Ly $\alpha$ absorbers, while dashed blue lines (also labeled) mark other Lyman or metal lines from Ly $\alpha$ absorber systems at higher redshifts. Ly $\alpha$ absorber green lines with a red marker at the bottom are “marginal” ( $3\sigma < SL < 4\sigma$ ). Red dashed and dotted vertical lines show the location of common galactic absorption lines, which are not always present. The red continuum fit is augmented by the voigt profile fit of each absorber. Finally, each non-Ly $\alpha$ feature is surrounded by a yellow box that denotes the region in which a Ly $\alpha$ absorber could not be found due to the obscuration. . . . .	91
A.2	The continuation of Figure A.1 for the HS1102+3441 spectrum. . . . .	92
A.3	The continuation of Figure A.1 for the Mrk421 spectrum. Note: the QSO is located at $z = 0.03$ (1252 Å for Ly $\alpha$ ), limiting the Ly $\alpha$ search. . . . .	93
A.4	The continuation of Figure A.1 for the PG0832+251 spectrum. Note: the absorption feature at 1236.9 Å is poorly constrained and probably the blending of several component environments from galaxies that are 14 and $53 h_{70}^{-1}$ kpc away. . . . .	94
A.5	The continuation of Figure A.1 for the PG0953+415 spectrum. . . . .	95
A.6	The continuation of Figure A.1 for the PG1048+342 spectrum. . . . .	96
A.7	The continuation of Figure A.1 for the PG1115+407 spectrum. . . . .	97
A.8	The continuation of Figure A.1 for the PG1116+215 spectrum. . . . .	98

A.9 The continuation of Figure A.1 for the PG1121+422 spectrum. . . . .	99
A.10 The continuation of Figure A.1 for the Ton236 spectrum. . . . .	100
A.11 The continuation of Figure A.1 for the Ton580 spectrum. . . . .	101

## Chapter 1

### Star Formation in Nearby Galaxies

As is common in life, this thesis did not follow the planned linear path. I began work on a sounding rocket telescope with the intention of using its data on star formation in other galaxies as the basis for my thesis. Due to malfunctions during the flight, the resulting data was corrupted and unusable. I then turned to a secondary science topic to demonstrate that I am not only a capable instrument builder, but a well-rounded scientist. Therefore, this thesis contains two, fairly distinct, halves. The first two chapters discuss the science goals, §1, and the construction and flight, §2, of the sounding rocket telescope. The second half covers the background, §3 and results, §4, of a search for hydrogen Ly $\alpha$  absorbers in spectra taken by the Cosmic Origins Spectrograph (COS). Appendix A provides a complete list of §4 data and Appendix B provides a list of acronyms used in this thesis for quick reference.

#### 1.1 Star formation in galaxies

A main goal of studying high redshift galaxies is to determine what point in the history of the universe coincided with the epoch of peak star formation within galaxies, since the star formation rate decreases from a redshift ( $z$ ) of  $z = 1$  to  $z = 0$  (Buat et al., 2008). Galactic development models depend on the rate and timing of star formation as limits to possible evolutionary paths (Johnson et al., 2007). Thus, studying star-forming regions in galaxies of varying redshifts leads to further understanding of the history and concurrent evolution of the universe as a whole (Sargsyan & Weedman, 2009). Star-forming regions contain an abundance of young, hot O and B type stars

and emit a significant fraction of their energy in the ultraviolet (UV) (Elmegreen, 2002). Flux in the Far-ultraviolet (FUV) and Near-ultraviolet (NUV) wavelength regions is a sensitive probe for these young stellar clusters and, due to the change in wavelength from galaxy's redshift, we observe of this radiation in the NUV and visible bands respectively, greatly facilitating their study (Bianchi et al., 2005). However, the picture is complicated by intervening dust which typically absorbs and scatters photons strongly in the UV and is one of the least understood phenomena that take place in a galaxy (Calzetti et al., 1994). In fact, the greatest disparities between existing galaxy attenuation measurements (the Milky Way and Large Magellanic Cloud) occur in the UV (Noll et al., 2007), precisely where the most attenuation occurs. Since the extinction ( $E(B - V)$ ) at 1500 Å is 2.5 times that of 5500 Å, which in turn is ten times that of 2.2 μm (Gordon et al., 1997), a wide range of wavelengths are needed to account for these effects, as illustrated in Figure 1.1. Thus, accurately removing the effect of the intervening dust on the UV emission becomes crucial to the accounting of young stars. Only when we understand and can reasonably approximate the UV extinction caused by dust can we confidently assign values to star-forming regions in galactic evolution studies.

Virtually all observations of astrophysical objects, and sometimes their actual physical processes, are affected by the presence of dust in their immediate vicinity or the line-of-sight, making the study of dust a crucial step in understanding the universe (Bianchi et al., 1996). While dust and its effects have been extensively studied in various wavelengths (e.g. McClure, 2009), at various redshifts (e.g. Nozawa et al., 2009), in relatively local environments (e.g. Sitko et al., 2008), and in computer models (e.g. Witt & Gordon, 2000; Bush et al., 2010), we still struggle to account for its effects on an individual observation. Unfortunately, direct determination of galactic attenuation curves is currently limited to extremely close galaxies: the Milky Way, the Large and Small Magellanic Clouds and, to some degree, M31 (Andromeda) (Noll et al., 2007; Fitzpatrick, 2004). In addition, the UV extinction measured in one (e.g. the Milky Way) almost certainly does not apply to others (Clayton, 2004). Local environmental effects, such as grain sizes, densities and shock fronts, likely dominate small-scale extinction properties and may even do the same on a

galaxy wide measurement (Calzetti et al., 1994). A galaxy’s attenuation curve, the loss of flux by wavelength, and the physical dust extinction curve, the loss of flux due to a specific type of dust, are distinct entities. While the dust extinction curve is due to the physical properties of the dust (e.g. size and composition), the galactic attenuation is a combination of the dust extinction and also the spatial distribution of said dust around the stars of study (Gordon et al., 1997). Thus, even with an accurate accounting of the galaxy’s attenuation, we cannot definitively untangle the physical properties of the dust from its spatial distribution (Gordon et al., 1997).

Measuring the UV flux from high- $z$  galaxies bypasses many of these small-scale effects while simultaneously introducing the complication inherent when an extended system is averaged together into a few measurements and differing regions combine into a typical galactic whole. While this

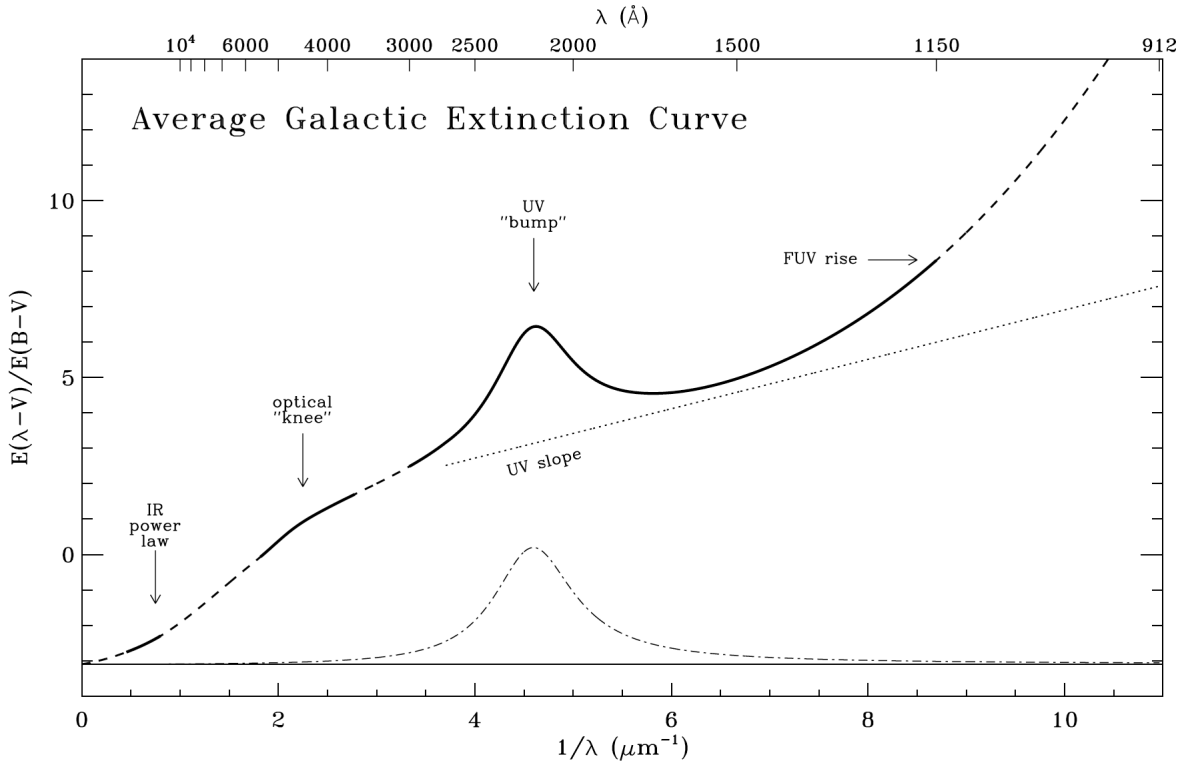


Figure 1.1: An averaged attenuation curve of the Milky Way galaxy in color magnitudes versus wavelength (reprinted from Fitzpatrick, 2004). The solid lines represent measured data, while the dashed lines are predicted values for unobserved regions of the spectrum. Notice the increasing attenuation with shorter wavelengths and the lack of data of wavelengths shorter than  $\approx 1150 \text{ \AA}$ .

measurement may be more insensitive to an individual star's local conditions, it is still affected by galactic attenuation. A single model must remove these influences all at once to retrieve the actual UV flux. To create the most accurate model possible, a source that is close enough to spatially separate out the various dust conditions is studied. Only when individual effects of differing dust conditions are understood can we confidently combine them with the appropriate weighting into a single extinction model.

There are numerous models of dust attenuation (e.g. Fitzpatrick & Massa, 1990; Calzetti et al., 1994; Gordon et al., 1997), and the Galaxy Evolution Explorer (GALEX) mission was launched to provide additional wavelength bands with which to study these effects. With two UV bands of 1350-1750 Å and 1750-2800 Å, GALEX provides two points with which to fit a model of galactic attenuation and dust extinction while simultaneously measuring the UV output of star-forming regions. My goal was to expand upon GALEX's leading role by measuring star formation and dust attenuation in a third wavelength band, 900-1000 Å. At these wavelengths, I would observe predominantly O stars, as opposed to the mix of O and B stars that populate a GALEX image. This new wavelength band would provide additional information by identifying the youngest stars and thus the youngest/most recent star-forming regions. In addition, this new wavelength band is beneficial when extending studies to higher redshifts and using closer galaxies as analogs. While the helpful transition of high redshift FUV into the optical makes it easier to observe, in order to make an accurate comparison to local galaxies we need measurements at that same FUV wavelength (Burgarella et al., 2001). Thus, a new 900-1000 Å imager allows analogous studies of galaxies ever deeper in the universe.

Just as important, my observations would provide a data point at a new and vital wavelength upon which to fit an extinction curve model. A model based on wavelengths that are either far from the region of interest (IR, optical) or that have similar dust extinction effects (GALEX UV bands) (Bianchi et al., 2005), may miss the full shape of the curve, especially since the extinction curve can steepen significantly in the far UV (Fitzpatrick, 2004). Figure 1.2 shows this steepening in a previous measurement of the extinction to M31 by Bianchi et al. (1996). Since the most reliable

measures of UV attenuation come from spectral energy distributions that cover the infrared to the far ultraviolet (Witt & Gordon, 2000), I planned to utilize data from Spitzer, Sloan Digital Sky Survey (SDSS), GALEX and my own instrument. I anticipated using a computer model such as Witt & Gordon (2000)'s DIRTY that allows assessment of the dust attenuation based on multiple wavelength observations.

The two targets selected for the first flight of this payload were M51 (the Whirlpool galaxy) and the white dwarf, G191B2B. M51 was chosen not only for its scientific properties, but also for its orientation that shows us the full galactic disc and expected surface brightness at these wavelengths (Tikhonov et al., 2009), necessary for a sounding rocket flight being used as a technology demonstrator (see §2.5). G191B2B represents the canonical white dwarf (Green et al., 1990) and has been used as a standard source and common calibration target for GALEX (Morrissey et al., 2007), ground based instruments (Holberg & Bergeron, 2006), NICMOS (Batcheldor et al., 2006), previous Colorado rocket experiments (Gunderson et al., 2001), FUSE (Sahnou et al., 2000) and Hubble Space Telescope (Stone, 1996; Bohlin et al., 1995). Combined with pre and post flight calibration measurements, the observation of G191B2B would have allowed me to create an absolute flux measurement from my data. This would have greatly enhanced the value of the experiment by allowing direct comparison to numerous other instruments and studies. Upon completion of launch and data reduction, I would have created three-color maps using my data and the two wavelengths of GALEX.

While, as previously mentioned, I was unable to obtain the scientific data from this flight, the science was not the only goal of this mission. As will be described in detail in §2, the successful completion of all the technology goals allowed the collection of an image at a heretofore unobserved portion of the spectrum. With this success, when the instrument is rebuilt, the second flight can be more ambitious in target selection and will likely observe M31 (Andromeda) for a more detailed look at dust and star forming regions with less importance placed on absolute flux since the technology is now proven.

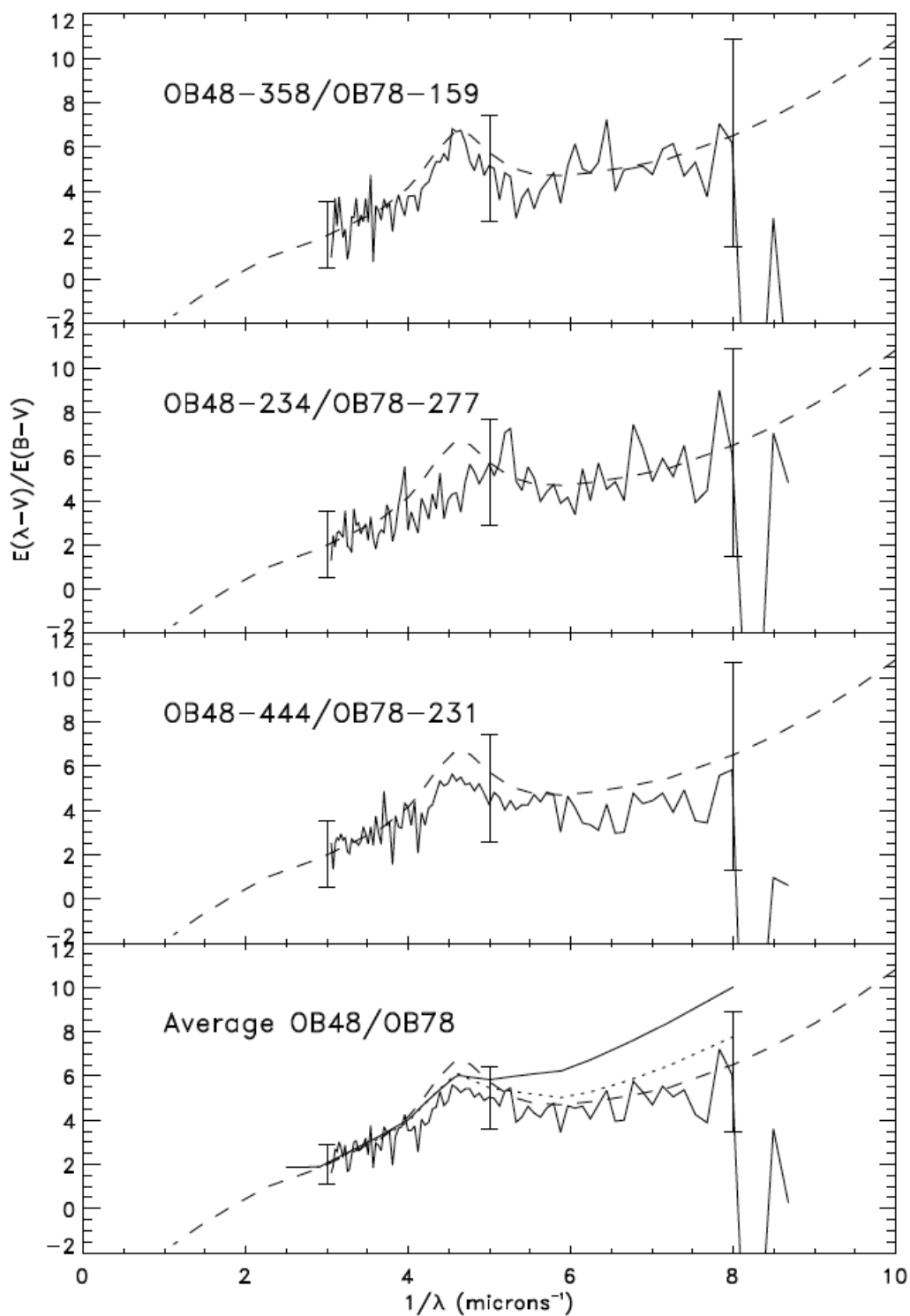


Figure 1.2: Attenuation between pairs of stars within M31 (reprinted from Bianchi et al., 1996). As in Figure 1.1, the attenuation of signal rises sharply in the FUV. My instrument would add additional data points to similar measurement at  $1/\lambda \approx 10.5$  on this scale.

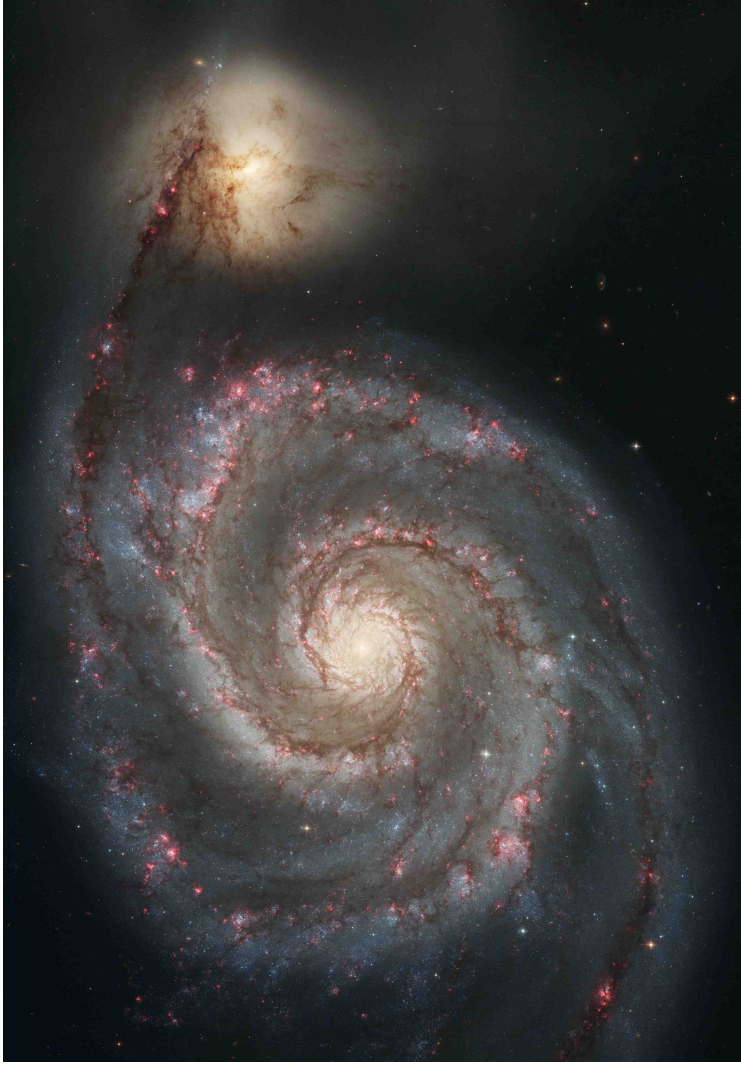


Figure 1.3: M51 (the Whirlpool galaxy) in visible light taken by the Hubble Space Telescope. Produced under NASA contract NAS5-26555.

## Chapter 2

### Far-Ultraviolet Imaging Rocket Experiment

*Between the acting of a dreadful thing  
And the first motion, all the interim is  
Like a phantasma or a hideous dream.*

-Shakespeare

In order to investigate star forming regions in nearby galaxies, I designed and built the Far-ultraviolet Imaging Rocket Experiment (FIRE), mission 36.257. FIRE launched on January 28th, 2011 from the Poker Flat, Alaska launch complex. The first flight targeted M51, the Whirlpool Galaxy. I chose M51 for its angular size on the sky, its face-on orientation to Earth, and its expected brightness in our passband of 900-1000 Å.

#### 2.1 Payload Overview and Mirror Design

The telescope's design was driven by the primary (and only) mirror, a parabolic prime-focus system with a focal length of 1750 mm. The mirror was purchased and shaped before funding for the project was awarded and therefore had to be designed without knowledge of other building constraints. The mirror was chosen such that the payload would have the standard 17.25 inch diameter skins while using the standard 14 inch diameter skins for an interior structure. It was also chosen to have a parabolic shape as the only focusing element in the light path. The outside diameter of the mirror, 13.25 inches, was made to fit inside the 14 inch inner skin while the 5 inch

hole at the center was placed as a weight-saving feature since it was assumed that that surface area would be blocked by the detector assembly.

The final telescope design was very close to these assumptions, in part because once the mirror was accounted for there was little reason to make major revisions. As can be seen in Figure 2.2, we did indeed use the 17.25 inch exterior skins, as well as 14 inch skins for the interior structure. The only change was that the standard Radax screw pattern that is used with all rocket skin sizes (for ease of manufacturing the interior skins) could not be used because it would have taken the interior edge of the inner skin to 13.25 inches diameter, the same size as the mirror. Thus, a slightly different machine pattern was used on the ends of the inner skins to allow the mirror a 1/4 inch clearance on all sides.

Two problems and one additional consideration about the mirror should be discussed. First, the mounting of the mirror was accomplished by three 1/4"-28 bolt holes tapped directly into the mirror metal instead of through-holes with room to place nuts on each side. Due to the relatively low pullout strength of the mirror material (aluminum) and the mirror's weight (approximately 45 pounds), springs could not be used to secure the mirror to its structural mounting plate. While this did not affect the final telescope quality, it did make it more difficult to focus by requiring that two nuts, one on each side of the mirror mount plate, be changed for each mirror adjustment instead of one. Second, the mirror was cut so that the optical axis of the parabola was not perpendicular to the flat sides (i.e. the back) of the mirror. Minor adjustment space was allowed for during telescope design; however, I did not account for such an offset being more than three degrees at worst. During focus, I discovered that this mis-cut was at least the three degrees allowed adjustment and using the resulting images and I later measured it to be 3.4 degrees. Since adjustment was not sufficient to bring the optical axis in line with the structural axis of the telescope, the mirror was flown in an off-axis configuration. Thus, the optical pointing was three degrees off from the structural pointing, almost entirely in the horizontal or yaw direction. This also meant that the star tracker had to be physically shimmed, which I accomplished by inserting spacers on the star tracker's mounting post to rotate its pointing and account for that same three degrees in yaw. As a result,

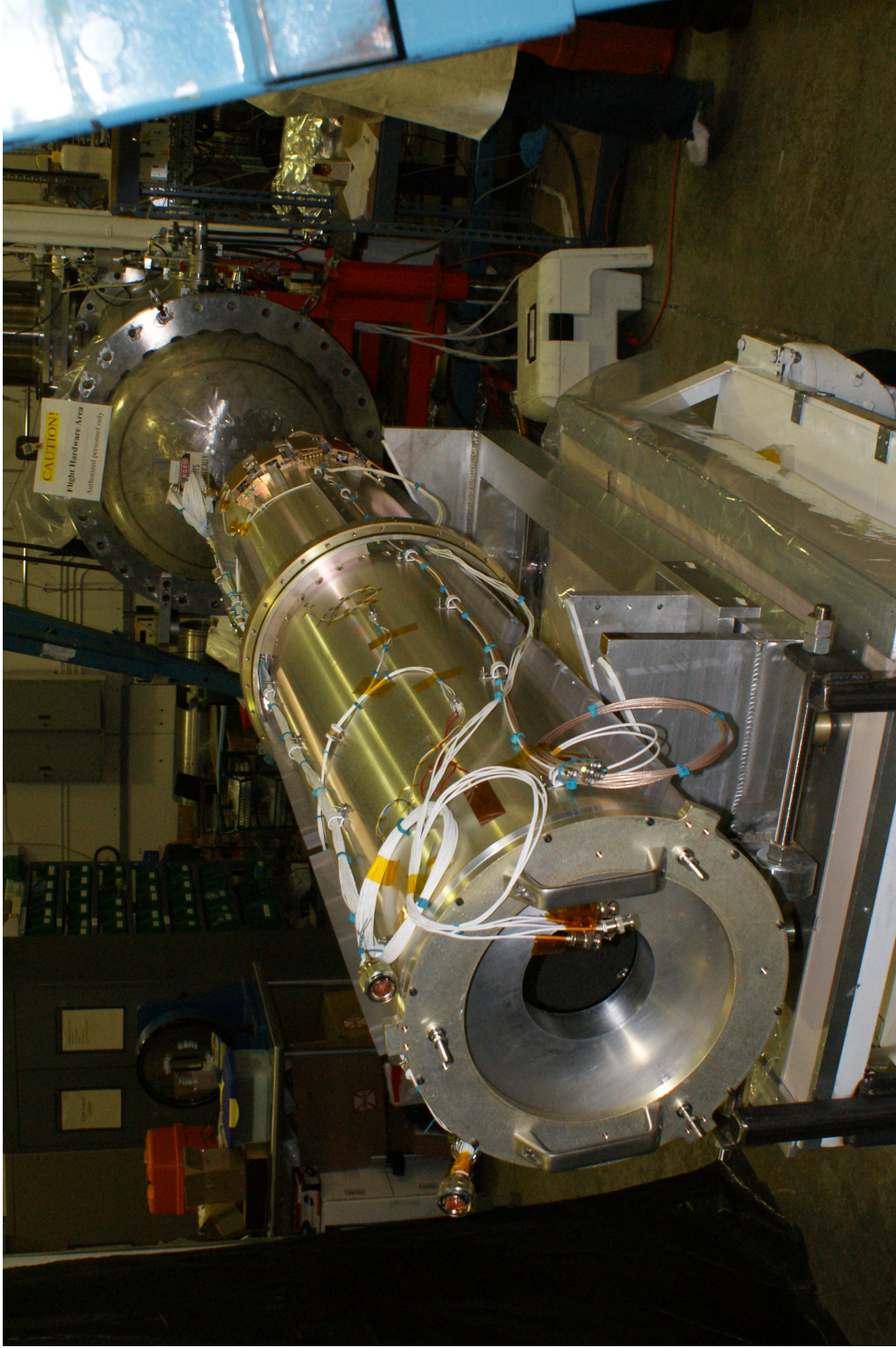


Figure 2.1: The FIRE primary mirror installed within the telescope (bottom left, identified by the 5 inch hole in its center).

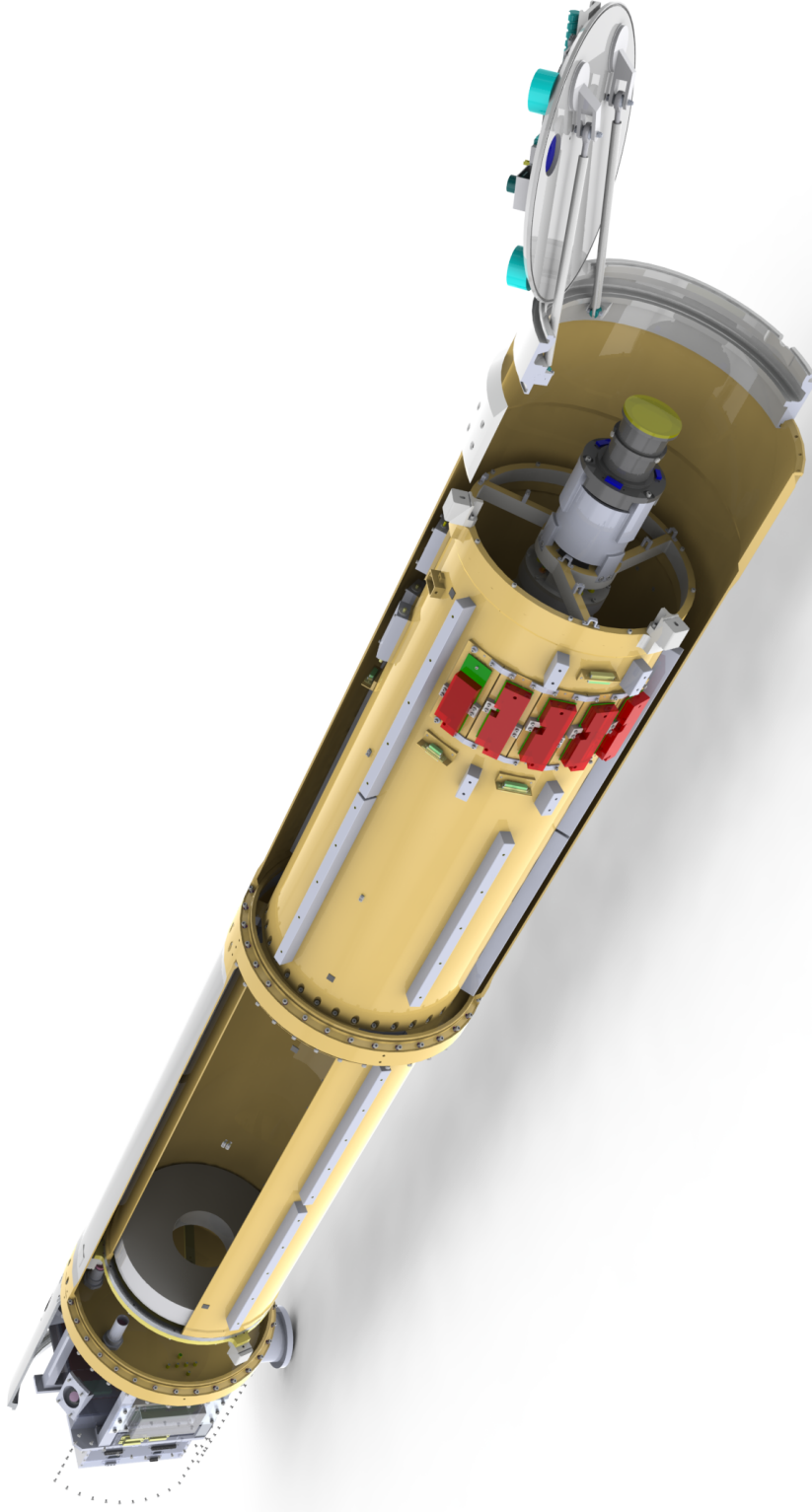


Figure 2.2: The FIRE telescope cut-away drafting model. Note the mirror in the upper left and the internal skins (14 inches diameter) and external skins (17.25 inches diameter) and the electronics (red boxes) that fit in the space between them. The grey bars that run along the internal skin are the lexan “safety rails” that protect wires and electronics during assembly. The vacuum canister discussed in §2.2 is hidden within the inner skin behind the red electronic boxes.

the final focus of the system was worse than expected because of the coma introduced by off-axis operation; final measurements put the resolution element of FIRE at 8 arcseconds. Finally, the mirror was purchased (and FIRE was locked into a 17.25 inch skin), before detailed examination of the available targets was completed. For future flights of a rebuilt FIRE, it would be advantageous to upgrade to a 22 inch skin, double the mirror area and, thus, double the photon collection rate. While this would result in a decreased length of time on target due to the extra weight, this loss is outweighed by increased collection rate and results in a higher total of photons from the mission.

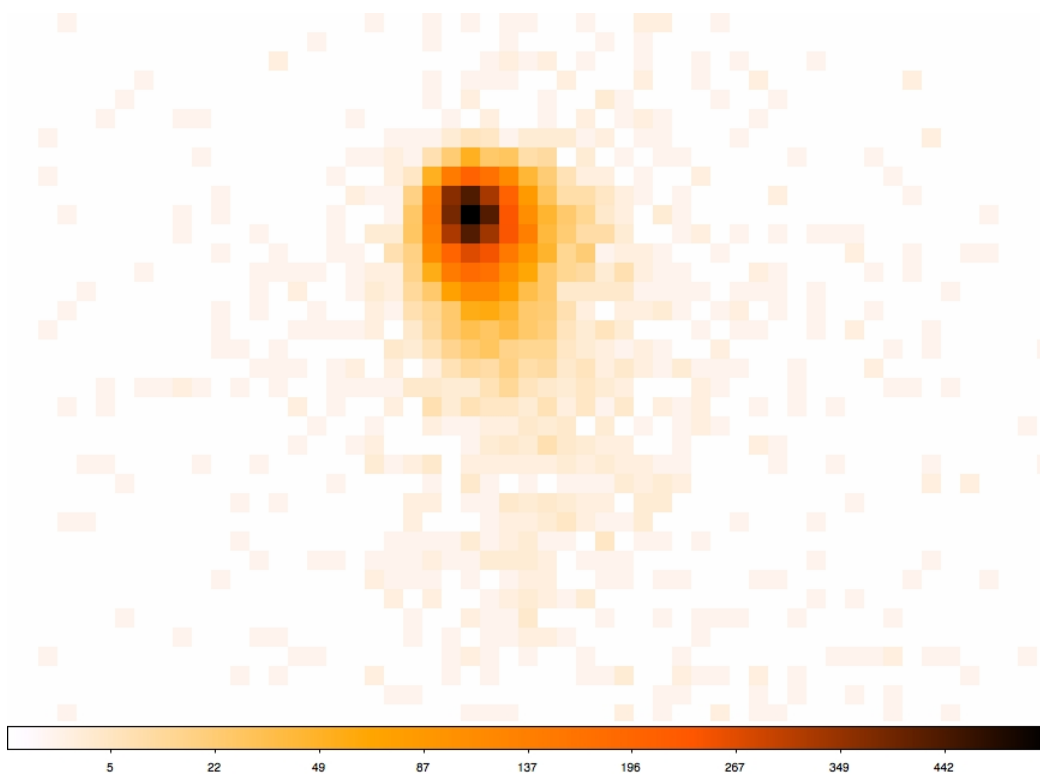


Figure 2.3: The final focus results for FIRE. Notice the residual coma that could not be corrected for in alignment. The final precision of this instrument was 8 arcseconds per resolution element.

The mirror reflecting surface was coated with silicon carbide. Silicon carbide has excellent reflectivity, approximately 30%, in the desired passband (see Figure 2.4) (Lambrecht et al., 1994; Keski-Kuha et al., 1995, 1999) when using chemically vapor deposited SiC on a bulk substrate. It also has the advantage of not being hydrophilic like lithium fluoride or other protective salts and therefore, much easier to work with while assembling the telescope. While 30% reflectivity at

these wavelengths is excellent, it is still low enough that including secondary optics results in a significant reduction in signal throughput. Thus, while the additional optics could have reduced aberrations, I decided that for the very first image at these wavelengths collecting the most light possible overrode other considerations such as resolution or field-of-view.

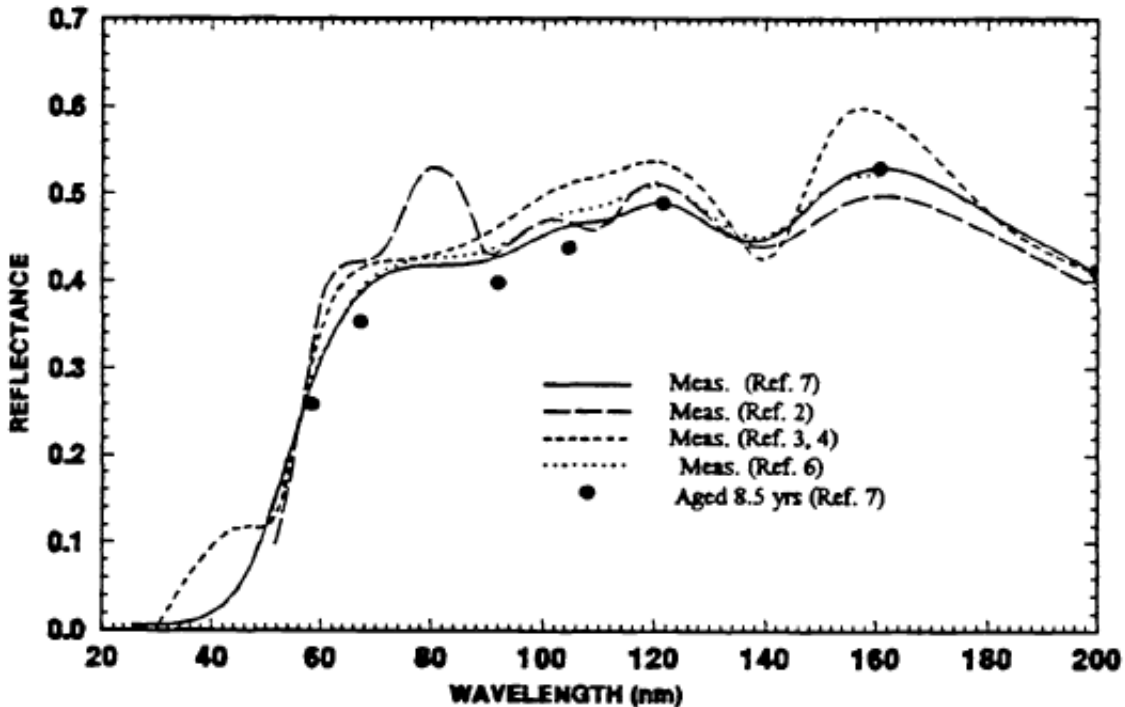


Figure 2.4: The reflectance of silicon carbide across the FUV wavelengths. The dots show a long duration study of its reflectance, 8.5 years. Silicon carbide has an average reflectance of 40% across the telescope's 900-1000 Å passband. Plot reprinted from Keski-Kuha et al. (1995).

Other design considerations were the gap between the inner and outer skins of the telescope and the placement of electronics within that space, as illustrated in Figure 2.2. The two high-voltage supplies and the high-voltage mixer were all placed in the one-inch gap between the inner and outer skins. In addition, the pre-amplifier for the detector, the temperature sensors, heaters and all the wiring were also placed within this space. Order of operations dictated that all these needed to be in place and secured to the inner skin before the outer skin was installed. Therefore, I attached numerous “safety rails” of 3/4 inch tall lexan to the inner skin along the path of the wires

and next to electronics and connectors. These not only protected delicate components, but also helped guide the outer skin during installation. For the next flight, I would recommend moving the high voltage supplies and pre-amplifier out of this gap and into the electronics section. Upon further review, neither need to be as close to the detector as originally thought and their placement in the electronics section would greatly simplify the design and assembly of the telescope.

Finally, instead of using the standard steel grade-8 black-oxide screws of previous rockets, I decided to use the steel alloy A286 screws. During initial assembly of the payload, black oxide screws were consistently found either to rust extensively during cleaning or to have greases that could not be removed by our standard cleaning methods. While we could remove these greases by extensive cleaning by hand, the time spent was usually more than five minutes per screw, an unacceptable use of time. The loss of reliable black-oxide screws is generally attributed to manufacturing in locations with less stringent quality control systems. Screws known to have been produced in the United States did not exhibit the same rusting or cleaning problems. Unfortunately, I was unable to procure a reliable source of these screws in quantities that were reasonable for the payload (i.e. dozens or hundreds as opposed to thousands or tens-of-thousands). In the end, even with the typical price difference of 2000%, the use of A286 screws was more economical in both time and money than black-oxide.

## 2.2 Canister Design

The most important component of the FIRE telescope design is the indium filter that sits directly in front of the detector. This filter is approximately 2000 Å thick and supported by a thin nickel mesh (see Figure 2.5). The filter is described in detail in §2.3. Not only did it drive the passband of the telescope, but it dominated the mechanical design as well. In order to survive the vibrations and shocks associated with rocket ascent, the filter had to be maintained at a pressure less than  $10^{-3}$  torr during launch. While a telescope payload is easily maintained at this pressure while it is being actively pumped on ( $10^{-6} - 10^{-7}$  torr is typical), once the pump is removed, within one to two hours the pressure will rise due to outgassing of interior aluminum and leaks in

the vacuum seals of the payload. While each payload has its own rate of pressure rise and it was quite possible that FIRE could hold a vacuum of sufficient quality, I determined that the methods to fix the system if it failed in this regard were limited and thus I needed to preemptively address the issue.



Figure 2.5: One of the indium filters used in FIRE.

This conclusion meant that the vacuum would have to be actively maintained until just a few minutes before liftoff. There were two sensible ways to accomplish this. First, we could have used an external pump that connected to the payload via a remotely controlled gate valve. Shortly before launch, the gate valve could be closed preserving the payload vacuum and the pump apparatus could pull or break away as the rocket launched. This solution had been used in the past on previous rocket payloads with mixed success. The biggest concern was that it would be difficult, if not impossible, to test the system prior to launch. In addition, there were the complications of operating electrical machinery next to the armed rocket.

The second option was to mount an internal pump and allow it to ride along with the payload. This allowed the option of pumping until just a few seconds before launch, ensuring the best possible vacuum. This also meant I could fully test the system in the lab, a significant advantage. Any pump large enough to affect the entire volume, however, would have dramatically increased the weight of the payload and significantly cut the time spent high enough above the atmosphere to collect data. Thus, I determined the optimal setup was a small vacuum chamber that would surround only the filter and the detector sitting next to it. An ion pump for a volume of this size ( $\approx 25 \text{ inches}^3$ ) could be only a few cubic inches in size itself and weigh less than three pounds.

While this decision was a simple solution to the vacuum problem, it introduced a second problem. Once the telescope was in space, the vacuum canister had to allow photons to reach the filter and detector. Since I could find no materials that were simultaneously transparent at these wavelengths and strong enough to deal with the pressure differences involved, the canister would have to open during flight and would add the complexity of internal moving parts. Typically, these are avoided in sounding rockets due to the added testing and expense of motors that are vacuum safe and strong enough to survive the launch themselves.

Once I decided to add a door to the canister that would open during flight, I had to confront the space limitations that this mechanism had to fit within. As shown in Figure 2.6, there is a small annulus of space around the detector that will not block the collection of light by the primary mirror and attenuate the signal. Any obscuration at this location, however, would only block the effective area of the system and not affect its resolution or field-of-view. Thus, the design was constrained with the goal of blocking as little of the mirror as possible. Within this space, I had to fit the pump itself and the source(s) of mechanical force needed to open and close the canister door.

Initially, I expected to use an electric motor to operate the canister door. However, finding a motor that was made of materials safe for exposure to vacuum near our optics limited the available options. Most electric motors contain plastics or greases that could outgas in a vacuum and, if they landed on the primary mirror or detector plates, would destroy the efficiency of the system. While

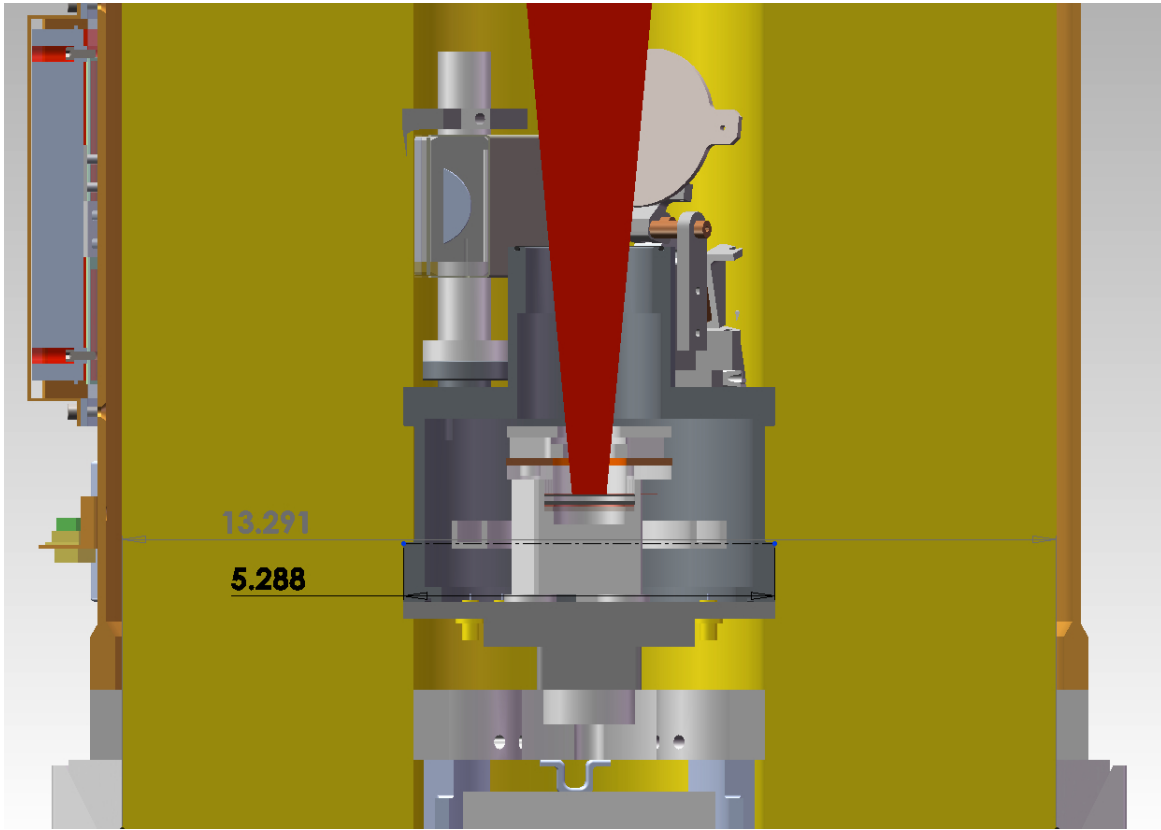


Figure 2.6: A cross-section of the space available that was not in the telescope's light path. In this view, the light enters from the bottom and the mirror is above focusing light back downward. The yellow annulus shows the incoming unfocused light that would be moderately harmful to block, while the red cone shows the focused light that would be extremely detrimental to block. The remaining space, a cylinder five inches across, had to contain the detector, filter, star tracker, vacuum pump, vacuum canister, canister door opening/closing mechanism and all accompanying wires. The measurements shown are of the diameter of the mirror (13.291 inches) and the canister system (5.288 inches), thus the canister extends 0.144 inches into the interior edge of the incoming lightpath. See Figure 2.8 for the entire canister system upon completion.

there were a few motors available that fit our criteria, none possessed the torque needed to open the canister door in a timely manner during flight and still remain physically small enough not to block significant quantities of light. I then decided to use a loaded spring to open the canister door in flight. This had several benefits. First, the portion of the mechanism that operated during flight could be as simple and reliable as possible. Second, the motor force that closed the canister could run at any speed needed since that operation was prior to flight and thus could provide the appropriate torque with planetary gears. Finally, the power needed to operate the canister closing mechanism could be provided by the ground station, since it would only operate on the ground, and would not tax the payload's electronics.

With this relaxation of the operation speed and several failed attempts to find an appropriate motor, I instead decided to use a wax actuator. These are small tubes of parafin wax surrounded by a heater and a piston on one end, as shown in Figure 2.7. When the wax is heated, it expands in a predictable and repeatable manner and generates 75 pounds of force. More significantly, the physical size of the wax actuator was approximately ten times smaller than electric motor I had been considering and fit comfortably into the available design space within the telescope. The primary disadvantage of the wax actuator was that it took several minutes of power before motion actually began. However, since the design now included a spring loaded door and several hours to prepare the canister for launch, this was no longer a problem.



Figure 2.7: Wax actuator used as the motor power to close the canister vacuum door in pre-flight preparations. See Figure 2.8 for placement on the canister.

In the final design of the canister, I used two wax actuators to provide enough force to seal a two-inch diameter opening with a 1/16 inch thick viton o-ring. The force was transferred to the door by a small set of parts that ran on ball-bearing linear slides. After sealing the door, a pin is positioned to counteract the spring force that is always trying to pry it open. This pin is then pulled in flight by a solenoid. Thus, the only operation during flight is the activation of the solenoid and the motion of the canister door springing open, both very reliable actions. Finally, any part of the mechanism that slid over another part was built out of phosphor-bronze to minimize the surface friction.

This design proved extremely reliable. The device worked correctly over 100 times before a partial failure during integration. When examined, it was determined that repeated operation had created the minimum friction necessary to impede the canister door from opening when it was fighting gravity (i.e. when the telescope was vertical). Since lubrication had not been used on the mechanism, this was considered a minor issue. When the mechanism was then greased with a vacuum safe lubricant, Braycote, it operated correctly for another thirty cycles before flying and working perfectly in-flight.

### 2.3 Indium Filters

In order to limit the passband of the telescope to 900-1000 Å, I used a pure indium filter directly in front of the detector. As shown in the theoretical transmission in Figure 2.10, indium has an acceptable transmittance at these wavelengths and most importantly only passes  $\approx 2 \times 10^{-5}$  of the 1216 Å Ly $\alpha$  photons. If left unmitigated, the background glow from Ly $\alpha$  would easily swamp the signal desired and would overwhelm the payload electronics with more counts than it could process. Therefore, it was a mission critical goal that the indium filter remained intact through launch, demanding the steps taken in §2.2.

### 2.3.1 Initial Results

The filters were purchased from the Luxel Corporation. They have extensive history in manufacturing thin-film filters and have produced pure indium filters for the University of Colorado in the past. However, when the first filters arrived, they were measured to have a significantly lower transmittance than was predicted as is shown in Figure 2.9. Numerous filters were created and tested and each showed the same low transmission characteristics. In cooperation with Luxel,

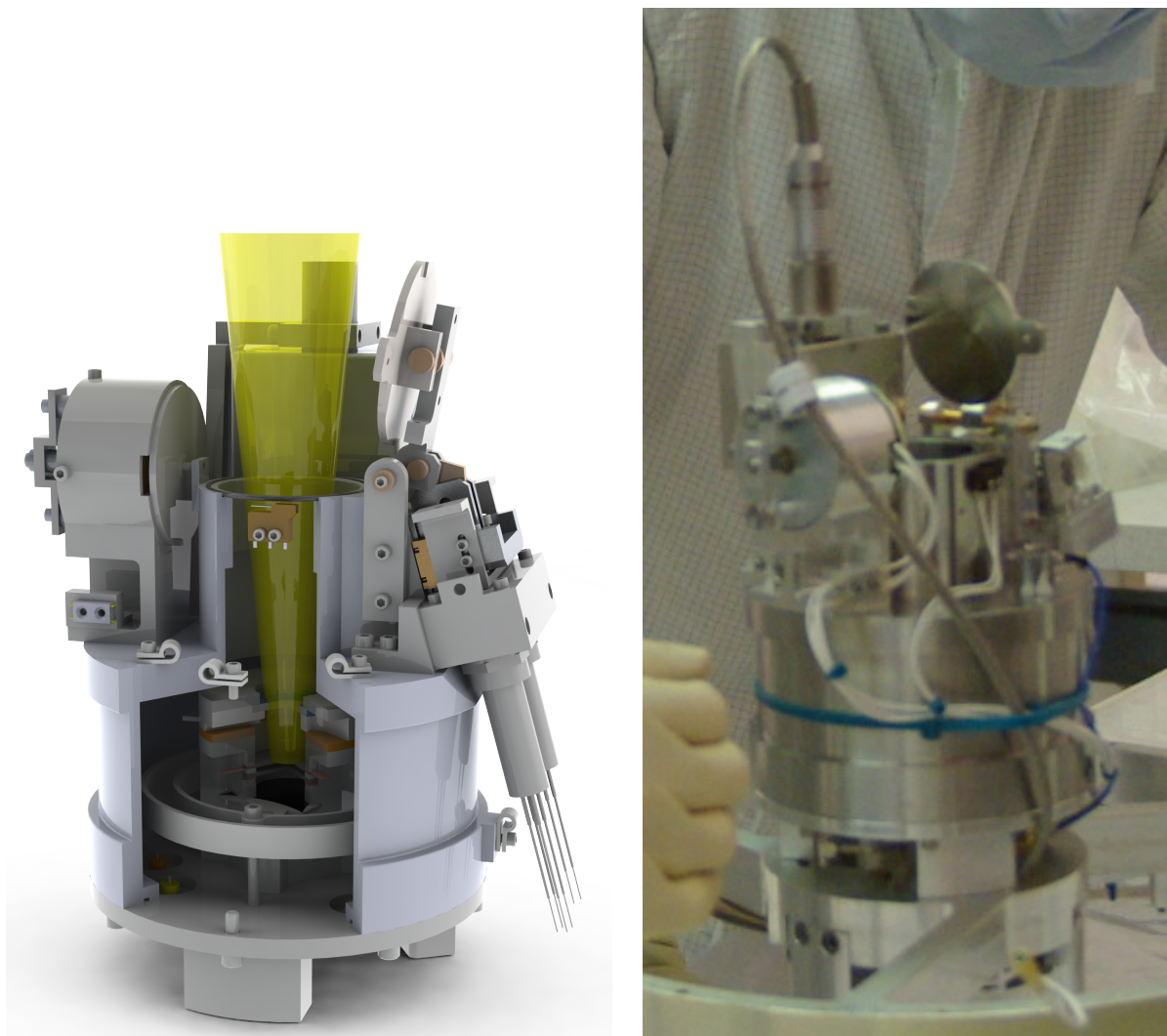


Figure 2.8: The vacuum canister that holds the detector and indium filter. The model on the left shows the wax actuators (tubes on lower right), vacuum door (top right) and detector (at base of yellow light cone in center). The real image on the right shows the door more clearly (top), the solenoid that opens the door (center left) and the ion pump (box back left with single large cable).

we began to search for the cause of this poor quality. Several filters were tested by using an Auger Electron Spectroscopy scan, a process that vaporizes the surface layers of materials and measures the atoms that are released. Testing several filters showed that there was a consistent layer of carbon and oxygen on the surface of the indium. The amount of carbon found matched the quantity required to uniformly drop the transmission across all our measured wavelengths.

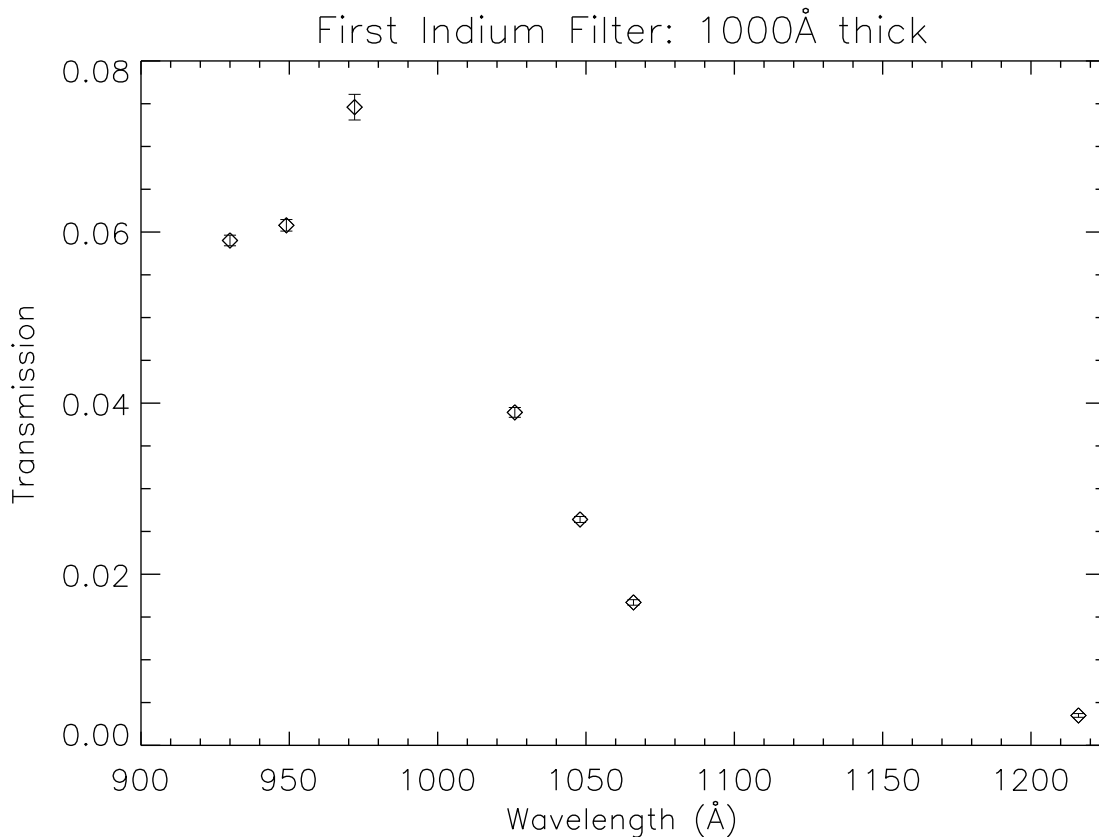


Figure 2.9: Transmission of first indium filter produced for FIRE. Note that in contrast to the final flight filter and the theoretical filter from Figure 2.10, this filter is only 1000 Å thick, making its transmission even worse in comparison. The goal was 10% transmission at 900 Å.

### 2.3.2 Plasma Cleaning

Since no change in the manufacturing process made significant differences in the carbon found on the indium surface, we began to search for methods to remove it in post-processing. The most successful was the process of plasma-cleaning, where the top surface is removed under inert

gases, thinning the entire filter. We began cooperation with Dr. Frank Greer at the Jet Propulsion Laboratory to develop a reliable method of removing the surface of the filter while not destroying it entirely. Concurrently, Luxel began a similar process of plasma-cleaning that also showed signs of success (Lairson et al., 2010).

### 2.3.3 Flight Filters

The final filters were delivered by Luxel after their own cleaning process and while they did not meet our initial requirements of at least 10% transmission at 900 Å and at most a  $10^{-4}$  transmission of Ly $\alpha$  (transmission of  $1.4 \times 10^{-4}$  at 1216 Å, see Figure 2.10), I determined that the effective Ly $\alpha$  removal was sufficient for this flight. While the noise was higher than initially calculated for, the target’s surface brightness was enough to still provide a sufficient signal-to-noise, see Figure 2.14, for the airglow the telescope was expected to see (Chakrabarti et al., 1984; Feldman et al., 2001). Since the Ly $\alpha$  transmission was higher than predicted, it meant that the filter was most likely thinner than 2000 Å, an expected result of the plasma cleaning process. Future filters should be made correspondingly thicker to account for this removal of material.

## 2.4 Detector

FIRE used a custom built resistive anode micro-channel plate (MCP) detector. A MCP is a thin glass plate with numerous cylindrical tunnels, commonly called pores or channels, across the thinnest dimension. These channels are a few degrees from perpendicular to the MCP surface, the “bias” angle. In a MCP detector, numerous MCPs are stacked together and a large negative voltage (thousands of volts) is applied across the stack with the “top” plate (closest to the mirror) more negative than the “bottom” plate. When a photon strikes the top plate it kicks off an electron from the glass. This electron is accelerated by the voltage back towards the plate and down a pore, ricocheting off the channel walls as it travels, as shown in Figure 2.11. Each contact with a wall releases numerous other electrons, each of which travel along with the voltage and create cascades of their own upon impacting the pore walls. In the MCPs I used, the process leads to an increase,

or gain, in electrons from one to approximately 10,000 through each individual plate. The bias angle ensures that an electron must strike a channel wall at least once while traveling along the voltage potential lines, as well as increasing the total number of walls struck on its journey.

In my detector I use five MCPs, each with a twelve degree bias angle and with the plates arranged in a Chevron-Z configuration. This arrangement places two plates together on the top of the detector with the channels forming a chevron when viewed from the side. The sharp turn of the connecting channels as the electrons traverse from one plate to the next increases the number of wall strikes yet again. The next three plates are pressed together with their channels forming a Z when viewed in a similar manner and separated from the first two by a small gap. Across

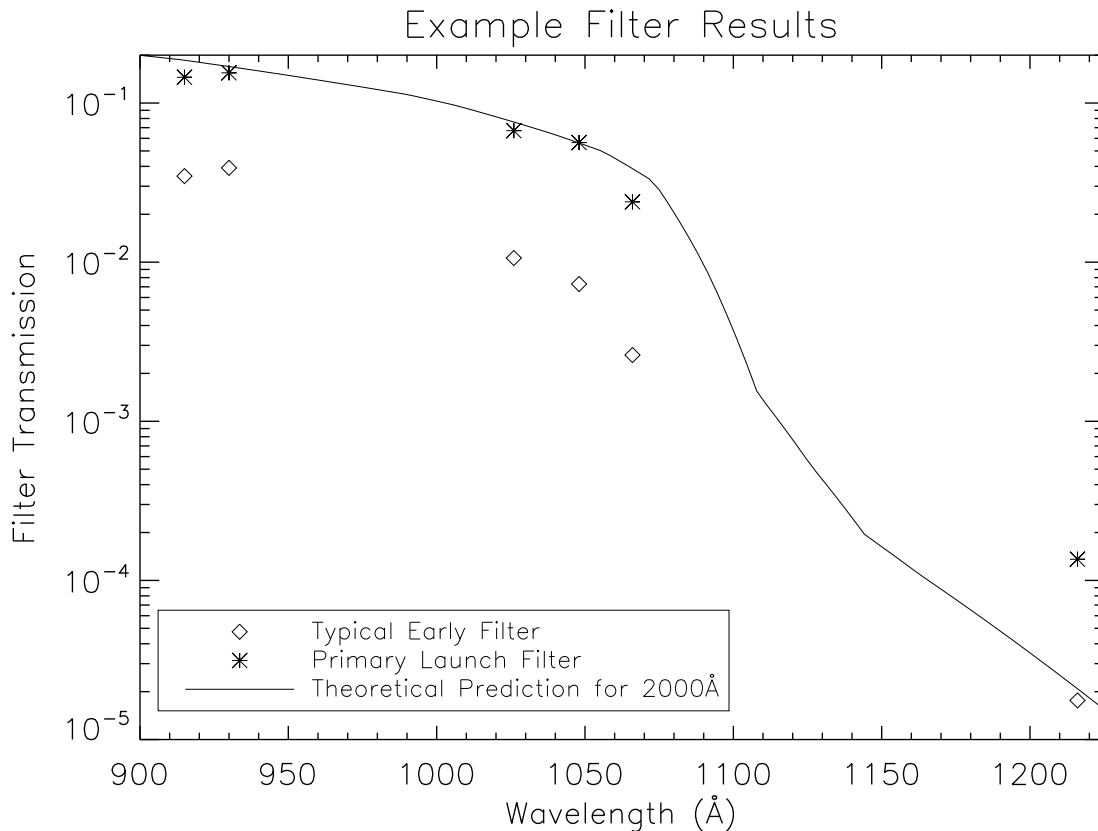


Figure 2.10: Transmission of the flight filter for FIRE, as well as the theoretical transmission for a 2000 Å thick filter and an early FIRE filter (pre-plasma cleaning) for comparison. While the goal was a 2000 Å thick filter, the fact that the Ly $\alpha$  transmission is higher than predicted indicates the filter is thinner than 2000 Å.

this gap is a small (a few hundred volts) potential in the reverse direction from the entire stack's main voltage. This reverse potential slows the electron cloud exiting the chevron plates and allows them to spread slightly before impacting the lower Z plates. This increases the number of channels electrons enter in these lower plates and the total gain of the system.

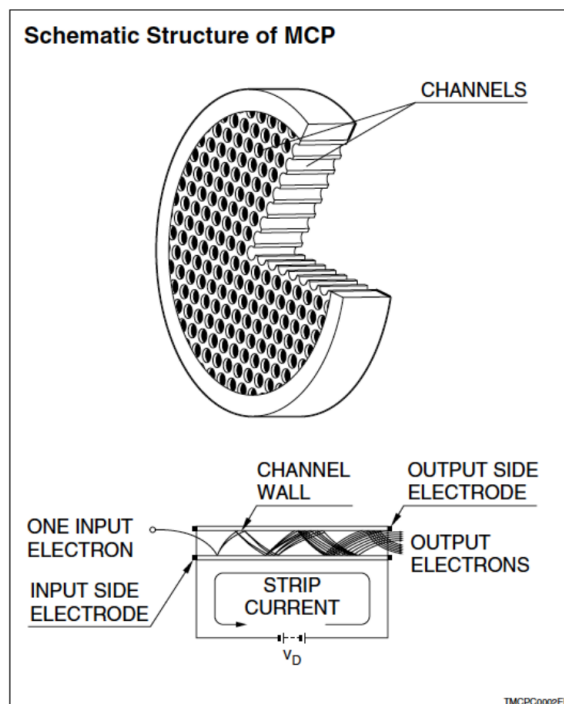


Figure 2.11: An example of the process of charge multiplication in a MCP. Electrons strike the walls of the pores, leading to more electrons being released and a cascade event that results in increased signal.

Directly in front (closer to the mirror) of the first MCP, I used a quantum efficiency grid. This copper mesh was charged to a more negative voltage than the first MCP. This helped any electron kicked off by a photon striking the MCP to be repelled back towards the plates, increasing the efficiency with which photons are turned into detectable cascades.

A bare glass MCP has a low chance of discharging an electron when struck with a photon, as little as two or three percent. Therefore, the top MCP is typically coated with a material with a higher photoelectric yield, often a salt. I chose to use a 1200 Å thick layer of rubidium bromide (RbBr); whose efficiency as a function of wavelength is shown in Figure 2.12 and is approximately

40% for the FIRE passband (Siegmond & Gaines, 1990). Not only did this choice enhance the efficiency of the device across the desired passband of 900-1000 Å, but RbBr responsiveness dropped quickly with wavelengths shorter than 900 Å, defining one side of the system's effective wavelength range.

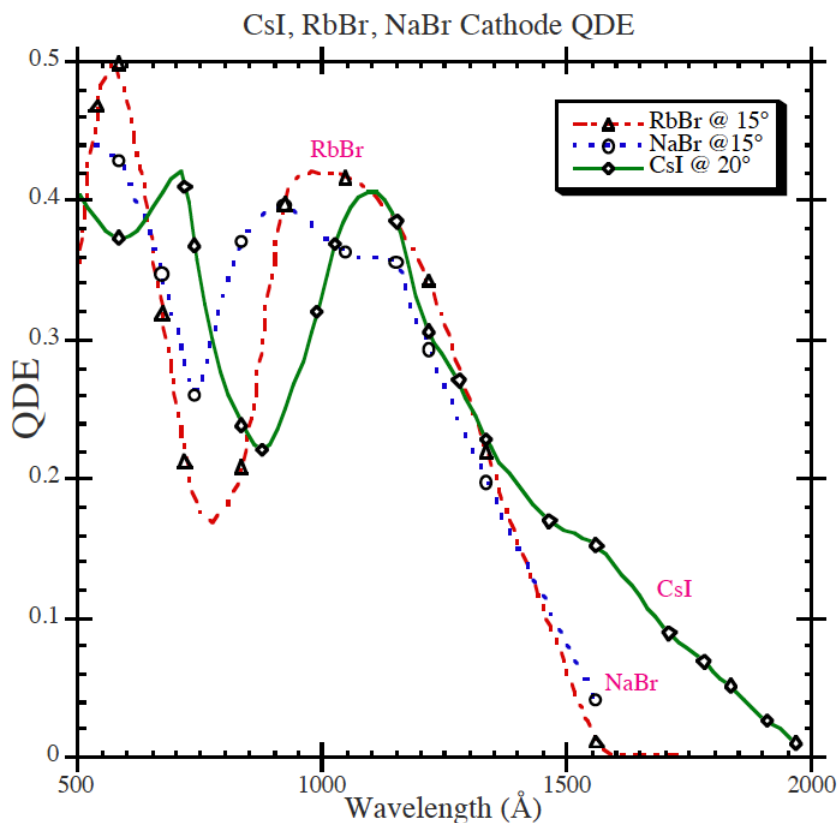


Figure 2.12: The quantum efficiency of a RbBr photocathode in a MCP detector (red line) (Siegmond, 2009).

Upon characterizing the detector during construction, I determined that 5200 volts was the optimal potential to put across these plates. This was the voltage needed to ensure that the pulse heights of actual counts was a distinct population from the electronics' system noise. The electronics were taken from a standard laboratory setup for this detector and modified for flight. First, the signal from each corner of the detector was fed through the bottom of the canister and along the arm to amplifiers mounted between the inner and outer skins. This trip was approximately eight inches and I used grounded insulation wires to ensure that there was minimal degradation of the

signal. These amplifiers were taken from the commercial Quantar package, physically cut into five circuit boards, rewired back together and mounted on a curved plate. The output from the amplifiers was then sent along the length of the telescope to the electronics section and a Quantar 2401 position analyzer. This is the same rack-mounted position analyzer used in the lab for MCP detectors. To save space and weight for flight, we removed the circuit boards and remounted and rewired them into a custom box that was mounted underneath the main electronics deck. The output of the position analyzer was two 10-bit words, one for X position and one for Y position, that was then passed directly to the digital telemetry and radioed to the ground.

The design of the detector was chosen such that each bit of data would cover  $25\ \mu\text{m}$  and the resolution element of the system would be  $50\ \mu\text{m}$ . With the 1.75 meter focal length of the mirror and the resistive anode of the detector being 25 mm square, this translates to 6 arcminutes/resolution element and a 49 arcminute field-of-view. These values were chosen to match the capabilities of the GALEX mission since the science goals require the combination of data from both instruments. However, when calibrated for flight, the position analyzer produced a digital circle that was 30 arcminutes in diameter with the desired resolution. With the choice of M51, however, this was acceptable and still captured the full galaxy in our field-of-view.

I also found that the MCPs purchased from Hamamatsu for flight were defective. When used in the detector, the plates elongated the signal in the direction of the pore bias, as shown in Figure 2.13. The flaw is likely due to a systemic manufacturing error since the effect was found in all ten Hamamatsu plates whether tested as a group or individually. They were replaced with proven MCPs from our stores that were flown instead.

## 2.5 Pre-flight Expectations

Figure 2.14 shows the image we expected to record during this first flight. One significant advantage of M51 was its high surface brightness compared to other possible targets. Since this was the first image in this passband, we decided to err on the side of caution and chose the highest surface brightness galactic target to ensure the best possible signal-to-noise. As figure 2.14 shows,

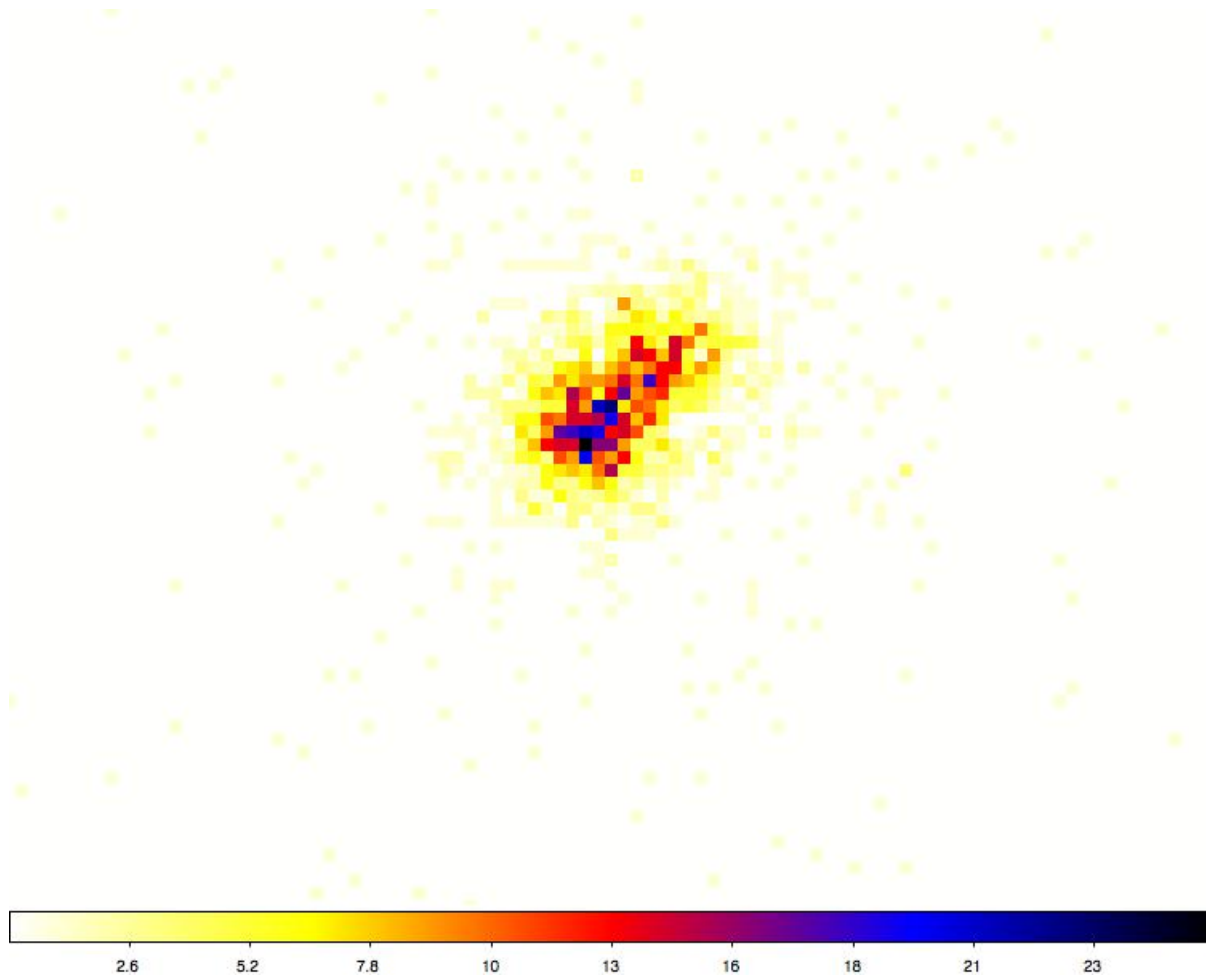


Figure 2.13: The recorded response of the initial detector MCPs when recording collimated radiation through a circular  $10 \mu\text{m}$  pinhole; each pixel is  $25 \mu\text{m}$ . The elongation occurs in the direction of the pore bias and was seen across all the Hamamatsu plates I obtained.

we expected S/N of greater than seven over the core and center of the spiral arms and a S/N of greater than two over the majority of the galaxy.

These expectations were based on a combination of FUSE data, GALEX data and pre-flight measurements of the telescope components. First, I gathered each FUSE and GALEX far-ultraviolet ( $1350\text{-}1750 \text{ \AA}$ ) observation of M51, as well as M31 and M81, the two other finalists for the first flight. Each of the 15 FUSE spectrums was matched to the pixels of a GALEX image, creating a photon/second (in our passband)-to-GALEX value. These 15 values were then fit linearly to create a complete table of conversion values. This table was used to convert the

GALEX far-ultraviolet image into an estimated 900-1000 Å image of M51. The image was binned to give the same angular value to each pixel as FIRE's expected resolution element (6 arcseconds across). Next, the expected reflection values of the mirror, the transmission of the indium filter and sensitivity of the detector were factored in to determine the expected recorded signal. Finally, a poisson distribution of anticipated noise in the form of Ly $\alpha$  and Ly $\beta$  was folded through the telescope system and added to the signal, creating the pre-flight image of FIRE's first flight (see Figure 2.14).

## 2.6 In-flight Specifics

FIRE launched from the Poker Flat Research Range north of Fairbanks, Alaska on January 28, 2011. Unfortunately, the flight did not go as planned. Several observations and decisions were made during flight that resulted in a mis-pointing of the telescope. In addition, a voltage anomaly compromised the data that was taken. While I did record the first ever 900-1000 Å image of an astronomical source, it was of Alkaid (a B3 star), not M51.

First, I had numerous sources of information during flight. Most important was the view of the ST5000 star tracker and the current pointing of the telescope. There were also several computer screens that showed the complete set of non-data telemetry sent from the payload in real-time. Finally, there were a bit decoder and PC that together took the X/Y positions of the detector data and displayed them to then screen in real-time as well.

Everything appeared fine for the first 77 seconds of flight. At 80 seconds, the canister door opened correctly and the resulting telemetry showed this. However, at that time we also noticed that the voltage readings for the payload (+/- 5V, +/- 15V and +/- 28V) were fluctuating quickly and with greater scale than was typical. It was difficult to tell exactly what values they were hitting; they were being sampled at 4000 Hz and the changing digits were the first indication that something was amiss. At 98 seconds, the high voltage system turned on and we immediately began receiving digital data telemetry indicating that counts were being passed through the system. However, at this time, it was discovered that the bit decoder that combined with the PC that produced the

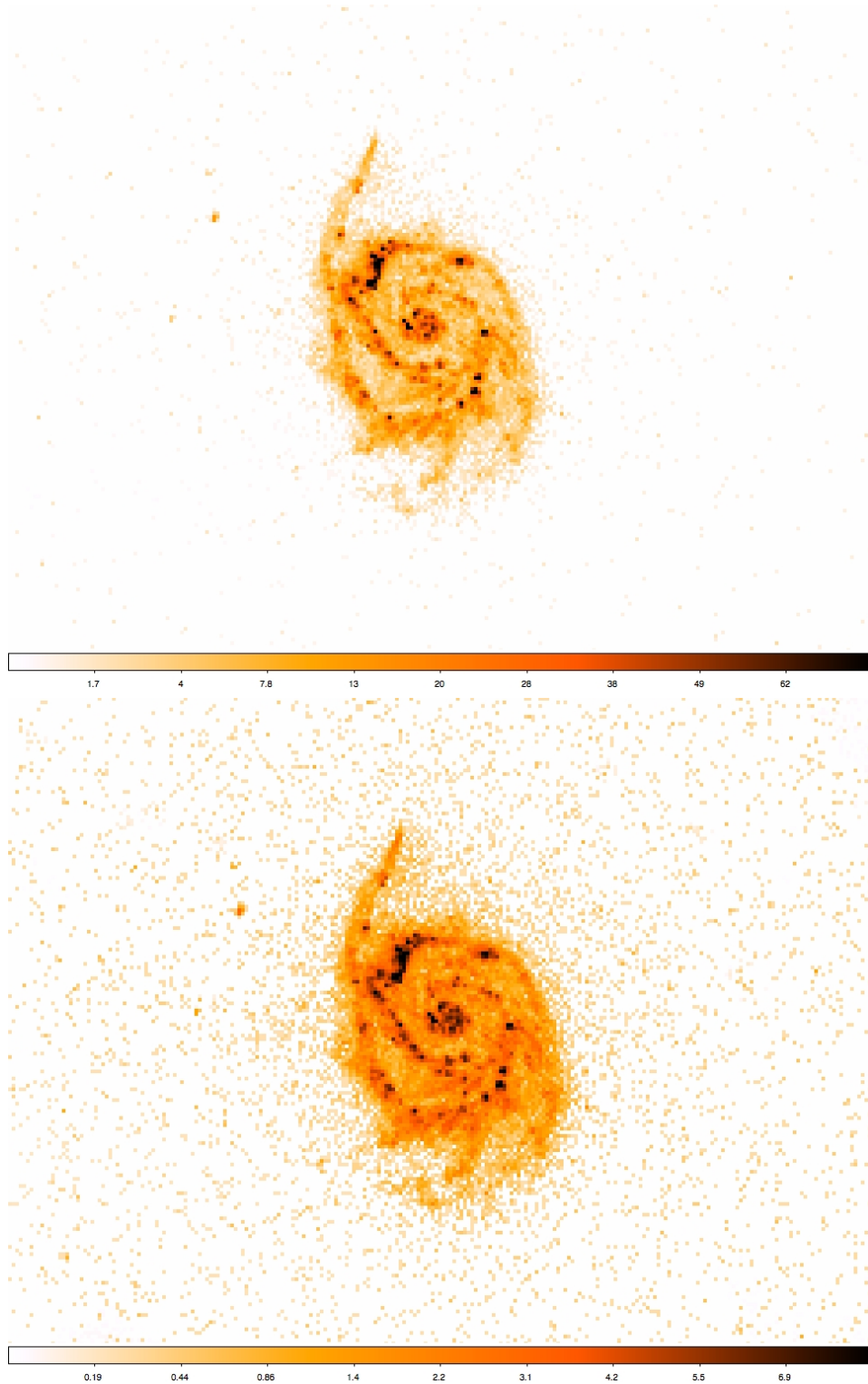


Figure 2.14: Expected counts for M51 (top) and the expected S/N (bottom) during the first flight of FIRE. This is based on a combination of previous spectra taken in our wavelength range with other UV images from GALEX and the efficiencies of the FIRE system.

detector image had failed. Numerous attempts were made by the responsible engineer to fix it, but he was unable to make any progress during flight. This left me only one indication to the state of the data collection, the telemetered count rate. By this time, we had arrived at the calibration target of G191B2B. However, the star tracker view showed no star in the telescope cross-hairs (in visible light) and the count rate of the detector was at 100 counts/sec instead of the expected rate of 10,000 counts per second. Since the telescope stayed on the calibration target for only 10 seconds, it was not possible to examine this discrepancy in detail, but at the time it appeared that something had gone wrong with the pointing of the system. During the 35 seconds it took to slew between targets and the telescope was sampling blank and random sky, I noticed that the count rate was now almost 1000 counts/sec. This was much higher than the expected background, but it was also higher than the rate at G191B2B, reinforcing the initial thought that we had not actually pointed at the calibration target. When the telescope arrived at M51 there was again no object in the cross-hairs of the star tracker and the count rate had not changed from the slew value of approximately 1000 counts/sec. Since the count rate should have increased by at least a few hundred counts per second from M51 flux, I was now convinced that there was a pointing error.

To prepare for this situation, I had gone to the Digital Sky Survey (DSS) and familiarized myself with the surrounding sky view. The DSS images should have been nearly identical to the star tracker with since they share a peak efficiency at 5000 Å. While the sensitivity of the star tracker was not going to be as good as the DSS, there were still several large stars in the immediate surroundings that would be visible in the star tracker and that could be used as guide stars. For use during flight, I printed this DSS image with a five degree by five degree field of view on a clear transparency. Since the star tracker had a seven degree (yaw direction) by five degree (pitch direction) field of view, this transparency could be held over the computer screen and, once physically scaled correctly, would match the size and aspect ratio of the images I would see in flight.

In flight, once I had concluded that we were not pointing at M51, I immediately grabbed the DSS transparency. Unfortunately, there were only two consistent objects in the star tracker view, with several that would flicker in and out with the static noise of the camera. The first was a

obvious star that was two pixels square and the second was what appeared to be a galaxy that was approximately 12 pixels square. The galaxy was also almost exactly three degrees away in the yaw direction. As described above in §2.1, the star tracker had been shimmed three degrees in yaw to account for the mis-cut telescope mirror. Thus, if a mis-pointing was going to occur in the system, a failure to properly account for the shimmed star tracker would be the most likely explanation. In addition, the other star was clearly identified in the transparency and was exactly the correct distance as expected from M51 as from this galaxy. I made the decision to slew the telescope to this new target. Immediately upon arriving there, the count rate of the detector shot upward. The rate settled at approximately 15,000 counts/sec, much higher than I had expected. However, this was the only real-time piece of evidence that the telescope was not looking at M51 and I concluded it was a combination of a greater efficiency of the RbBr photo cathode and a higher than expected flux from the galaxy.

The telescope remained on this target for the remainder of the flight. Since the rocket had not flown as high as expected, it began reentering the atmosphere before the high voltage system was disabled. Thus, from a steady value during mid-flight, the count rate exponentially fell until it reached zero for several seconds. After a few seconds, the count rate spiked to 100,000 counts/second, the maximum rate the electronics system could transmit. This was a result of the atmosphere pressure increasing to the point that the micro-channel plates had begun to arc and short the thousands of volts across them. Shortly thereafter the high voltage system automatically turned off and it appeared that the flight had been a success.

## **2.7 Post-flight Conclusions and Results**

Once all the information of the flight is combined and examined closely, the facts of the flight clearly differ from the in-flight conclusions. In short, there were three problems with the flight of 36.257: the voltage ripple present on all the electronic lines, the mis-pointing of the telescope, and the loss of the payload in the Alaskan wilderness. The voltage ripple also leads directly into the events that led to the mis-pointing problem.

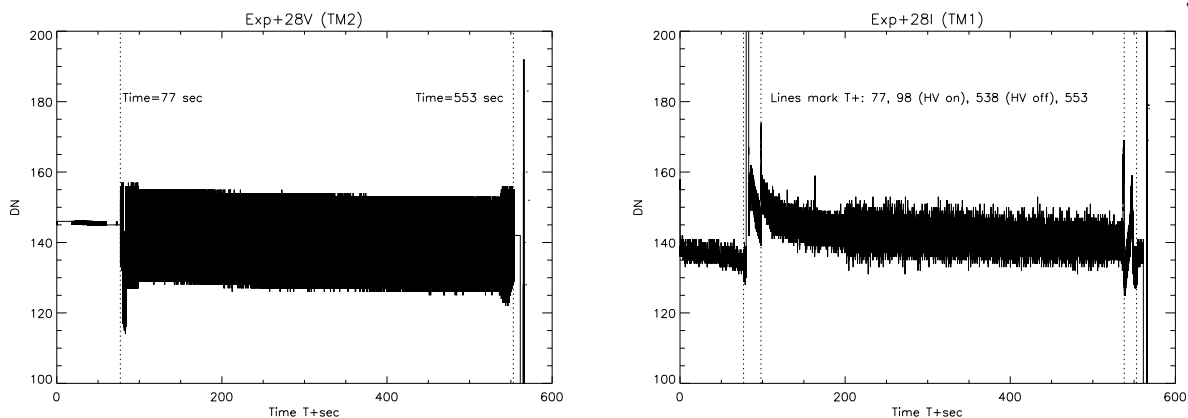


Figure 2.15: The recorded +28V instrument main power line monitor (left) in digital numbers (DN) and the current monitor on the same line (right). The anomaly start (77 sec) and stop (553 sec) times are marked as well as the high voltage system on/off.

First, there was a voltage ripple present on every voltage line in the scientific payload electronics (e.g. see Figures 2.15 and 2.16). While the amplitude varied slightly among lines, it began and ended on every line at exactly the same time,  $T+77.159$  seconds through  $T+553.736$  seconds. Since two separate voltage regulators, each supplied by two battery packs, powered the telescope, the ripple could not be a failure of the power system. In addition, nothing within the telescope oscillates except for the high voltage power supplies that were completely off during the first and last seconds of the anomaly (see Figure 2.15). The most convincing possibility is that something like a linear power supply partially failed within the NSROC half of the payload and put a several volt ripple onto the common ground plane of the rocket skin.

This voltage ripple had a major effect on the collection of detector data. With a peak-to-peak value of 1.5 volts and a frequency greater than the measurement rate of 4000 Hz, the voltage ripple could cause: a corresponding ripple in the high voltage power supplies and spurious counts, a partial failure of the 5 volt logic system of the detector position analyzer, corruption of the signal amplification at the pre-amplifier or a miscommunication of digital values to the NSROC radio. I am uncertain where exactly the failure occurred or if, more likely, it was a combination of several or all of them, but the practical result was a corruption of the image and the loss of a significant number of photon detections. As can be seen in Figure 2.17, a point source star has been

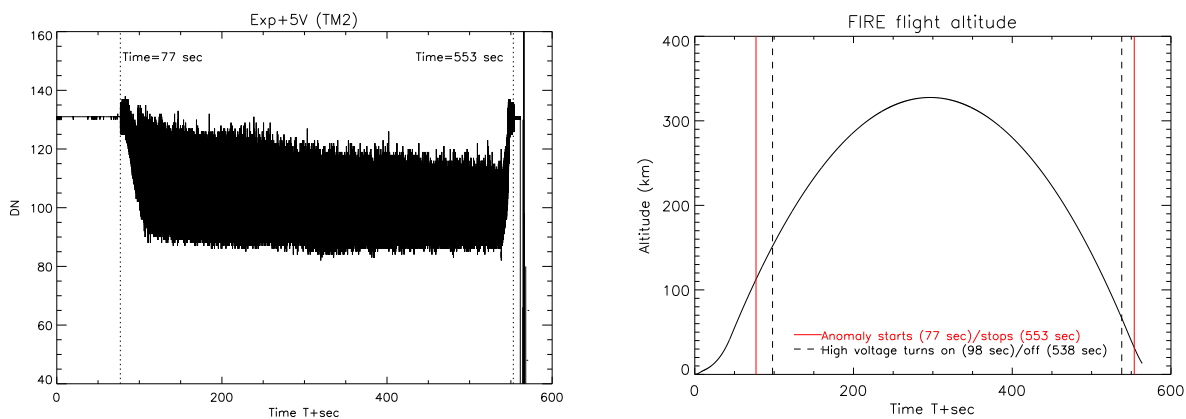


Figure 2.16: The recorded +5V instrument monitor in digital numbers (DN) during flight, with the start and stop times of the anomaly marked (left) and the altitude of the payload versus time, again with the anomaly and high voltage systems marked (right).

smearred in several directions and the background noise is obviously grouped into chunks at regular intervals. In addition, 21% of the total number of counts of the image occur at the 0,0 X/Y location on the detector, an obviously spurious result. I estimate the number of counts that should have been recorded by the star at several million per second. Since the recorded rate averaged 16,000 counts/sec, the telescope system was operating at a fraction of the effective sensitivity expected. With the atmospheric reentry and the corresponding count rate of zero followed quickly by the high voltage arcing of the full 100,000 counts/sec limit, the electronics were still operating well enough to pass along only true counts, albeit it a small fraction of them.

Once I had examined all the detector data and the telemetered voltages and currents, I could explain the steps that led to the second problem, the mis-pointing of the telescope. In truth, there was no failure in the pointing system in-flight. Upon careful examination of the star tracker data after the flight, it was determined that the telescope had correctly acquired G191B2B and M51 before I had slewed it 3 degrees in yaw to the B3 star Alkaid (eta Uma), the star shown in Figure 2.17. Unfortunately, several factors had to happen for this mistake to occur: a miscommunication on the expectations of the star tracker sensitivity and resolution, a loss of real-time detector data imaging and the unlucky placement of an alternative target in the one place that I could mistake for legitimate.

While it may seem especially unlucky that I did not capture much time on M51, the transfer to the star Alkaid ended up being a boon. The payload actually flew significantly lower than was expected and since all the power functions are based on timers, re-entered the atmosphere before the high voltage systems and data collection had ceased. In addition, while the voltage anomaly did not transmit the correct number of counts, it was very consistent in the number of counts it did record. I was therefore able to make what I believe is the first recording of UV extinction through the upper atmosphere as a function of altitude. Figure 2.18 shows the count rate per second for the end of the FIRE mission. As more atmosphere comes between the telescope and Alkaid the rate begins to decline until it reaches zero. Shortly thereafter, the rate spikes to the full 100,000 counts/second limit of the electronics. That marks the arcing of the detector high

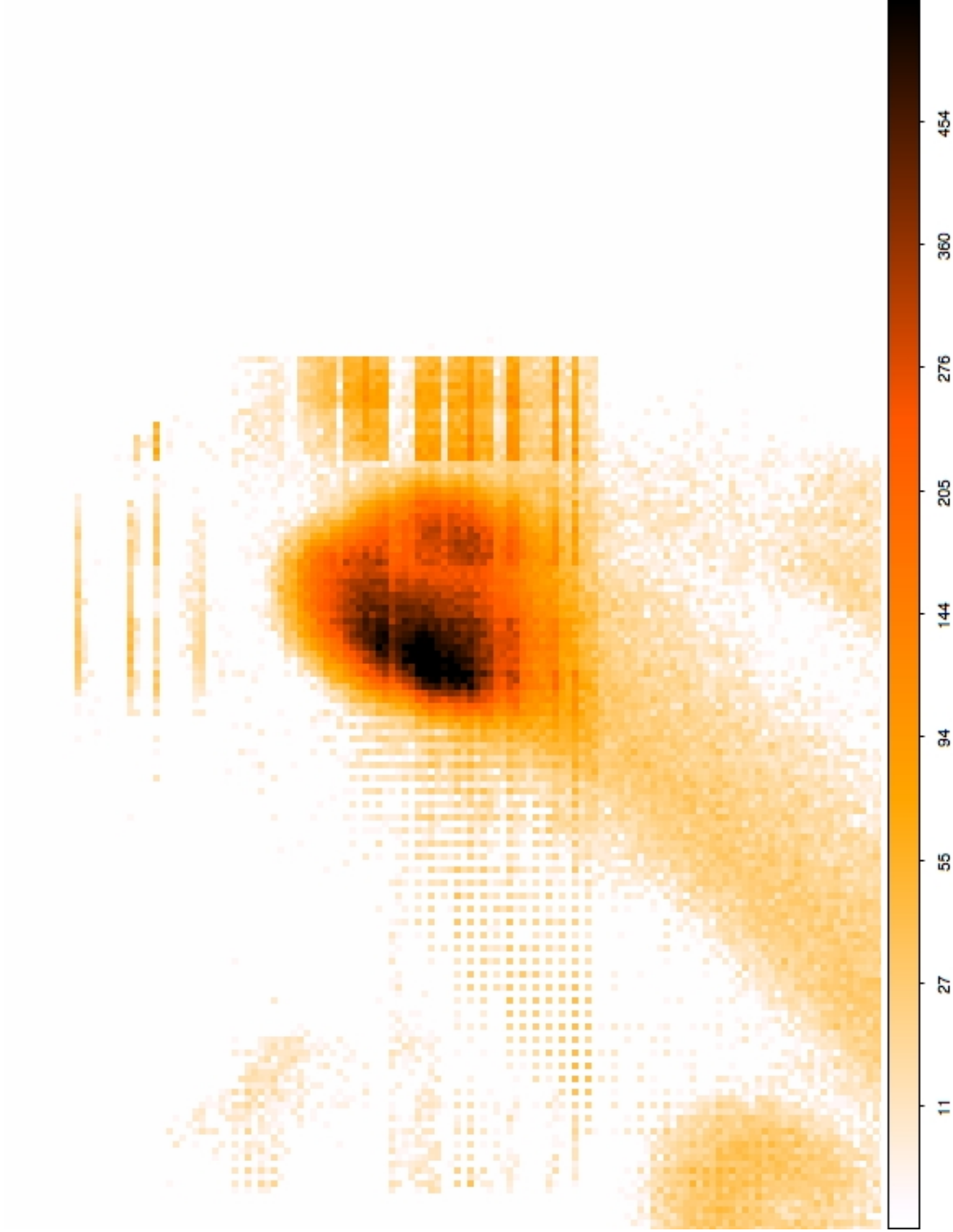


Figure 2.17: FIRE flight image of the B3 star Alkaid, the first ever astronomical image from 900-1000Å. Artifacts from the voltage ripple are apparent in the blocks around the star, the streaks leading down and left, as well as the blurring of the star itself.

volts because the pressure of the system has risen enough to allow current to bypass the plates and move through the atmosphere. That shows that the system was working consistently and that the previous measurements, while off on an absolute scale, still are believable on a relative scale. Figure 2.18 shows this attenuation as a function of altitude for UV flux from 900-1000 Å.

## 2.8 FIRE summary

Despite the problems listed above, most aspects of the flight were successful. The goals of this rocket were based around not only the science, but the engineering feasibility of the optical system needed to image astronomical sources at these wavelengths. We successfully demonstrated that the combination of the pure indium filter and a silicon carbide coated mirror can successfully survive launch and record images of 900-1000 Å. The vacuum canister was also successful in protecting the filter and opening during flight. In addition, despite the electrical issues, we still recorded the first ever image of an astronomical source at these wavelengths (see Figure 2.17) and the first recording of UV attenuation through the upper atmosphere (see Figure 2.18). A FIRE-type payload will fly again and many lessons from this flight can be applied to make a better instrument.

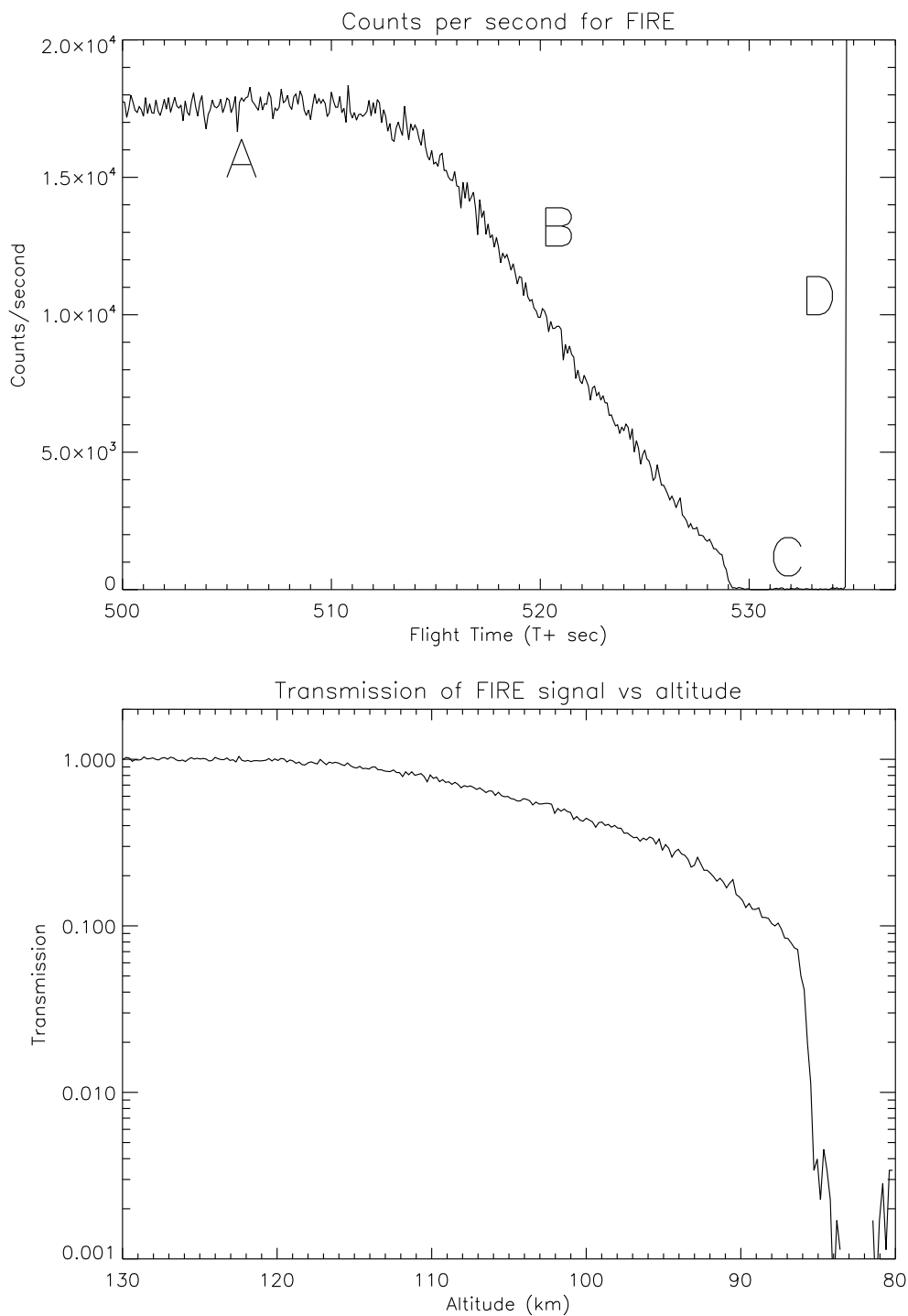


Figure 2.18: The counts per second for the end of the FIRE flight (top) and the attenuation of UV signal as a function of altitude (bottom). Region A marks the majority of the flight with a stable count rate. B shows the attenuation effects, dropping the count rate to zero at C. The spike upward at D shows the detector has enough ambient atmosphere to arc and helpfully demonstrates that the system was still working at this time.

## Chapter 3

### $\text{Ly}\alpha$ absorbers and nearby galaxies

Given the inability to retrieve significant levels of scientific data from the FIRE mission, I undertook a second scientific project for the data analysis portion of this thesis. I investigated the connection in the local universe between  $\text{Ly}\alpha$  absorbers seen in quasi-stellar objects (QSO) sightlines and galaxies near these absorbers. This study covered the CfA Great Wall of galaxies and the regions of under-dense galactic voids surrounding it ( $0.0035 < z < 0.07$ ). In §3, I discuss the background and history of this research, while §4 focuses on the data analysis and resulting conclusions I have drawn.

#### 3.1 Introduction to $\text{Ly}\alpha$ absorption in QSO sightlines

The study of hydrogen  $\text{Ly}\alpha$  absorbers within QSO sightline spectra has been going on for decades. Soon after being discovered, it was realized that they provided a powerful probe of the fundamental properties of the universe (Meiksin, 2009). However, only with the launch of the Hubble Space Telescope (HST) did this study enter the ultraviolet (UV) and the nearby universe. Almost immediately, it was found that the number of  $\text{Ly}\alpha$  absorbers was surprisingly high given extrapolations to the local universe from large redshifts ( $z$ ) (Morris et al., 1991; Bahcall et al., 1991). While this extrapolation predicted only 1-2  $\text{Ly}\alpha$  absorbers with a equivalent width ( $\mathscr{W}$ ) greater than  $\mathscr{W} > 50\text{m}\text{\AA}$  for a single QSO, Morris et al. (1991) actually found ten. A similar prevalence was quickly confirmed in other sightlines and the theoretical reason for their numbers elucidated (e.g. Davé et al., 1999). Observing hydrogen absorption in this manner allows us to

study gas that is up to six orders of magnitude less dense than the lower limit currently provided by comparable 21-cm techniques (Shull, 2002). When this gas was found to be relatively common, one of the first questions asked was whether it was pristine cosmic remnants of the Big Bang (true intergalactic medium, IGM) or the extended halo of galaxies.

Even before HST, Sargent et al. (1980) had postulated that Ly $\alpha$  absorbing systems with additional metal lines and higher neutral hydrogen column densities ( $N_{HI}$ ) are associated with galaxies, while clouds with lower  $N_{HI}$  trace the IGM. Leveraging the advantage that, at low- $z$ , galaxy populations can be studied to lower luminosity limits, Morris et al. (1993) was the first examination of this question using HST UV data and with a single QSO sightline concluded that a majority of low redshift Ly $\alpha$  absorbers were not intimately associated with luminous galaxies. Shortly thereafter, Lanzetta et al. (1995) used six sightlines and came to the opposing conclusion. They claimed that for  $z < 1$ , most luminous galaxies are surrounded by extended gaseous halos approximately  $160 h_{100}^{-1}$  kpc in size and that at least half of the Ly $\alpha$  absorbers arise from these halos. Three years later, Tripp et al. (1998) supported the IGM explanation and Chen et al. (1998) the galactic halo alternative. Since that time, numerous papers on each side of the debate have been published, notably Penton et al. (2002), Stocke et al. (2006), Chen & Mulchaey (2009), Wakker & Savage (2009) and Prochaska et al. (2011b).

In general, it appears that the debate is beginning to shift away from an exclusionary explanation to one where both explanations are valid. Wakker & Savage (2009) make a convincing case for a strong association between absorbers and galaxies, at least in the very local universe of  $z < 0.017$ . However, Penton et al. (2002) and Prochaska et al. (2011b) make an equally good argument that over a wider redshift range a significant number of these clouds are not galaxy halos. While Damped Ly $\alpha$  and Lyman Limit systems are generally associated with galaxies and their halos, the connection between Ly $\alpha$  systems with lower  $N_{HI}$  ( $N_{HI} < 10^{17} \text{ cm}^{-2}$ ) discussed here and galaxies is much less clear (Rosenberg & Putman, 2002). Thus, somewhat presciently, Sargent et al. (1980) may have been correct after all. There appear to be two populations of Ly $\alpha$  absorbers in the local universe, stronger ones that preferentially trace galaxy halos and weaker ones that

are IGM gas. While these distinctions may appear trivial, this is more than a simple question of semantics. The IGM is expected to be the main reservoir of baryons up to, and possibly including, the present age (Davé et al., 2010). A recent estimate of the distribution of the matter in the local universe by Shull et al. (2011) found that 53% of the local baryons are in the IGM and 18% are in galaxies, while 29% are still unaccounted for. Of that 53%, half is IGM that is relatively cooler in temperature ( $T < 10^5$  K) traced by these Ly $\alpha$  absorbers and the other half is the "warm-hot intergalactic medium" (WHIM) that has temperatures of  $10^5 < T < 10^7$  K measured through metal lines such as OVI. Thus, between a quarter and half of all baryons in the local universe can be studied directly by using Ly $\alpha$  absorbers and well-known galaxy locations to examine the relationship between Ly $\alpha$  absorbers and galaxies.

Since these baryons account for such a large fraction of the local universe, an accurate counting is crucial to the correct calculation of the cosmological  $\Omega_b$  (the fraction of baryonic density needed for a "flat" universe). Three primary ingredients go into this measurement (Shull, 2002; Savage et al., 2011): the  $N_{HI}$  derived from the Curve of Growth on Lyman series absorption, knowledge of the ionizing radiation field to derive photoionization corrections, and the physical density ( $n_H$  cm $^{-3}$ ) from independent observations of the hydrogen cloud sizes. Rosenberg et al. (2003) made an initial attempt to find sizes for several Ly $\alpha$  absorbers using the spread of their fingerprint in the spectra to determine their thickness in  $z$ . Unfortunately, since QSO absorption is based around pencil beam measurements that are limited to the background QSO placement, only rough maps, at best, could be created with this technique. In addition, the background flux of UV radiation that ionizes the hydrogen is also difficult to characterize since the UV spectral energy density cannot be reconstructed unambiguously from existing data (Fechner, 2011; Shull et al., 2011). However, the determination of the  $N_{HI}$  is possible to a high degree of accuracy with QSO absorption.

Hydrodynamical simulations of the local universe that focused on the IGM appeared not long after the Morris et al. (1993) discovery. Because the IGM is only detected in absorption and cannot be easily mapped, their physical structure must be modeled. The simulations help connect the study of low- $z$  Ly $\alpha$  absorbers with other branches of astronomy and cosmology. For example, it

was initially thought that low- $z$  absorbers represented a different population than their counterparts at a higher redshift, the first arising from galaxy halos and the second tracing the cosmic web of IGM (Bahcall et al., 1996). This was supported by connections between absorber-galaxy distance and  $N_{HI}$  (e.g. Chen et al., 1998). However, simulations (e.g. Davé et al., 1999) began to show that observations such as Chen et al. (1998) could be accommodated by having the higher  $N_{HI}$  tied to galaxies, while the lower  $N_{HI}$  followed their high- $z$  counterparts by tracing the IGM.

In addition, hydrodynamic simulations by Davé et al. (1999); Cen & Ostriker (1999); Davé et al. (2010) suggest that there should be a true IGM present in the local universe and that column densities derived from Ly $\alpha$  absorber observations are reasonable values for that gas. Davé et al. (2010) claimed that their results broadly confirm the theory that most Ly $\alpha$  absorbers trace large scale filamentary structures via highly ionized gas, at least Ly $\alpha$  absorbers with weak column density ( $N_{HI} < 10^{14} \text{ cm}^{-2}$ ). Other simulations (Sommer-Larsen, 2006; Fukugita & Peebles, 2006) predict galaxies surrounded by coronae that stretch hundreds of kpc outward and much less of a true IGM. It should be noted, however, that caution should be exercised in assuming that all, or any, of the IGM is “pristine” (unprocessed material from the Big Bang nucleosynthesis) as many of these simulations suggest. Studies by Songaila (2001) on the high- $z$  universe found CIV in all gas by  $z = 5.5$ , thus arguing that nothing in the local universe is pristine.

Study of the local IGM and Ly $\alpha$  absorbers covers numerous paths, not just the association with nearby galaxies; one of these is the WHIM. Ly $\alpha$  serves as an excellent tracer of the IGM as long as neutral hydrogen remains in the gas in reasonable quantities. As temperatures rise past approximately  $T > 10^5 K$ , the fraction of neutral hydrogen drops to the point that it becomes difficult to observe, although attempts are now possible with COS (e.g. Danforth et al., 2011). This transition is what is commonly used to separate the “cooler” IGM from the ‘warm/hot’ IGM, now called WHIM. Tracing the WHIM is typically done with absorption measurements of OVI, a transition that peaks between  $10^5 < T < 10^7$  K. Researchers will often combine the search for Ly $\alpha$  and OVI absorption lines since they are present in the spectra to the same QSO targets Tripp et al. (e.g. 2000); Tumlinson et al. (e.g. 2005). However, the fraction of absorbers with OVI lines

appears to be found preferentially near galaxies (Prochaska et al., 2011b); specifically within  $800 h_{70}^{-1}$  kpc from  $L_{\star}$  galaxies (Stocke et al., 2006). Tripp et al. (2006) shows that not every OVI absorber is intimately related to a galaxy, but only has two examples of this in their data set. This galaxy association is expected since large quantities of OVI are almost certainly the product of recycled galactic gas blown back out into space instead of nucleosynthesis during the Big Bang. Tripp et al. (2008) examines the relationship between  $\text{Ly}\alpha$  absorbers and OVI absorbers and finds that they trace the same gas with a high degree of confidence. In fact, Williams et al. (2010) reports finding two X-ray absorbers in a QSO absorption system and Savage et al. (2011) has found NeVIII lines, tracing probable galactic halos to even hotter temperatures. Thus, while I limit the analysis in this thesis to only  $\text{Ly}\alpha$ , the OVI absorbers I found are useful to the same field of study at higher temperatures and redshifts.

## 3.2 $\text{Ly}\alpha$ absorption and galaxies

Recognizing the outstanding questions of  $\text{Ly}\alpha$  absorber and galaxy associations and the implications for the local universe, I undertook a study of 11 QSO sightlines to find  $\text{Ly}\alpha$  absorbers within the CfA Great Wall of galaxies and the galactic voids surrounding it ( $0.0035 < z < 0.07$ , see §3.2.1) and the galaxies nearest to each absorber. The absorbers were found by using spectra from the recently installed Cosmic Origins Spectrograph (COS) onto HST, as in §3.2.3. I then used Dr. Steven Penton’s galactic database (Penton et al., 2002, 2004) to find galaxies within  $3 h_{70}^{-1}$  Mpc of the line-of-sight to the QSO, §3.2.2.

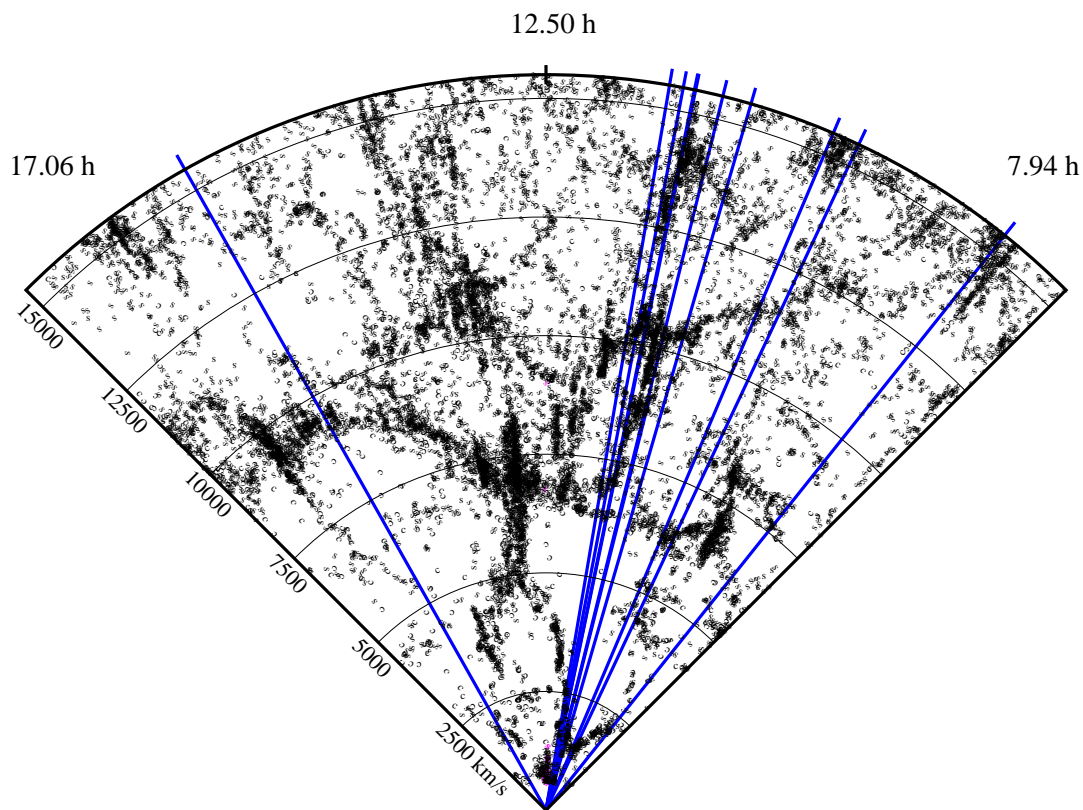
### 3.2.1 Great Wall of galaxies

The CfA “Great Wall” of galaxies was first discovered by galaxy surveys of Geller & Huchra (1989) (Figure 3.1 shows the portion of the Great Wall I covered). Geller (1997); dell’Antonio et al. (1996) demonstrated that the Great Wall is an actual two-dimensional structure and not just a artifact of the peculiar motions of the galaxies collapsing into a wall, the opposite of the well known “fingers of God” effect (see Geller (1997) for more details on this phenomenon). The

Great Wall is not perfectly perpendicular to our radial line-of-sight, but the region that I examined is well described by a redshift of  $0.015 < z < 0.03$ , with a noticeable density peak at  $z \simeq 0.02$ . The advantages of targeting this area of the universe are three-fold. First, the Great Wall is a volume relatively over-dense with galaxies. Second, immediately surrounding the Great Wall, from  $0.01 < z < 0.015$  and  $0.03 < z < 0.06$  are regions that are significantly under-dense in galaxies, galactic voids. Finally, these regions are close to the Milky Way and galactic surveys of them go to lower brightness limits of tenths of  $L_\star$ , a characteristic luminosity measure of galaxies (Blanton et al., 2003). For this paper,  $L_\star$  is calculated in the same manner as Penton et al. (2002). Specifically, using the Zwicky (or blue) band measurement, the magnitude is converted to a galaxy luminosity, where -19.57 magnitudes is equal to  $L_\star$  (Penton et al., 2002). More recent measurements from the Sloan Digital Sky Survey (SDSS) are converted to this band before  $L_\star$  calculations are made to ensure consistency. Since this investigation focuses on the association between absorbers and galaxies, the hypothesis that stronger  $N_{HI}$  clouds correlate more strongly with galaxies than lower  $N_{HI}$  can be rigorously tested with the highly contrasting regions of galactic-density.

### 3.2.2 Galaxy database

Dr. Steven Penton has compiled and maintains a galaxy database of the combined surveys of the Center for Astrophysics (CfA) and the Sloan Digital Sky Survey (SDSS or Sloan) and has generously assisted in this thesis study. All told, there are approximately  $1.5 \times 10^6$  galaxies in this database which has been used in numerous published papers (e.g. Penton et al., 2002, 2004; Stocke et al., 2006). One of the key components of this study is the association of the  $\text{Ly}\alpha$  absorbers to the nearest galaxy. However, bias can be introduced if regions are compared to each other that have differing levels of sensitivity to galaxy detection. Most obviously, the further one searches from Earth, the more difficult it becomes to detect fainter sources. Thus, during analysis, I am explicit about the limits of each population in terms of galaxy luminosity,  $L_\star$ . The database provides almost complete coverage of the  $0.0035 < z < 0.07$  range to a lower luminosity limit of  $L_\star$  for the eleven QSO sightlines (see §4.3 for details on absorbers that are left out of analysis for this reason). In



$\alpha$  wedge for  $\delta = 32.00 \pm 4.0^\circ$

Figure 3.1: A map of the local universe with nearby galaxies drawn from Dr. Penton’s database. Solid lines show the sightlines to the 11 QSO under study. Each galaxy in the CfA catalog is designated by a “c”, while each galaxy unique to the Sloan catalog is denoted by an “s”. The redshift analysis range,  $0.0035 < z < 0.07$ , is equivalent to  $1,050 < cz < 21,000$  km/second. The CfA Great Wall stretches from approximately 10,000 km/sec on the left, down through the middle to 6,000 km/sec in the lower right. Note the regions of low galactic density (voids) in the lower left, lower middle, upper left and upper right. Note: the declination wedge shown does not cover every sightline drawn on the plot.

addition, I also cut lower luminosity limits from the overall population to examine the differences that low-surface brightness (LSB) galaxies ( $0.1L_{\star} < L < 1L_{\star}$ ) induce in the results. Also, whenever a lower limit is set in this regard, all galaxies below that limit are discarded for that particular calculation. If this were not done, bias due to the more sensitive limits versus distance would be introduced by default. Other authors have mitigated this problem by taking their own galactic surveys, usually over one or two QSO sightlines (e.g. Rosenberg & Putman, 2002; McLin et al., 2002; Chen & Mulchaey, 2009; Prochaska et al., 2011a). These often have lower luminosity limits taken to a further distance, but over a limited field-of-view.

### 3.2.3 COS spectra

COS is the latest UV spectrograph installed on HST and while it has similar spectral resolution to a previous instrument (STIS), it has many times the sensitivity (for additional instrument details, see Froning & Green, 2009; Dixon, 2011; Green et al., 2012). Thus, even fainter QSOs can be used while achieving the same quality of data, a resolution of 20,000 (Green, 2001). Table 3.1 shows the targets used for this thesis, most of which have not been observed previously by UV spectrographs at these wavelengths. Another advantage of COS is the wavelength coverage, 1150Å to 1750Å in its far ultraviolet mode (using G130M and G160M, Green, 2001). While this thesis covers only 1220Å to 1300Å, the higher wavelengths were still searched for absorber systems. Discussed in detail in §3.3, the absorbers found at these longer wavelengths may have other resonance systems that appear in my studied wavelength range. Eliminating these spurious signals greatly increases the accuracy of assigning atomic transitions to absorption features in spectra. As a secondary check, Far-Ultraviolet Spectroscopic Explorer (FUSE, 905-1195Å) data was used whenever available. While the usefulness of this data was sometimes limited for these faint sources, in some instances I was able to confirm Ly $\alpha$  absorbers in the COS wavelength passband by matching them to Ly $\beta$ , other Lyman series or metal absorbers in the FUSE data.

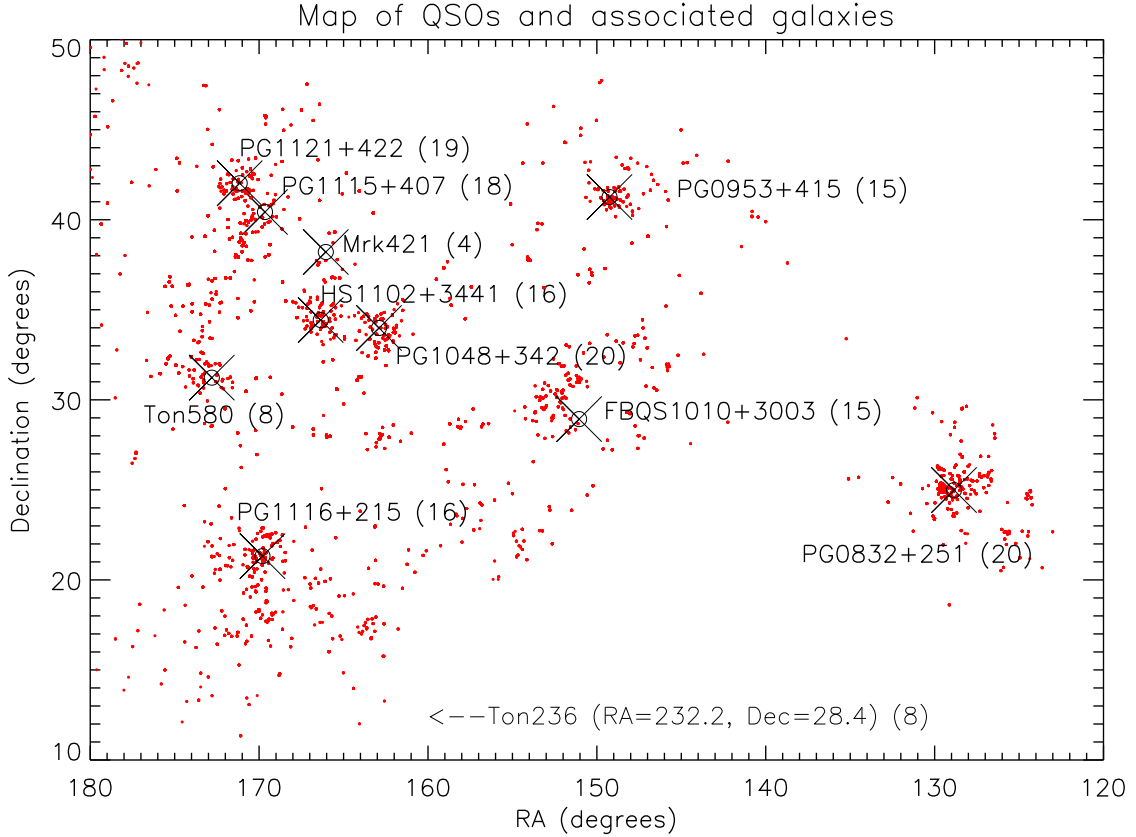


Figure 3.2: A sky map of the QSO sightlines and the galaxies within the 3 Mpc cylinder with them (red dots). Each sightline is labeled with the number of Ly $\alpha$  absorbers in parentheses. Ton236 is left off the plot for scaling reasons.

### 3.3 COS Data Reduction

The COS data analysis for this thesis followed a multi-step process that differs from the typical reduction of COS spectral data. Developed by Dr. Charles Danforth, this process starts

Table 3.1: A list of the QSO sightlines used and their availability in UV spectra before COS.

Target	RA (J2000) (h)	Dec (J2000) (deg)	$z_{target}$	Ly $\alpha$ absorbers ( $0.0035 < z < 0.07$ )	FUSE Y/N	FOS Y/N	GHRM Y/N	STIS Y/N
PG0832+251	8.59	24.99	0.330	20	Y	N	N	N
PG0953+415	9.95	41.26	0.239	15	Y	N	N	N
FBQSJ1010+3003	10.17	30.06	0.256	15	N	N	N	N
PG1048+342	10.86	33.99	0.167	20	Y	N	N	N
Mrk421	11.07	38.21	0.030	4	Y	Y	Y	N
HS1102+3441	11.09	34.43	0.509	16	Y	N	N	N
PG1115+407	11.31	40.43	0.155	18	Y	Y	N	N
PG1116+215	11.32	21.32	0.176	16	Y	Y	Y	Y
PG1121+422	11.41	42.03	0.225	19	N	Y	N	N
Ton580	11.52	31.23	0.290	8	N	N	N	N
Ton236	15.48	28.43	0.450	8	Y	N	N	N

with running the spectrum through the most current version of the CALCOS software available at the time, not the often outdated version available to MAST.

### 3.3.1 Co-adding Spectra, Continuum Fitting

Data sets for each target then needed to be coadded and a global continuum fit to the entire spectrum. The coaddition was done by matching galactic lines across exposures and interpolating onto a common wavelength scale (see Danforth et al. (2010) for additional details). To fit a global continuum, each spectrum was split into 5-10 Å segments. Within each of these, continuum pixels were identified by having a signal-ratio (flux/error) less than  $1.5\sigma$  signal-to-noise (S/N) of the segment. These continuum regions were then fit with a spline function that works well for smoothly-varying data. In areas of sharp spectral curvature, i.e. the Galactic Ly $\alpha$  trough, the spline was augmented with piecewise-continuous Legendre polynomial fits (see Danforth (2012) for more details).

Next, each potential absorber was fit with a Voigt-Hjerting (hereafter, voigt) profile convolved with the wavelength dependent COS line spread function (LSF, Kriss, 2011), revealing its intrinsic column density and internal gaussian velocity ( $b$ , temperature, hereafter referred to as Doppler parameter). The fitting of a voigt profile (the convolution of a gaussian and lorentzian, Hjerting, 1938) is acceptable if one assumes that the temperature and column density uniquely define the physical state of the absorption system (Tepper-García, 2006). If the doppler parameter ( $b$ ) exceeded 100 km/sec or showed obvious multiple components, I then attempted to fit multiple profiles to a single absorption feature since a cloud with a true 100 km/sec Doppler parameter ( $T > 6 \times 10^5$  K if it is fully temperature based) would ionize hydrogen almost beyond detection.

### 3.3.2 Noise and searching for absorption features

Once the absorption features had been identified, I checked to see if they were statistically significant compared with the noise. As is common (e.g. Penton et al., 2000b), I differentiated detections based on the “significance level” (SL) and kept all absorbers  $SL > 3\sigma$ . Detections above

$SL > 4\sigma$  are considered reliable, while those between  $3\sigma < SL < 4\sigma$  are treated as marginal. These marginal detections are kept through the rest of analysis but withheld from some data products to produce more statistically significant results. Unless otherwise stated, it can be assumed that the marginal detections are part of any conclusion or plot henceforth.

SL is based upon the more traditional signal-to-noise (S/N) calculation, but includes the contribution of the instrument resolution as well as the broadness of the source itself. Instead of assigning a gaussian probability to the value of a single pixel, it assigns a probability to an entire absorption feature. Thus, the cutoff of a  $SL > 3\sigma$  is a statement saying that the measurement is 99.7% ( $3\sigma$ ) certain is not noise.

SL is calculated based on the limiting equivalent width ( $\mathcal{W}$ ) of a feature that could be detected given the wavelength ( $\lambda$ ), resolving power of the instrument ( $R$ ) and S/N of the data (Ghavamian et al., 2009; Keeney et al., 2012).

$$SL = \frac{\mathcal{W} R (S/N)}{\lambda} \quad (3.1)$$

However, binning data can increase the S/N and reveal smaller absorption features. Thus, to increase the SL as much as possible, and observe the smallest equivalent width possible, I binned the data by the optimal number of pixels for the features I am searching for,  $x$ . This new pixel size ( $x \times \Delta\lambda$ , where  $\Delta\lambda$  is the pixel size in wavelength space) changes the above equation to:

$$SL = \frac{\mathcal{W} R_x (S/N)_x}{\lambda} \quad (3.2)$$

where  $R_x$  is the effective resolving power for these absorption features ( $R_x = \frac{\lambda}{x\Delta\lambda}$ ) and  $(S/N)_x$  is the S/N at this revised resolving power (Keeney et al., 2012). To find this optimal pixel size ( $x$ ), I started with the resolving power of the instrument ( $R \approx 18,000$ , Danforth et al., 2010) and found the corresponding doppler parameter to the instrument's resolution,  $b \approx 10$  km/second. Since we were looking at physical systems that were also broadened by internal processes, namely temperature and other non-thermal velocities, I needed an acceptable average value for these absorbers. Referring to Penton et al. (2000b) and others, I used  $b = 25$  km/second, a typical value. When these two doppler parameters were added in quadrature and reinserted into the above equations, I found that

the best effective resolving power of the instrument for observing these features is  $R_x \approx 7,200$ . This value goes directly into Equation 3.2 above and can be used to find  $x$  itself by

$$R_x = 7,200 = \frac{\lambda}{x\Delta\lambda} \implies x = \frac{\lambda}{7,200\Delta\lambda}$$

Thus, each absorber has an individual SL calculated based upon the revised  $(S/N)_x$  of approximately  $2 \text{ \AA}$  of available continuum on either side of the feature.

### 3.3.3 Identifying galactic sources and multiple component absorbers

Once I had a complete list of statistically significant absorption features for a spectrum, I searched the full wavelength range for known galactic lines. A list of common galactic lines is shown in Table 3.2, drawn from a variety of sources such as Penton et al. (2000b) and Wakker & Savage (2009), and based upon the atomic tables of Morton (2003). In addition, there are occasionally signals of high-velocity clouds that surround the Milky Way that are slightly redshifted from our local frame of reference. These clouds typically have redshift velocities of  $cz < 200 \text{ km/second}$  (Wakker & van Woerden, 1991); thus, at the  $1220\text{-}1300 \text{ \AA}$  range of this study,  $200 \text{ km/second}$  is  $0.5 \text{ \AA}$  of displacement from the equivalent galactic line. While it is possible to extract manually the nature of an absorption feature found in these ranges, I decided to err conservatively by ignoring any signal that could be a high-velocity cloud.

Once the galactic lines had been accounted for, I made the assumption that any remaining absorption feature represented a redshifted obscuration between us and the target QSO. I then began to search the entire wavelength range available for multiple component absorption systems. For example, for most  $\text{Ly}\alpha$  systems detected there will also be a  $\text{Ly}\beta$  feature ( $1026 \text{ \AA}$ ) at the appropriate redshifted wavelength. Since the  $\text{Ly}\beta$  signal will be approximately  $1/7$ th as strong, weaker  $\text{Ly}\alpha$  detections do not expect to lead to a matching  $\text{Ly}\beta$  feature at a statistically significant level. However,  $\text{Ly}\beta$ , and higher Lyman series components, are not the only features that may match a  $\text{Ly}\alpha$  system. Table 3.3 shows the fifteen most common extragalactic species for gas at this temperature that I searched each spectrum for. In matching  $\text{Ly}\alpha$  systems at higher redshifts,

I removed approximately one quarter of the absorption features in the target redshift ( $0.0035 < z < 0.07$ ) from consideration (see Figure A.2 for an example). One additional benefit of the COS instrument is that the extended wavelength coverage allows us to search for absorbers back in redshift far enough to ensure that they do not pollute our target range, often back to the source itself. It should also be noted that no absorbers intrinsic to the QSO source itself were used in the Ly $\alpha$  absorber collection.

Table 3.2: A list of the galactic lines removed from the spectra. Higher Lyman series lines (Ly $\beta$ , Ly $\gamma$ , etc.) can be present but are not listed here.

Lines Always Present		Lines Sometimes Present	
Atomic Species	Wavelength (Å)	Atomic Species	Wavelength (Å)
NI	1134.17	CIII	976.9
NI	1134.41	OVI	1031.9
NI	1134.98	CII	1036.3
FeII	1144.93	OVI	1037.6
PII	1152.81	FeIII	1122.5
SiII	1190.41	FeII	1133.67
SiII	1193.28	FeII	1142.37
NI	1199.54	FeII	1143.23
NI	1200.22	CI	1157.91
NI	1200.70	CI	1188.83
SiIII	1206.50	CI	1193.03
Ly $\alpha$	1215.67	CI	1193.99
SII	1250.57	NV	1238.82
SII	1253.80	NV	1242.80
SII	1259.51	CI	1277.25
SiII	1260.42	CI	1280.14
OI	1302.16	NiII	1317.22
SiII	1304.37	CI	1328.83
CII	1334.53	NiII	1370.13
CII	1335.66	NiII	1393.32
SiIV	1393.76	NiII	1454.84
SiIV	1402.77	NiII	1467.26
SiII	1526.70	NiII	1467.76
CIV	1548.20	NiII	1502.15
CIV	1550.78	CI	1560.31
FeII	1608.45	CI	1656.93
AlII	1670.78	NiII	1703.41
		NiII	1709.60
		NiII	1741.55
		NiII	1751.91

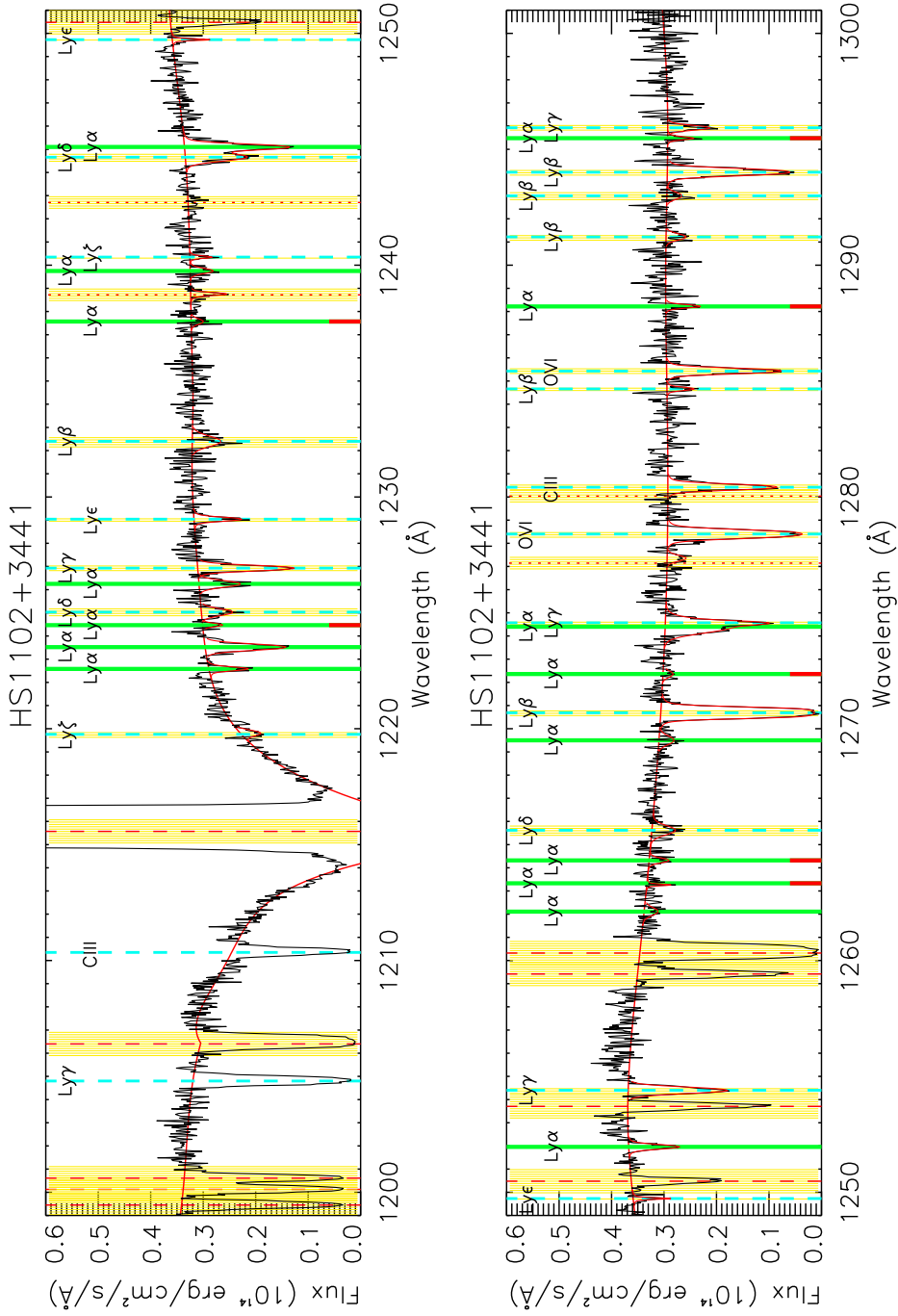


Figure 3.3: The  $0.0035 < z < 0.07$  (1220-1300 Å) range of the HS1102+3441 spectrum. Solid green vertical lines mark (and are labeled) Ly $\alpha$  absorbers, while dashed blue lines (also labeled) mark other Lyman or metal lines from Ly $\alpha$  absorber systems at higher redshifts. Ly $\alpha$  absorber green lines with a red marker at the bottom are “marginal” ( $3\sigma < SL < 4\sigma$ ). Red dashed and dotted vertical lines show the location of common galactic absorption lines, which are not always present. The red continuum fit is augmented by the voigt profile fit of each absorber. Finally, each non-Ly $\alpha$  feature is surrounded by a yellow box that denotes the region in which a Ly $\alpha$  absorber could not be found due to the obscuration. Note the large number of non-Ly $\alpha$  absorbers within the target wavelength region. Without the extended coverage of COS to larger wavelengths, absorption features such as these may be spuriously labeled Ly $\alpha$  and distort the population. The same plot for each QSO absorber can be found in the appendix.

With the non-Ly $\alpha$  absorbers removed from consideration, every remaining feature was designated as a Ly $\alpha$  absorber and kept for this study. Appendix A lists all 167 Ly $\alpha$  absorbers found across the 11 QSO sightlines from  $0.0035 < z < 0.07$ . The physical properties and the comparison to previous Ly $\alpha$  absorption studies will be discussed in the next chapter.

Table 3.3: A list of the Lyman and metal lines that I searched for at the same redshift as each Ly $\alpha$  absorber system. They are ordered from most likely to least likely to occur on a typical absorption feature. Higher order Lyman lines were checked when Ly $\beta$  or Ly $\gamma$  were present but are not listed here.

Atomic Species	Wavelength ( $\text{\AA}$ )
Ly $\beta$	1025.72
Ly $\gamma$	972.54
OVI	1031.93
OVI	1037.62
NV	1238.82
NV	1242.80
SiIV	1393.76
SiIV	1402.70
CIV	1548.20
CIV	1550.77
SiIII	1206.50
CIII	977.02
FeIII	1122.52
CII	1334.53
CII*	1036.34

## Chapter 4

### Analysis of Ly $\alpha$ absorbers and their nearby galaxies

This chapter covers the analysis of the Ly $\alpha$  absorbers found in the COS spectra and how they relate to nearby galaxies. As covered in §3, both of these studies relate to the nature of the IGM and, thus, the baryonic content of the local universe.

#### 4.1 The Ly $\alpha$ absorber population

All eleven COS spectra analyzed in this thesis contained Ly $\alpha$  absorbers. Table 3.1 lists the QSO sightlines and the number of Ly $\alpha$  absorbers found in each one, while Appendix A lists the complete set of Ly $\alpha$  absorbers found and their physical details. I found a total of 167 Ly $\alpha$  absorbers over a total pathlength of  $\Delta z = 0.618$ . Of those 167, thirty-five have a significance level between  $3\sigma < SL < 4\sigma$  and are considered marginal. Where possible, all the results have been replicated using only the reliable absorbers ( $SL > 4\sigma$ ) and found to be similar in nature to the results using the full set of absorbers. Thus, unless otherwise stated, it is assumed that the marginal detections are included in any data set or plot henceforth.

Each Ly $\alpha$  absorption feature found in a spectrum between  $0.0035 < z < 0.07$  ( $1220 < \lambda < 1300 \text{ \AA}$  or  $1050 < cz < 21,000 \text{ km/sec}$ ) was fit with a voigt profile. From that, I extracted the equivalent width ( $\mathscr{W}$ ), the doppler parameter ( $b$ ) and the column density ( $N_{HI}$ ). Figure 4.1 shows the distribution of the population for each parameter. The equivalent width is presented as the rest frame equivalent width for accurate comparison between redshifts. Rest frame equivalent width is simply the measured  $\mathscr{W}$  divided by  $1+z$  to account for feature broadening due to different redshifts.

There was one absorption feature that could not be fit well, 1236.9 Å of PG0832+251. This feature has been excluded from data products that require a column density, equivalent width or doppler parameter and is discussed in detail in Appendix A.

The means, medians and distributions of these values match previously published surveys well, notably Penton et al. (2004) and Wakker & Savage (2009). In addition, I have one QSO sightline that has been studied by multiple papers in the past, PG1116+215. Table 4.1 shows the Ly $\alpha$  absorbers found by myself, Penton et al. (2004) and Sembach et al. (2004). The agreement between my sample and the combination of Penton et al. (2004) and Sembach et al. (2004) is excellent. There are five new Ly $\alpha$  absorbers not seen by the two previous papers and the only Ly $\alpha$  absorber claimed by either that I did not find is the 1287.69 Å ( $\mathscr{W} = 15$  mÅ), a feature that registers on my search as a SL of  $2.9\sigma$ , just below the cutoff of  $3\sigma$ .

Table 4.1: A comparison of Ly $\alpha$  absorbers found on QSO sightline PG1116+215 for this study, Penton et al. (2004), and Sembach et al. (2004). Note: Sembach et al. (2004) did not list SL, so their  $\mathscr{W}$  is listed instead.

This study (Å)	SL ( $\sigma$ )	Penton 2004 (Å)	SL ( $\sigma$ )	Sembach 2004 (Å)	$\mathscr{W}$ (mÅ)
1221.68	30.8	1221.749	8.6	1221.66	95
1225.25	9.7	..	..	..	..
1235.49	38.1	1235.594	9.4	1235.55	113
1239.25	10.4	..	..	1239.05	40
1239.69	13.6	..	..	..	..
1250.06	52.5	1250.212	27.2	1250.04	219
1254.83	35.2	1254.989	8.8	1254.85	93
1265.63	20.5	1265.780	10.6	1265.82	81
1266.11	11.4	1266.474	5.4	..	..
1269.57	9.5	1269.606	8.3	..	..
1276.43	5.7	..	..	1276.31	30
1279.17	9.7	..	..	..	..
1283.72	4.4	..	..	..	..
1287.28	29.6	1287.438	20.0	1287.33	172
..	..	..	..	1287.69	15
1288.45	5.5	..	..	..	..
1289.45	8.3	1289.583	8.9	1289.49	85
1291.68	5.3	1291.754	4.8	1291.58	79

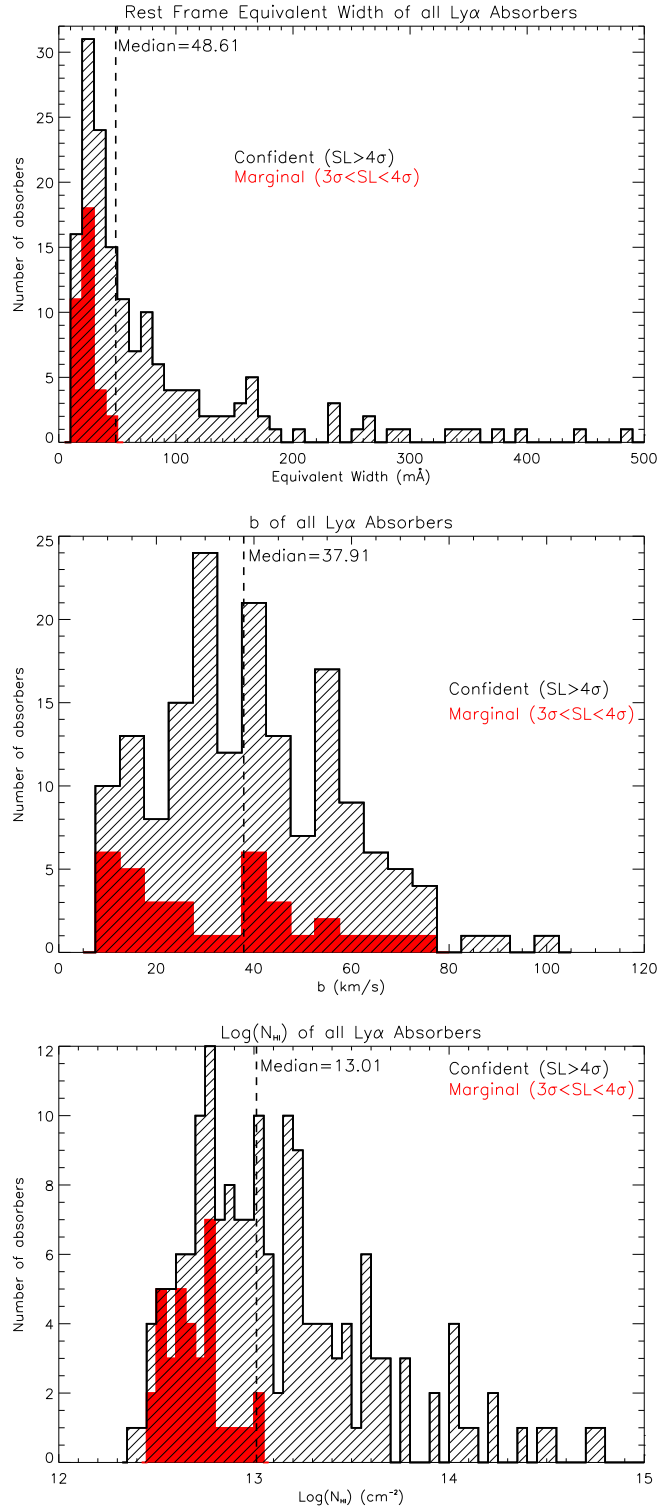


Figure 4.1: The distribution of rest frame equivalent widths ( $\mathscr{W}$ , top), doppler parameters ( $b$ , center) and column densities ( $N_{HI}$ , bottom) in the Ly $\alpha$  absorber population. Note: two equivalent widths (767.26 and 1977.28 mÅ) and one column density ( $\text{Log}(N_{HI})=18.75$ ) have been left off their respective plots for scaling purposes.

#### 4.1.1 Ly $\alpha$ absorber column densities and evolution with redshift

The  $N_{HI}$  number density per unit redshift and column density can be modeled by a power law,

$$\frac{\partial^2 \mathcal{N}}{\partial z \partial N_{HI}} \equiv n(N_{HI}) = C_H N_{HI}^{-\beta} \quad (4.1)$$

with an exponent  $\beta$  and constant  $C_H$ . Figure 4.2 shows the fit of this power law to the Ly $\alpha$  absorbers of this study and the fit found by Penton et al. (2004) for their sample. While Penton et al. (2004) detected a break in the population above  $\text{Log}(N_{HI}) \approx 14.5$  where the evolution with high column densities flattens, I have only a single absorber above  $\text{Log}(N_{HI}) > 15.0$  and cannot confirm that conclusion. Penton et al. (2004) used a constant value of  $b = 25$  km/sec to calculate the column density due to the large margins of error associated with a  $b$  measurement. However, since a majority of my absorber measurements of  $b$  fall on the more accurate “linear” portion of the curve of growth, I chose instead to use the measured fit values of  $b$  for these, and all following, results. As Figure 4.2 shows, the difference between the two populations and the two doppler parameter choices is within the margin of error of the power law fit.

While there have been numerous other Ly $\alpha$  absorber surveys and studies, I focus comparisons on two studies, Penton et al. (2004) (in combination with Penton et al. (2002)) and Wakker & Savage (2009), because they have the largest numbers of Ly $\alpha$  absorbers and also examine the absorbers’ association with nearby galaxies. Penton et al. (2004) found 187 Ly $\alpha$  absorbers while searching QSO sightlines over the same redshift space ( $0.002 < z < 0.07$ ) using the previous Hubble Space Telescope UV spectrographs, GHRS and STIS. Wakker & Savage (2009), in contrast, limited their search of Ly $\alpha$  absorbers to the very near universe,  $z < 0.017$ , to stay within the regions of the most complete galactic surveys. They did, however, include every sightline from the Hubble archive available at that time; seventy-six sightlines yielded 115 Ly $\alpha$  absorbers. In addition, the two studies arrive at contrasting conclusions about the Ly $\alpha$  -galaxy relationship. Penton et al. (2002) show numerous absorbers in galactic voids, while Wakker & Savage (2009) claims that every Ly $\alpha$  absorber can be matched to a specific galaxy if the galactic survey is complete enough. In

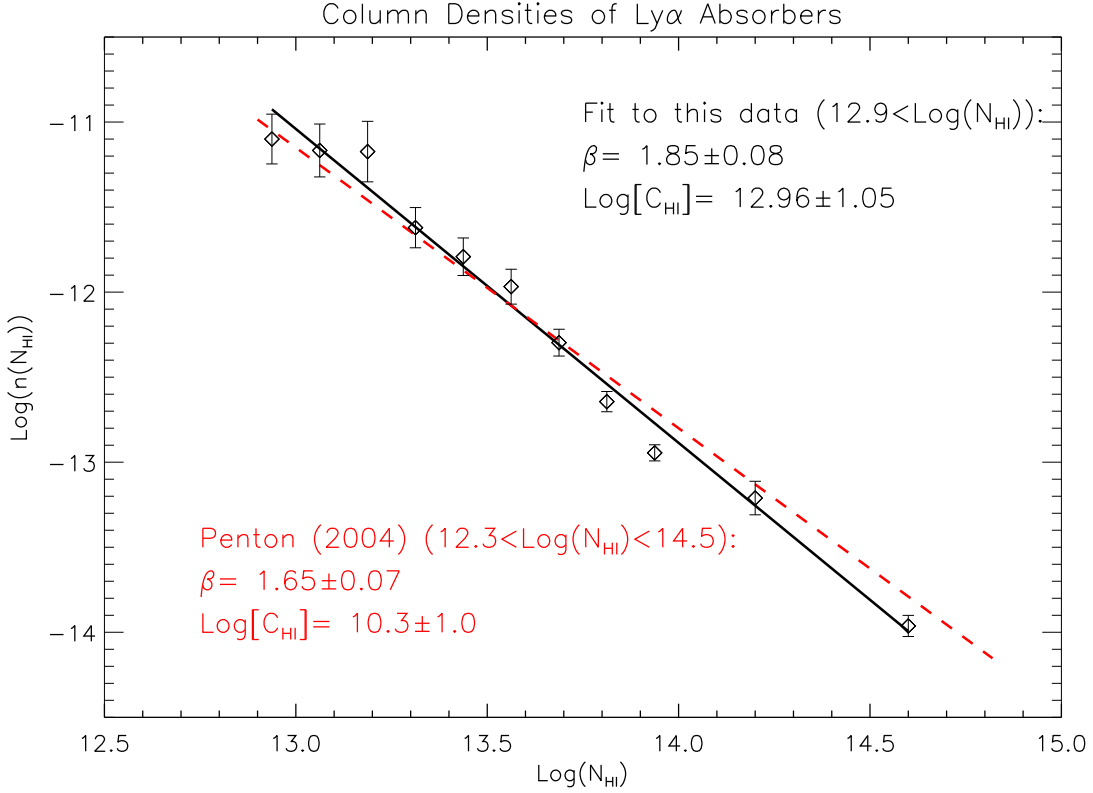


Figure 4.2: The distribution of column densities ( $N_{\text{HI}}$ ) in the Ly $\alpha$  absorber population per unit redshift and column density,  $n(N_{\text{HI}}) = \int \int (\partial^2 \mathcal{N} / \partial z \partial N_{\text{HI}}) dz dN_{\text{HI}}$ . The absorber population is truncated below  $\text{Log}(N_{\text{HI}}) < 12.9$  to adjust for the limiting detection sensitivity of the spectra. The fit to this data (black) is compared to the fit to Penton et al. (2004) data (red).

agreement with both Penton et al. (2004) and Wakker & Savage (2009), I find no evolution of either  $b$  or  $N_{\text{HI}}$  with redshift (see Figure 4.3).

#### 4.1.2 Two-point Correlation Function

The Two-Point Correlation Function (TPCF) is a commonly used method of determining the propensity for a population to group together. That is, are Ly $\alpha$  absorbers more likely to be found near other Ly $\alpha$  absorbers or by themselves? Previous authors (e.g. Ulmer, 1996) have shown an excess of Ly $\alpha$  absorbers with low separation velocities at higher redshifts and Penton et al. (2004) shows a similar grouping at low redshifts. Specifically, Penton et al. (2004) claims that the number of Ly $\alpha$  absorbers found within a recession velocity of  $\Delta v < 260$  km/sec of each other is  $7\sigma$  from

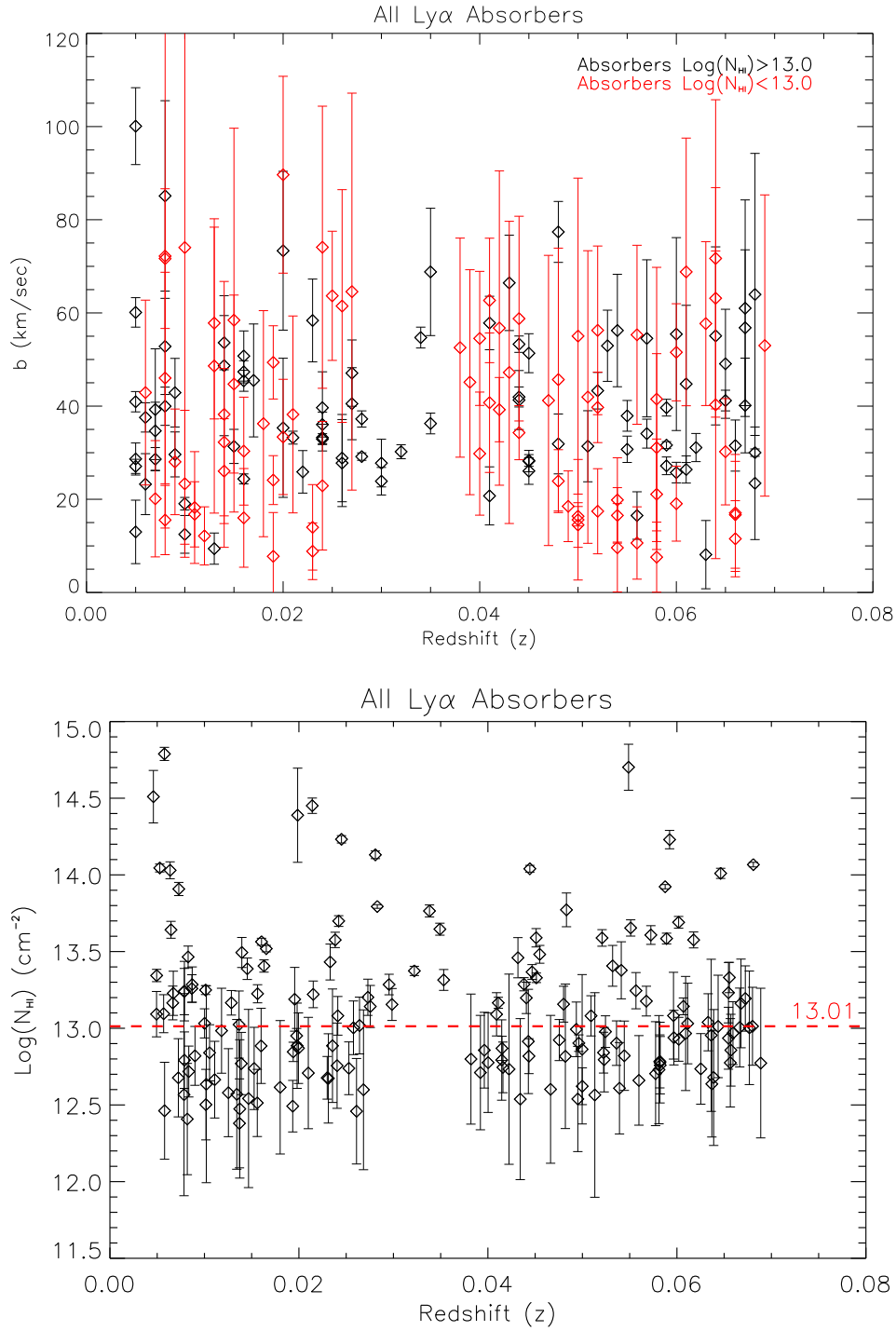


Figure 4.3: The distribution of  $b$  (top) and  $N_{\text{HI}}$  (bottom) versus redshift. Absorbers have been split into strong ( $\text{Log}(N_{\text{HI}}) > 13.0$ ) and weak ( $\text{Log}(N_{\text{HI}}) < 13.0$ ) based on the median value of the population ( $\text{Log}(N_{\text{HI}}) = 13.01$ ) marked with the red dashed line. Note: One column density point (PG0832 1236.9Å) has been left off the bottom plot for scaling purposes.

random, primarily due to higher column density clouds ( $\mathcal{W} > 68 \text{ m}\text{\AA}$ ).

The TPCF is the separation of any two absorbers along a QSO sightline, typically calculated in velocity.

$$\Delta v = \frac{c\Delta z}{1 + \langle z \rangle} \quad (4.2)$$

where  $\Delta z = z_2 - z_1 = (\lambda_2 - \lambda_1)/1215.67 \text{ \AA}$  and  $\langle z \rangle = (z_2 - z_1)/2$ . To determine whether the resulting distribution is significant, it must be compared to a similar situation populated by randomly located absorbers. However, these random locations must still account for the limitations that define the actual absorber search. For example, portions of the spectrum are removed from the search for Ly $\alpha$  absorbers by the presence of Galactic lines that would obscure any Ly $\alpha$  absorbers at that redshift from discovery. Regions are blocked off not only by Galactic lines, but also by the presence of a non-Ly $\alpha$  absorption feature or a Ly $\alpha$  feature already present. In addition, not all spectra are sensitive to small column densities due to larger noise components. Thus, the probability of a random absorber of a given  $N_{HI}$  appearing at a given wavelength is

$$P(\lambda) = \int_z \int_{N_{min}}^{\infty} \frac{\partial^2 \mathcal{N}}{\partial z \partial N_{HI}} dN_{HI} dz . \quad (4.3)$$

Here,  $\mathcal{N}$  is the number of absorbers over a given interval  $\partial z$  and within a given  $N_{HI}$  range of  $\partial N_{HI}$ . Since there is no evolution of absorber population with redshift (see §4.1.1), the redshift integral can be approximated by the redshift width ( $\Delta z$ ). For use in generating random absorbers, the function  $\frac{\partial \mathcal{N}}{\partial N_{HI}}$  is taken from §4.1.1 power law fit to the absorber population of

$$\frac{\partial^2 \mathcal{N}}{\partial z \partial N_{HI}} \approx \frac{\mathcal{N}}{\Delta z \Delta N_{HI}} = C_H N_{HI}^{-\beta} = 10^{11.47} N_{HI}^{-1.74} \quad (4.4)$$

Once the random population of absorbers is placed along a sightline, it is measured by the same Equation 4.2 as the real absorbers. This process is repeated 10,000 times and the results averaged into our “random” TPCF population. Figure 4.4 shows the distribution of both the observed absorbers and the random population when binned by velocity separations of  $\Delta v = 100 \text{ km/sec}$ . Unlike Penton et al. (2004), there is no general excess or decrement at low velocity separations ( $\Delta v < 500 \text{ km/sec}$ , see Figure 4.5). While the spike at  $\approx 15,000 \text{ km/sec}$  appears

significant, when other bin sizes are used the spike is diminished while the match between the observation and random populations at low velocity separations remains constant.

To create a better comparison to the random population, the additional TPCF function  $\xi$

$$\xi(\Delta v) = \frac{N_{observed}(\Delta v)}{N_{random}(\Delta v)} - 1 \quad (4.5)$$

is calculated. Here  $N_{observed}$  and  $N_{random}$  refer to the number of pairs in each velocity bin ( $\Delta v$ ) respectively. This shows the fraction above or below the random population that each velocity bin ( $\Delta v$ ) contains. Figure 4.6 shows the TPCF  $\xi$  function for the Ly $\alpha$  absorbers and the  $1\sigma$  and  $2\sigma$  significance level cutoffs for each bin.

While Penton et al. (2004) found an excess of absorbers at small separations, the majority of these came from the stronger half of the Ly $\alpha$  equivalent widths of their sample. To examine this possibility, I followed the prescription in Penton et al. (2004) and removed the weaker equivalent widths. Since the median value for my sample differs from Penton et al. (2004) and, thus, we use different strong/weak cutoff equivalent widths, both values are examined in Figure 4.5. While not as pronounced as the Penton et al. (2004) data, there is a significant excess of strong Ly $\alpha$  absorbers (by both measures) at  $\Delta v < 250$  km/sec in my data (see Figures 4.6 and 4.7). In addition, when a stronger equivalent width cut is made ( $\mathcal{W} > 80$  mÅ), the low velocity separation excess becomes even more pronounced. Thus, while my data agree with the general conclusion that stronger Ly $\alpha$  absorbers preferentially group at small velocity separations as postulated by Penton et al. (2004), I find the excess above a random population to be less significant and dominated even more by higher equivalent width absorbers. This lower excess agrees more closely with higher redshift studies such as Rauch et al. (1992) and Ulmer (1996).

## 4.2 Hits and Misses in the Great Wall

To directly examine the possibility of a filament of Ly $\alpha$  absorbers at or near the CfA Great Wall of galaxies, I started with a fairly simple approach of determining where exactly the Great Wall lies for each sightline and checking to see if there was an absorber there. However, even though there

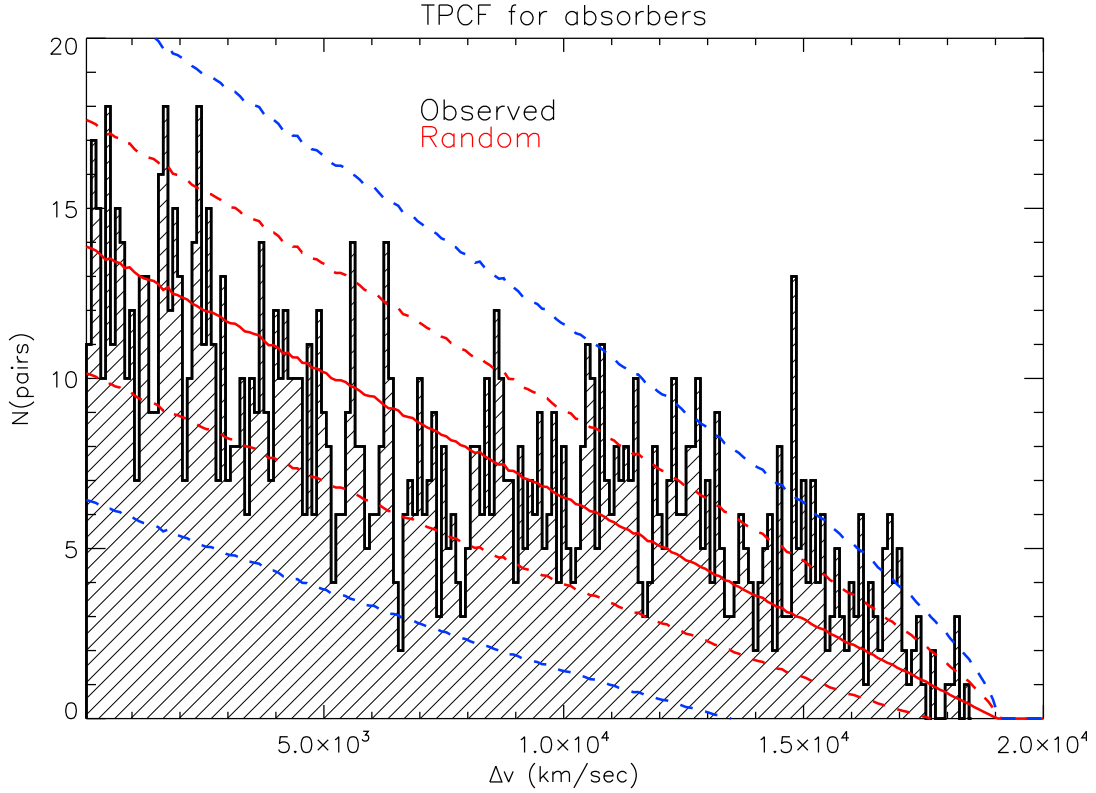


Figure 4.4: The Two-Point Correlation Function (TPCF) for the number of pairs of observed absorbers (black) and a random population (red) against velocity separation ( $\Delta v$ ) bins of 100 km/sec. The red and blue dashed lines represent the  $1\sigma$  and  $2\sigma$  limits respectively. When bin sizes other than 100 km/sec are used, the spike at  $\approx 15,000$  km/sec drops to near or below the  $2\sigma$  cutoff.

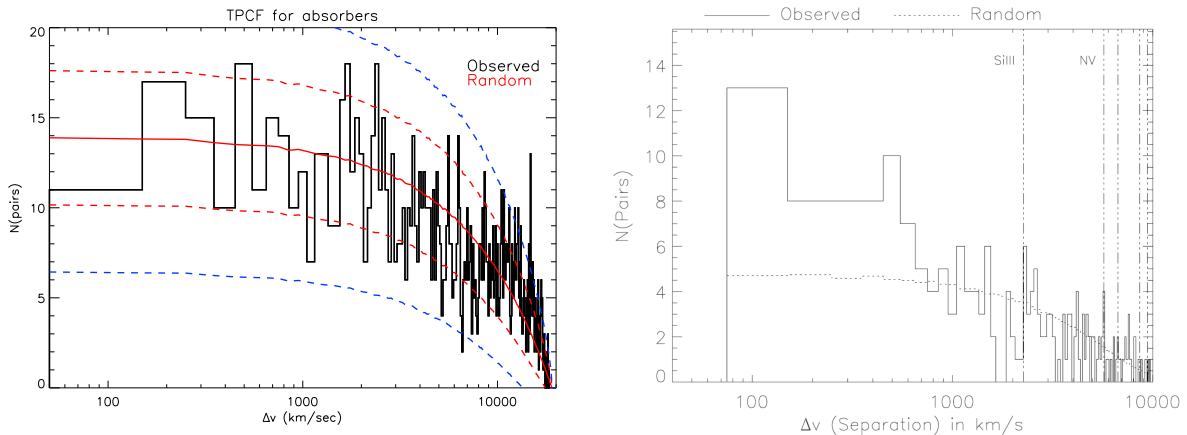


Figure 4.5: The same data as Figure 4.4 on a log scale (left) and the same measurement taken by Penton et al. (2000a) (right) (a subset of the Penton et al. (2004) data). Penton et al. (2000a) shows an excess of pairs  $\Delta v < 500$  km/sec, while my data has no significant excess at any separation.

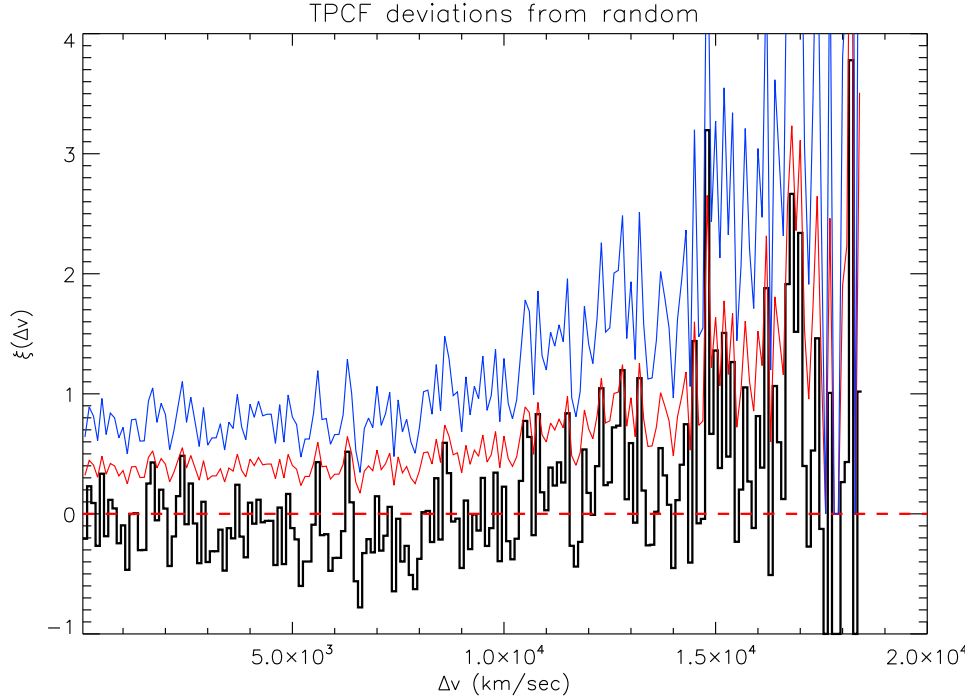


Figure 4.6: The Two-Point Correlation Function (TPCF)  $\xi$  for the data presented in Figure 4.4. The red dashed line emphasizes the value where the random and observed populations match in the  $\xi$  function. The red and blue lines represent the  $1\sigma$  and  $2\sigma$  significance level cutoff respectively of each bin. While the values above  $\approx 14,000$  km/sec appear large, they are dominated by low number statistics and none passes the  $2\sigma$  confidence level.

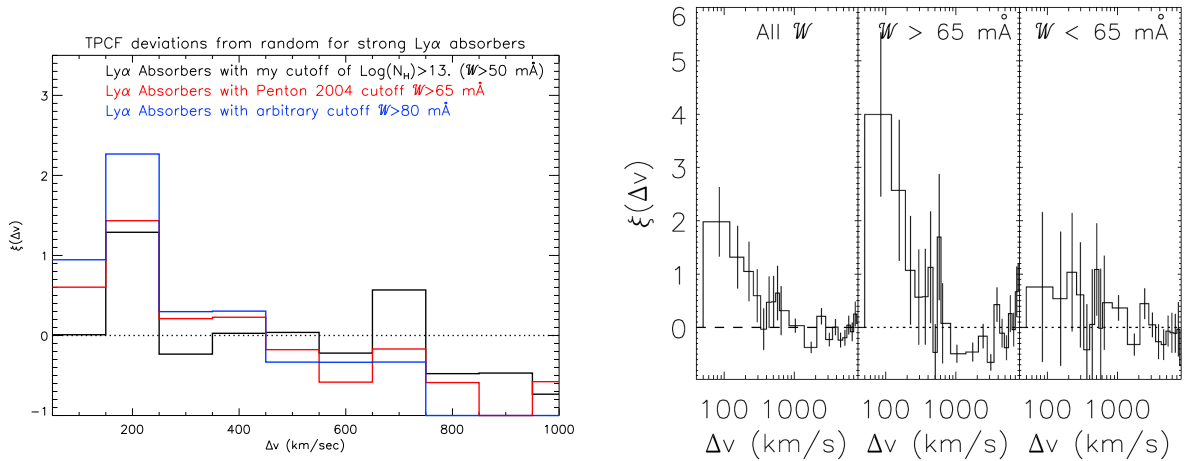


Figure 4.7: TPCF  $\xi$  function for all strong Ly $\alpha$  absorbers from my data (left) and Penton et al. (2004) (right plot, middle segment). While not as pronounced as the Penton et al. (2004) data, there is a significant excess of strong Ly $\alpha$  absorbers (by both measures) at  $\Delta v < 250$  km/sec in my data. In addition, when a higher equivalent width cut is made (blue line), the excess becomes even more pronounced.

is a large over-density of galaxies in the Great Wall, when pencil beam observations are taken, the number of galaxies along those lines-of-sight can still appear to be quite low. I therefore calculated the density of galaxies in the co-moving  $3 h_{70}^{-1}$  Mpc cylinder along each sightline to determine the maximum galaxy density in redshift for each observation. Figure 4.8 shows three of these sightlines in the Great Wall region and the location of Ly $\alpha$  absorbers. The number of galaxies are the solid plotted lines, while the Ly $\alpha$  absorbers are shown in the vertical green lines.

In addition, to create a consistent measure, the sensitivity of each QSO pathlength must be examined as well. To measure this, I stepped through each data point of the eleven sightlines and subtracted a gaussian function (with a  $b = 25$  km/s) at that location. I then measured the significance level of the resulting spectrum in the same manner as I would for a true absorption feature. The strength of the gaussian was incrementally increased until that SL exceeded the marginal cutoff. The resulting measurement of the column density gave a lower detection limit at that location. Since the noise can vary over the spectrum range of 1220-1300 Å, there are small variations in this value along each pathlength, however, these are typically  $< 0.1$  in  $\text{Log}(N_{HI})$ . The worst sensitivity had a detection limit of  $\text{Log}(N_{HI}) = 12.9$ , therefore, to be consistent along the lines of sight, I cut all absorbers below that value.

While every QSO sightline has a peak of galactic density at some point in the typical Great Wall region ( $0.015 < z < 0.030$ ), determining whether an absorber that is near the peak, but not directly on top of it, is “within” the Great Wall is somewhat arbitrary. Therefore, I created three levels of discrimination to determine the boundaries of the Great Wall along each sightline and create a consistent and binary check. While these three boundary conditions themselves are somewhat arbitrary, they can be roughly categorized as “narrow” ( $+/- 300$  km/s from the peak of galaxy density), “medium” ( $> 50\%$  of the peak of galaxy density), and “wide” ( $> 20\%$  of the peak of galaxy density). In addition, since two of the QSO sightlines are displaced from the tighter clustering of the other nine (PG0832+251 and Ton236), to ensure they were not biasing the sample, the summation is performed on the full sample as well as only the tightly clustered nine (hereafter called the “grouped nine”).

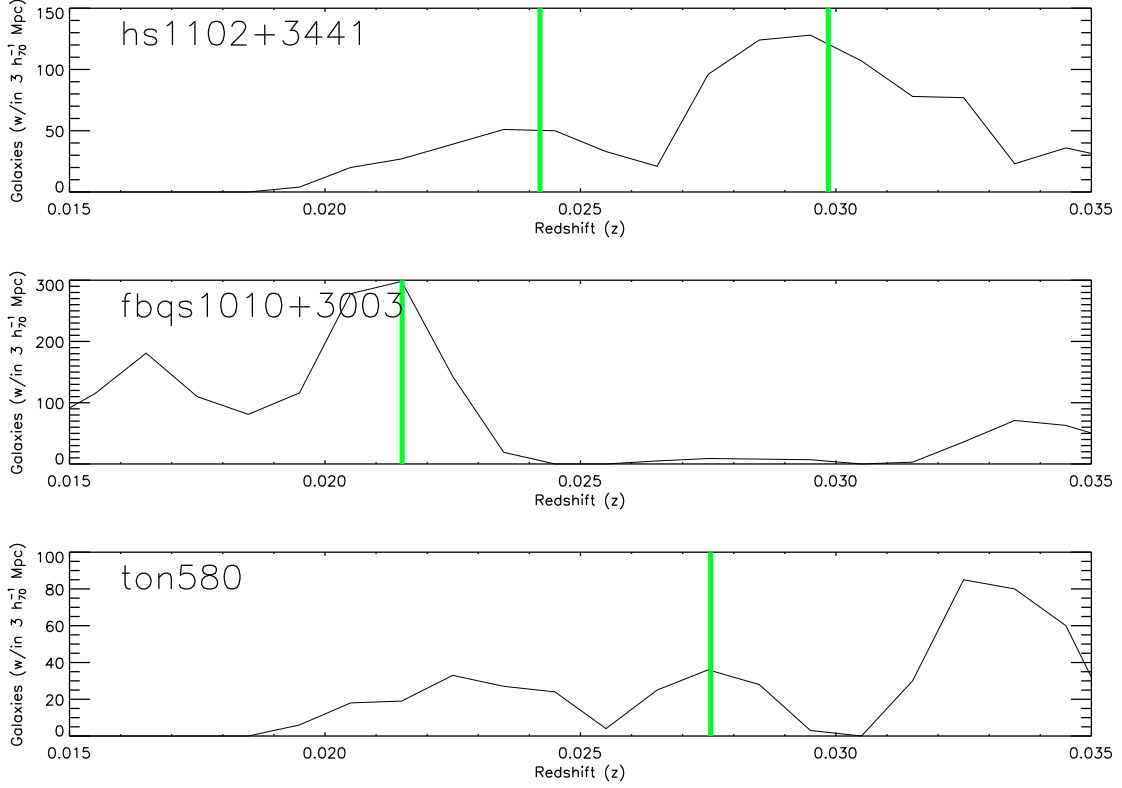


Figure 4.8: Three sightlines through the Great Wall region with  $\text{Ly}\alpha$  absorbers with  $\text{Log}(N_{\text{HI}}) > 12.9$ . The solid black lines are the number of galaxies within  $3h_{70}^{-1}$  Mpc cylinders as you move outward in redshift space. The vertical green lines are  $\text{Ly}\alpha$  absorbers specific to that sightline. As discussed in the text, a “hit” of a  $\text{Ly}\alpha$  absorber aligned with the Great Wall is based on the number of galaxies to determine the exact extent and location of the Great Wall along that specific sightline. Here, HS1102+3441 counts as a “hit” for the two looser restrictions, FBQS1010+3003 is a “hit” for all three restrictions, and TON580 is only a “hit” for the loosest restriction.

While even the “narrow” Great Wall definition gives nearly a fifty percent hit rate (see Table 4.2), one must examine the null hypothesis and check to see if this is statistically significant from a random population. Therefore, I performed a Monte Carlo simulation in the same manner as discussed in the TPCF section above (§4.1.2). With the random  $\text{Ly}\alpha$  absorbers placed, I performed the same hit/miss check. As Table 4.2 shows, in all six cases (three Great Wall definitions vs the full and grouped nine populations), there are more hits than would be expected in a random population. However, since the Monte Carlo simulations return a gaussian distribution of hits, the error estimates included show that in each case the excess is approximately only  $1\sigma$  above

	Actual: All (11)	Random: All (11)	Actual: 9 grouped LOS	Random: 9 grouped LOS
+/- 300 km/sec from peak	4	3.1 +/- 1.4	4	2.3 +/- 1.3
50% of peak from peak	6	5.7 +/- 1.5	5	4.2 +/- 1.4
20% of peak from peak	8	8.0 +/-1.4	7	6.2 +/-1.3

Table 4.2: The number of “hits” of Ly $\alpha$  absorbers falling within the specified limits of the Great Wall along the QSO sightlines with the furthest extent of the Great Wall limited to 7000 km/sec. The results for all eleven sightlines are shown on the left, while a subset of the nine tightly grouped sightlines are shown on the right. Also shown are the results of a Monte Carlo uniform random population with the same restrictions and measurements. The results are split along the three definitions of the Great Wall range for each sightline. The peak is the maximum number of galaxies found for each sightline within  $0.015 < z < 0.035$ , while the percentages give the extent of the range by again following the number of galaxies and ending when the galaxy number drops below the peak value. The errors shown on the random samples are the  $1\sigma$  values of the gaussian distributed results.

the random expectation. While it is intriguing that numerous Great Wall definitions and the two populations (full and grouped nine) all show similar results, none can be categorized as statistically significant at this time.

#### 4.2.1 Expanding virial radii

To further examine the possibility that these Great Wall Ly $\alpha$  absorbers may be associated with galaxies, I measured the number of virial radii needed by each galaxy that would produce a “hit” to achieve the covering factor indicated by the actual hit/miss measurement (see §4.2). Specifically, using a region of space bounded by the grouped nine sightlines (plus 0.5 degrees additional in each direction), I searched Dr. Penton’s galaxy database for all galaxies with a luminosity of  $0.5 L_{\star}$  or greater. This value ensures galaxy completeness along all nine sightlines past the far redshift boundary of the Great Wall. I then performed another Monte Carlo simulation by choosing nine random sightlines within this region and determined the Great Wall boundaries in the same manner as before (narrow, medium and wide). Hits were determined by stepping along each sightline and finding the nearest galaxy and measuring the distance away in virial radii. If

the distance was under the cutoff, it was a hit, if not, a miss. In this manner, I can determine how many virial radii each  $0.5 L_*$  or greater galaxy would have to store material in high enough densities to produce a column density of  $\text{Log}(N_{HI}) > 12.9$ . As Table 4.3 shows, the galaxies would have to be between six and nine virial radii in size to match the covering factor that the true Great Wall hit/miss measurement shows.

Virial Radii +/- 300 km/s	Avg hits (of nine) $L_* > .5$	Avg hits (of nine) $L_* > .25$	Virial Radii 50% of peak	Avg Hits (of nine) $L_* > .5$	Avg Hits (of nine) $L_* > .25$	Virial Radii 20% of peak	Avg hits (of nine) $L_* > .5$	Avg hits (of nine) $L_* > .25$
1	.1	.2	1	.5	.7	1	.8	1.1
3	.9	1.2	2	1.6	2.1	2	2.4	3.1
5	1.8	2.7	3	3.1	3.6	3	4.3	5.0
7	2.9	*3.9*	4	4.3	5.0	4	5.6	6.3
*9*	*3.9*	5.2	5	5.5	*6.1*	5	6.6	7.3
11	4.7	6.1	*6*	*6.3*	6.9	6	7.3	*7.9*
13	5.5	6.9	7	7.0	7.5	*7*	*7.9*	8.2
15	6.2	7.6	8	7.6	8.0	8	8.2	8.4
17	6.7	8.1	9	7.9	8.2	9	8.4	8.5
19	7.2	8.5	10	8.2	8.5	10	8.5	8.6
Actual hits Table 4.2	4			6			8	

Table 4.3: The number of hits using the same Great Wall extent definitions (see Table 4.2) for nine random sightlines (repeated 1,000 times and averaged) within the same region of space as the grouped nine QSO sightlines. “Hits” are determined by stepping along the sightline and examining each galaxy nearby. If that galaxy is less than the number of virial radii away for that cutoff regime (left column), then it is a “hit”. Thus, the larger the number of virial radii allowed, the higher the covering factor. Starred rows are the virial radii cutoffs that produce the same number of hits as the actual measurement of the nine QSO sightlines (final row, taken from Table 4.2). As before, the restriction of the Great Wall extent does not change the end results much. This table shows that  $0.5 L_*$  (and greater) galaxies would need material at 6-9 virial radii away dense enough to produce a absorption feature of  $\text{Log}(N_{HI}) > 12.9$  to match the results found in the actual measurement. In addition, a cutoff of  $0.25 L_*$  is also shown. While a portion of the space ( $\approx 33\%$ ) examined is not complete to  $0.25 L_*$  (the entire region is complete to  $0.5 L_*$ ), this does not show a significant change in the number of virial radii needed for the same covering factor.

Again, all three definitions used to limit the Great Wall hit region (narrow, medium and wide) show similar results, indicating that these are relatively independent of this definition. To ensure that there is no controversy about galaxies extending significant quantities of mass to this large of radii, I calculated the mass necessary for the entire galaxy to produce a  $\text{Log}(N_{HI}) > 12.9$  absorber at its limb. Using the lowest radii (6 virial radii) and an estimated mass profile from Gnedin et al. (2010), I found that a  $0.5 L_*$  galaxy would need a mass of approximately  $10^{30}$  solar

masses to have an IGM that dense at that range. This is an unreasonable quantity when the mass of a  $1.0 L_{\star}$  galaxy such as the Milky Way is estimated to be of an order of approximately  $10^{12} M_{\odot}$  (McMillan, 2011). Therefore, it is extremely unlikely that these absorbers are the extended limbs of galaxies and, thus, a significant fraction of them must be parts of galaxy filaments or void absorbers.

### 4.3 Ly $\alpha$ absorber and galaxy populations

With the intriguing, but statistically inconclusive, results of the Hit/Miss procedure, I instead turned to an alternative method of measuring the eleven QSO sightlines while averaged together against the galaxy density background.

#### 4.3.1 Ly $\alpha$ absorbers normalized

The probability of one galaxy completely obscuring another during a galactic survey and distorting the resulting population is small. However, the same is not true for the Ly $\alpha$  absorber search in a spectrum. As Figure 3.3 shows, a significant portion of the spectrum can be obscured by non-Ly $\alpha$  absorbers and galactic lines. In addition, each QSO spectrum has a different detection limit for the weakest Ly $\alpha$  absorbers, not only between targets, but along a single spectrum. Therefore, to create a consistent picture of the number of absorbers across a given redshift, these effects must be removed. Figure 4.9 shows total pathlength of the eleven combined sightlines that is available to search for Ly $\alpha$  absorbers that have an equivalent width  $\mathscr{W} > 15 \text{ m}\text{\AA}$ . Note that one QSO sightline (Mrk421) does not span the entire wavelength range and, thus, the total pathlength after its end is correspondingly lower. This correction factor must be applied at every redshift for these obscuring features and detection limits when calculating the number of absorbers per redshift. The same  $\text{Log}(N_{HI}) > 12.9$  cutoff is also applied (see §4.2) for the same reasons previously discussed.

### 4.3.2 Galaxies normalized

Since no galactic survey is ever complete to the dimmest of galaxies, limits must be applied to ensure that low luminosity galaxies that are detected do not distort the population and results. Unsurprisingly, dim galaxies form an increasingly larger fraction of the population as the survey gets closer to Earth, since they become easier to detect. To remove this bias, I established brightness limits based on the  $L_*$  value of each galaxy. If a region is “complete to  $L_*$ ”, it is assumed that all galaxies with a luminosity of  $L > L_*$  have been detected but there is an inconsistent level of detection for galaxies below that luminosity cutoff. Thus, any galactic population I label as “complete” to a luminosity limit has been excised of any galaxies below that limit. While this limits the studies that include faint galaxies to progressively closer and smaller spatial regions as the luminosity limit drops, it removes the ambiguities and caveats that must accompany a study that does not apply these criteria. I apply three general limits in this study,  $0.1L_*$ ,  $0.5L_*$ , and  $1.0L_*$  (hereafter just  $L_*$ ). The  $L_*$  limit was chosen because it very nearly matches the original redshift range of the Ly $\alpha$  absorber search. While each QSO sightline has a different luminosity limit at

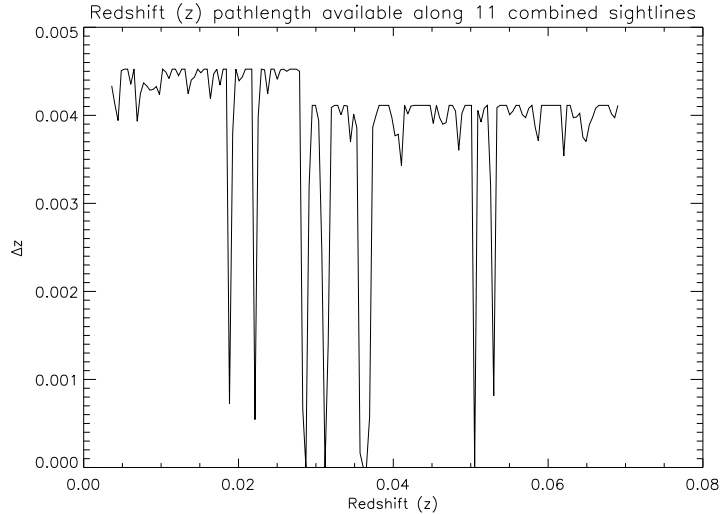


Figure 4.9: The combined pathlength of all eleven QSO targets that is available to search for Ly $\alpha$  absorbers. Dips are due to obscuring galactic lines, non-Ly $\alpha$  absorbers and changes in the  $\mathcal{W}$  detection limit. In addition, one QSO (Mrk421) is located at  $z = 0.03$  and its pathlength ends there.

a given redshift, a  $L_*$  limit covers  $\approx 95\%$  of the absorber sample. The  $0.1L_*$  limit was chosen to match the redshift space of Wakker & Savage (2009), while  $0.5L_*$  is a middle value for investigating incongruities between the other two populations and the completeness level used above.

Since a given galactic luminosity limit shortens the redshift space investigated for a specific QSO sightline, the Ly $\alpha$  absorbers along the same sightline must also be limited to that same redshift. Thus, each luminosity limited galaxy sample has a different number of Ly $\alpha$  absorbers that are acceptable to use. Figure 4.10 shows the corrected pathlengths for Ly $\alpha$  absorbers when the corresponding galactic luminosity redshift limit is applied. With the appropriate limitations and corrections applied, including the  $\text{Log}(N_{HI}) > 12.9$  sensitivity limit discussed in the previous subsection (§4.3.1), the accurate comparison between galaxies and absorbers as a function is shown in Figure 4.11.

### 4.3.3 Ly $\alpha$ absorber and galactic densities discussion

Starting with the sensitivity cutoff of  $\text{Log}(N_{HI}) > 12.9$  does not show strong correlation with background galaxies, although there is a large spike in the CfA Great Wall itself (see Figure 4.11). However, when increasing column density limits are applied, the correlation begins to emerge (see Figure 4.12). While the  $\text{Log}(N_{HI}) > 13.0$  plot does not differ greatly, the  $\text{Log}(N_{HI}) > 13.5$  shows a relatively good match between the Local group ( $z < 0.005$ ), the following void ( $0.005 < z < 0.015$ ), the CfA Great Wall ( $0.015 < z < 0.035$ ) and the next following void ( $0.035 < z < 0.04$ ). While a Kolmogorov-Smirnov test (KS test) on the full range has a very small chance of a similar population (approximately  $10^{-7}$  chance of being the same population), if the KS test is run on just the population below  $z < 0.04$ , it is much more likely (approximately  $10^{-4}$  chance of being the same population). Going to a still higher column density cutoff shows a similar result, but the numbers of absorbers become small enough to create significant statistical noise and no firm conclusions can be drawn. Several previous studies (see §3.1) suggest that while Ly $\alpha$  absorbers with higher column densities correlate to galaxies, those absorbers with lower column densities are more likely to trace the IGM and to be distinct from galaxy populations. These plots show that correlation

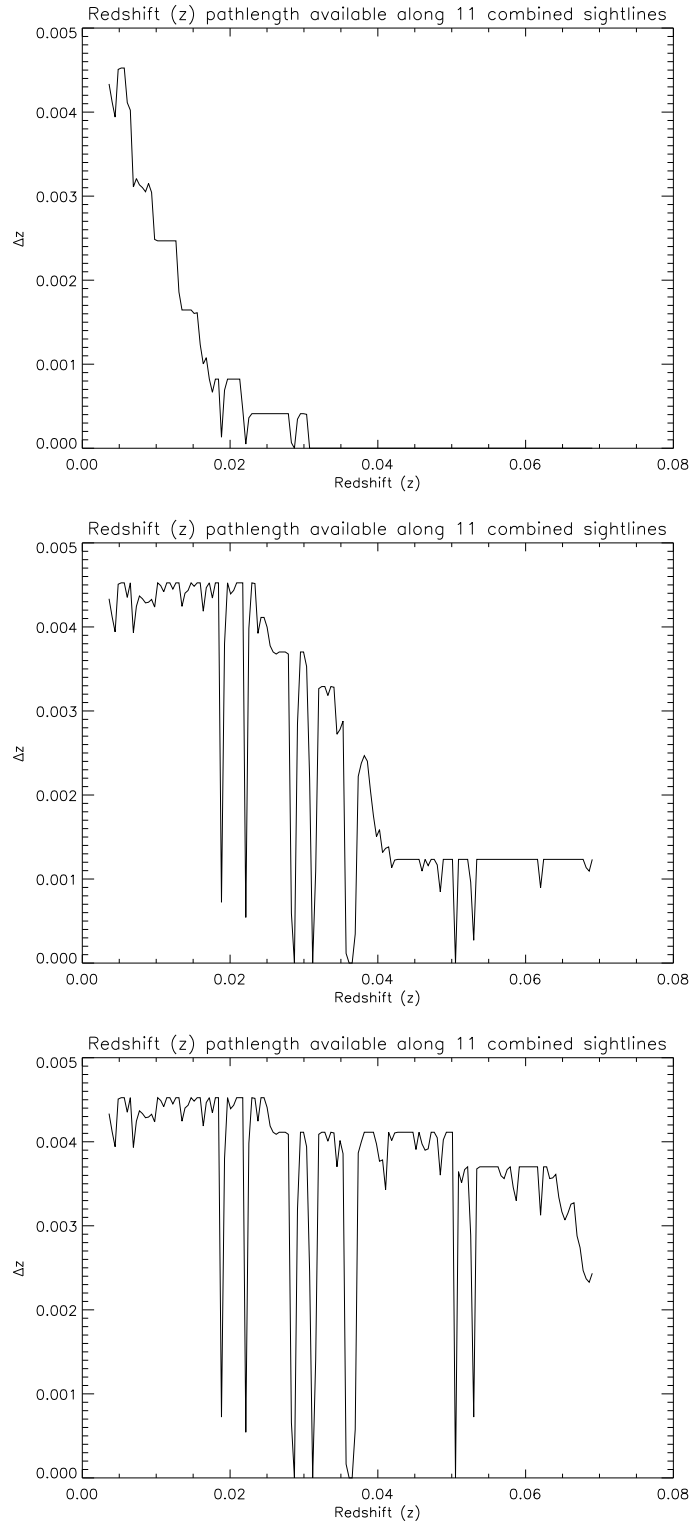


Figure 4.10: The combined pathlength of all eleven QSO sightlines after correcting for absorbers that obscure Ly $\alpha$  and the redshift limits imposed by the galactic survey luminosity limits,  $0.1L_{\star}$  (top),  $0.5L_{\star}$  (middle),  $L_{\star}$  (bottom). While the  $0.1L_{\star}$  pathlength is significantly diminished, the  $L_{\star}$  limit is almost unchanged from an uncorrected sample.

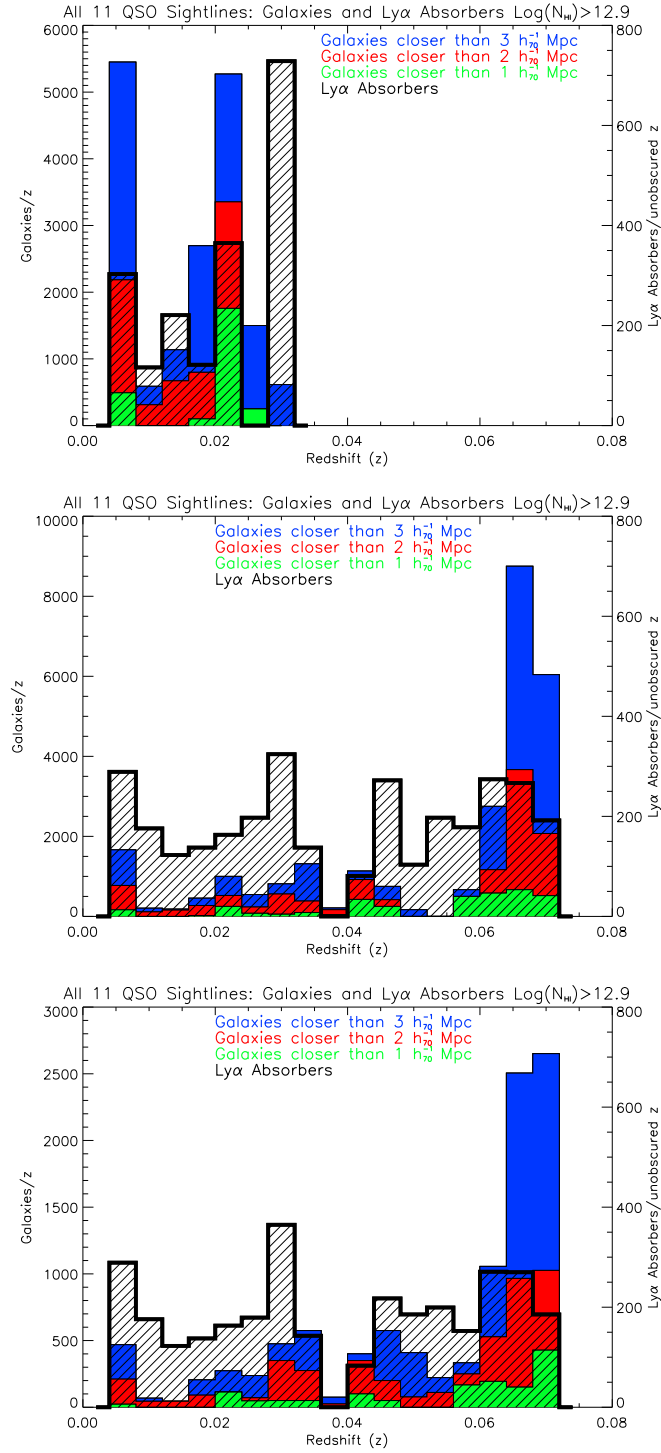


Figure 4.11: The number of Ly $\alpha$  absorbers per redshift (black) and the number of galaxies per redshift as a function of their co-moving distance to the QSO line-of-sight (colors) of the eleven QSO sightlines with redshift limits imposed by the galactic survey luminosity limits,  $0.1L_{\star}$  (top),  $0.5L_{\star}$  (middle),  $L_{\star}$  (bottom). The larger number of galaxies from  $0.015 < z < 0.035$  is the CfA Great Wall, while the lack of galaxies and  $z = 0.04$  and  $0.045 < z < 0.06$  are the following galactic voids. The increasing density of galaxies at  $z > 0.06$  is the beginning of the Sloan Great Wall. The Ly $\alpha$  absorbers have been limited to  $\text{Log}(N_{HI}) > 12.9$  to match sightline sensitivity.

well. Weaker column densities that fall away as the limit is raised are almost entirely in the galactic voids and are the least likely to be associated with a galaxy due to the lack of galaxies in those regions.

The same comparison between Ly $\alpha$  absorbers and nearby galaxies has a similar conclusion when the galaxies are limited to  $0.1L_\star$  and  $0.5L_\star$ . The inclusion of additional low luminosity galaxies changes the galaxy density dramatically and modifies the Ly $\alpha$  absorber population by excluding regions outside the galaxy survey limits. However, as Figure 4.11 shows, the Ly $\alpha$  absorber density and the galactic density still do not match. Again, setting a high column density limit makes a qualitative improvement, but the absorber and galaxy counts still quickly decrease into statistical noise. Even more than the  $L_\star$  limit previously discussed, the  $0.1L_\star$  regime would benefit from the inclusion of additional Ly $\alpha$  absorber studies (e.g. Wakker & Savage, 2009) that cover the  $z < 0.03$  redshift range.

Since the choice of a  $3 h_{70}^{-1}$  Mpc radial cutoff was chosen for a reason that pertains to a different question (see §4.4), I also changed the galaxy distance sample. Since the radial cutoff is not dependent on the survey completeness, the radii chosen does not affect the Ly $\alpha$  absorber sample. The existing figures already show the radial bins limited to one, two and three megaparsecs. Dropping the radial cutoff to either one or two megaparsecs does not change the previous results. When a lesser value is chosen (i.e.  $< 0.5 h_{70}^{-1}$  Mpc), so many galaxies are removed that the statistics are poor. Again, while this approach may be useful when the populations of both galaxies and absorbers are much larger, the relative increase in the number of QSO sightlines and additional galaxies needed will be even more than the previous methods.

The goal of this examination was to determine the association between densities of Ly $\alpha$  absorbers and nearby galaxies. With the inclusion of the CfA Great Wall of galaxies and the surrounding galactic voids, the sample contained large variations in galactic density, with an order of magnitude difference between adjacent redshift bins in the  $0.1L_\star$  sample. While a clear correlation emerges with higher column density cutoffs, when  $\text{Log}(N_{HI}) > 14.0$  the small numbers of Ly $\alpha$  absorbers prevent drawing statistically significant conclusions.

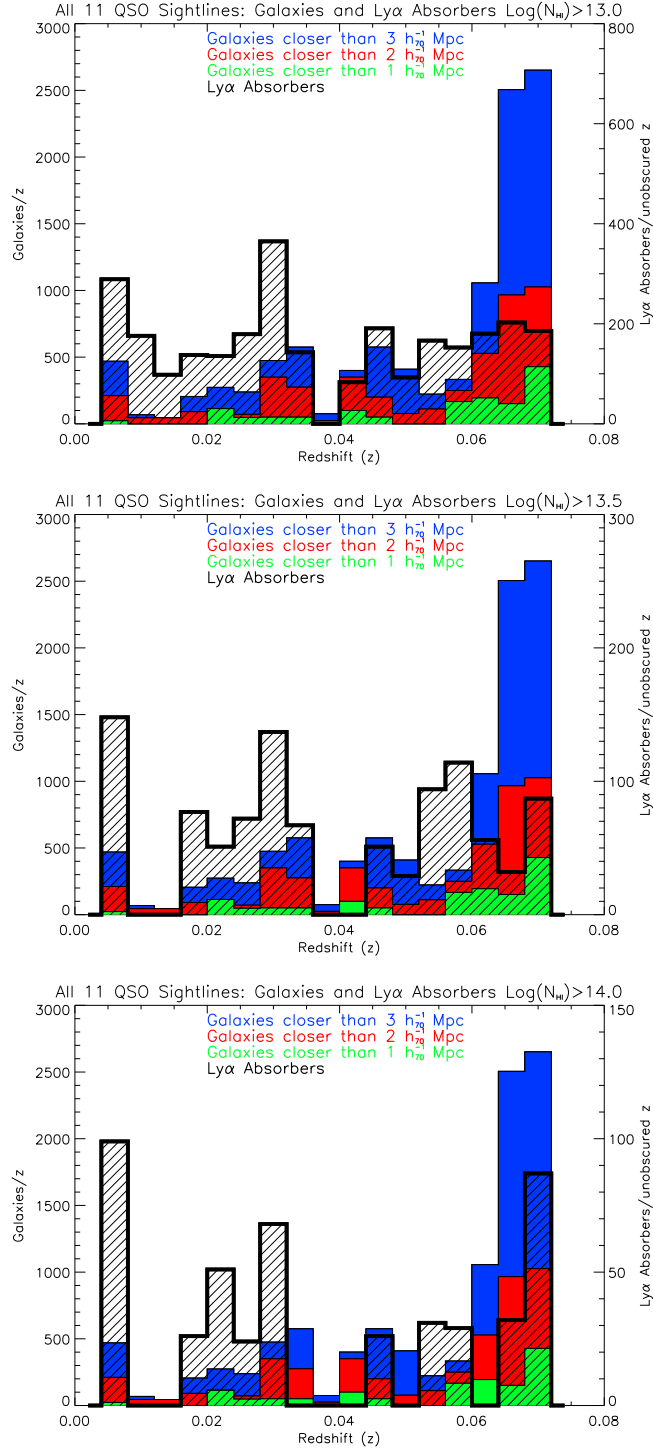


Figure 4.12: The adjusted galaxies and Ly $\alpha$  absorbers per redshift including only the strong absorbers ( $\text{Log}(N_{HI}) > 13.0$ ) on the top,  $\text{Log}(N_{HI}) > 13.5$  in the middle and  $\text{Log}(N_{HI}) > 14.0$  on the bottom. Increasing column density cutoffs show a better correlation with the background galaxy density for  $z < 0.04$ . All the plots are  $1.0 L_*$  limited. Note that each plot has a different y-axis scale for absorbers per redshift.

#### 4.4 Examination of Ly $\alpha$ absorbers and their nearest galactic neighbor

Next, I turned to the examination of individual galaxies associated with each Ly $\alpha$  absorber. This is the same comparison that was done in both Penton et al. (2002) and Wakker & Savage (2009). Using a subset of the Penton et al. (2004) data, Penton et al. (2002) directly examined the galaxy-Ly $\alpha$  absorber relationship. Using similar, but not the same, conditions on galaxy luminosity limits and redshift ranges, they had forty-six Ly $\alpha$  absorbers in regions that were surveyed complete to  $L_\star$ . After correcting for pathlength and sensitivity issues, they claim that 22% of Ly $\alpha$  absorbers lie in voids. Their definition of voids, which I will also use in this study, is  $3 h_{70}^{-1}$  Mpc from the nearest galaxy. Three megaparsecs was chosen because it is the median distance from a random point in the low- $z$  universe to the nearest galaxy (Penton et al., 2002). They also found a significant distinction between the nearest galactic neighbor distance of strong and weak Ly $\alpha$  absorbers. While 80% of their stronger Ly $\alpha$  absorbers ( $\mathcal{W} > 68$  mÅ) have a galaxy within  $1 h_{70}^{-1}$  Mpc, only 45% of the weaker Ly $\alpha$  absorbers fit the same criteria. They also use a TPCF measurement of galaxies to show that the galaxies cluster on the same scale as the strong Ly $\alpha$  absorbers. Together, they use these results to make the claim that low- $z$ , low- $N_{HI}$  Ly $\alpha$  absorbers are not extended halos of galaxies (Penton et al., 2002).

Wakker & Savage (2009), on the other hand, comes to the opposite conclusion. They claim that almost all Ly $\alpha$  absorbers have a galaxy within  $3 h_{70}^{-1}$  Mpc and that the voids present in Penton et al. (2002) come from the lack of sensitivity to galaxies down to a  $0.1L_\star$  limit. Using a smaller redshift range ( $z < 0.017$ ) that is almost complete in galaxy surveys down to this  $0.1L_\star$ , Wakker & Savage (2009) used seventy-six QSO sightlines to find 115 Ly $\alpha$  absorbers. Citing the fact that their Ly $\alpha$  absorber population is consistent with redshift ( $d\mathcal{N}/dz$ ), the same as Penton et al. (2002), they state their conclusions extend beyond the narrow redshift range studied to the wider one employed by other authors (Wakker & Savage, 2009). Notably, their sample places a galaxy within 3 Mpc of 81% of Ly $\alpha$  absorbers when the galactic survey is complete to, and limited by,  $0.1L_\star$ .

Since my data can cover both regimes identified by these two papers, I investigated the claims

made by each. I started by locating the nearest galactic neighbor to each Ly $\alpha$  absorber, if one was present within the  $3 h_{70}^{-1}$  Mpc limit of my galactic list. The distance between a specific galaxy and Ly $\alpha$  absorber is determined by relaxing the redshift measurement of the galaxy by a small amount to be closer to that of the absorber. Since the galaxy may have local motion that is unrelated to the Hubble expansion, differing redshifts between a galaxy and absorber may belie the fact that they are physically close. To account for this, the redshift of a galaxy is allowed to float  $\pm 300$  km/sec to match the Ly $\alpha$  absorber redshift, a “retarded velocity” Penton et al. (2002). While this may err by placing a galaxy closer to an absorber than it actually is, it strengthens any statements about Ly $\alpha$  absorbers in voids. This is explained in more detail in Penton et al. (2002).

Figure 4.13 shows the range of luminosities that these neighbors have and the distance they are from their absorbers. Throughout this section, stronger and weaker Ly $\alpha$  absorbers will be designated, separated on the median of my absorber sample ( $\text{Log}(N_{HI}) = 13.0$ ). As Figure 4.13 shows, there is a large spread of luminosities that form this nearest neighbor population. Thus, using the same rationale as §4.3, the same criteria of pathlength and  $L_{\star}$  luminosity are applied. These limits have the undesired side effect of moving some Ly $\alpha$  absorbers from having a nearest neighbor to the void category, but they are necessary to allow consistent comparisons throughout the sample.

Using the same  $0.1L_{\star}$  (to match Wakker & Savage (2009)),  $0.5L_{\star}$  (used in 4.2.1), and  $L_{\star}$  (to match Penton et al. (2002)) cutoffs, the revised galaxy and absorber samples were re-examined for the nearest galactic neighbor. Since the study also seeks to find the connection between absorbers, galaxies and the IGM, the alternate separation distance scale of the galaxy’s virial radius is also used. The virial radius is estimated from the galaxy’s luminosity by

$$r_{virial} = 250 \text{ kpc} \left( \frac{L}{L_{\star}} \right)^{0.2}, \quad (4.6)$$

taken from Prochaska et al. (2011b).

Figures 4.14 and 4.15 directly address both claims made by Penton et al. (2002) and Wakker & Savage (2009), that large numbers of absorbers are in galactic voids at  $L_{\star}$  regions and most

absorbers have galaxies within 3 Mpc in  $0.1L_*$  regions. When limiting to the  $L_*$  criteria, I find that 71 of 159 (45%) absorbers do not have a galaxy of  $L > L_*$  within  $3 h_{70}^{-1}$  Mpc. While this is higher than the 22% claimed by Penton et al. (2002), they did not remove galaxies that fell below the  $L_*$  limit, only ensuring that the absorbers were in a region that was complete to  $L_*$ . Thus, as Figure 4.13 shows, many galaxies may have nearest neighbors that are at lower luminosities and are removed by my luminosity criteria. The 22% void absorbers claimed by Penton et al. (2002) may instead be viewed as an upper limit; that when fainter galaxies are added into the sample, the number of absorbers without a nearby galaxy can only decrease. In the interest of a more accurate comparison, I relaxed the luminosity criteria imposed on my sample to match those of Penton et al. (2002). That is, absorbers were only kept if they fell within regions that were complete to  $L_*$ , but

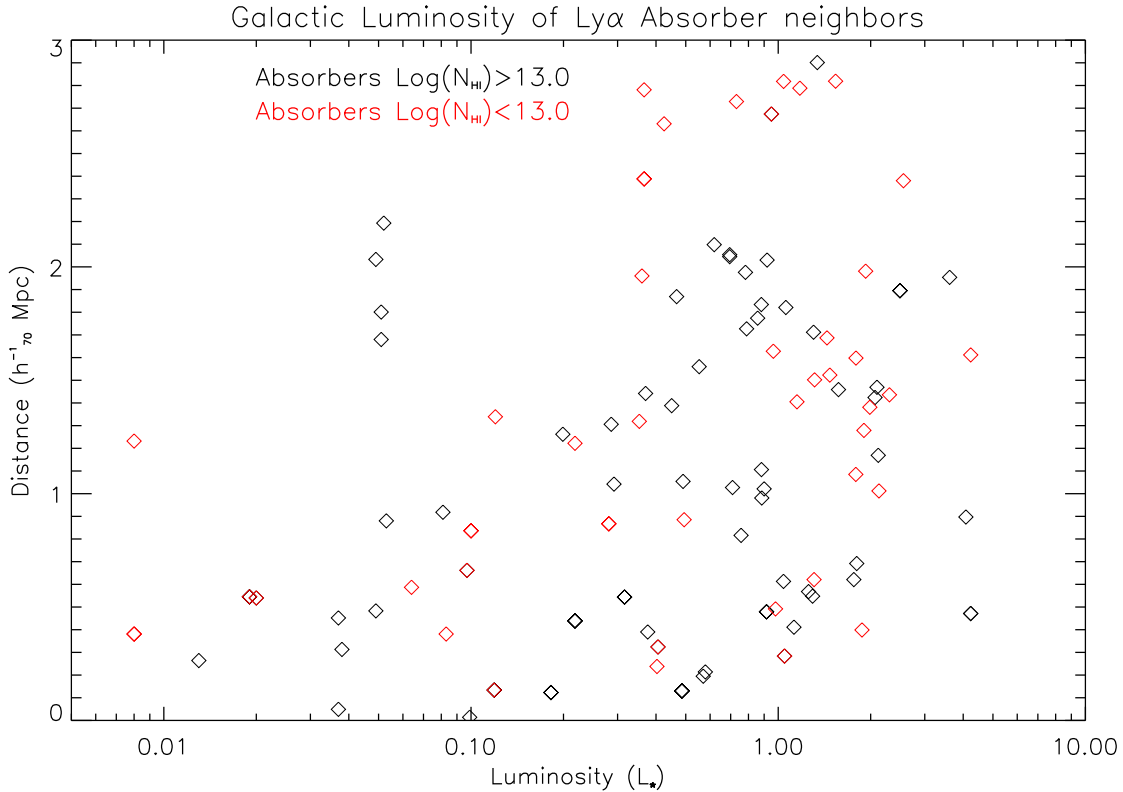


Figure 4.13: The luminosity of nearest neighbor galaxy to each Ly $\alpha$  absorber versus its distance from said absorber. Those absorbers that do not have a galaxy within  $3 h_{70}^{-1}$  Mpc are not shown. The sample is split between strong and weak Ly $\alpha$  absorbers.

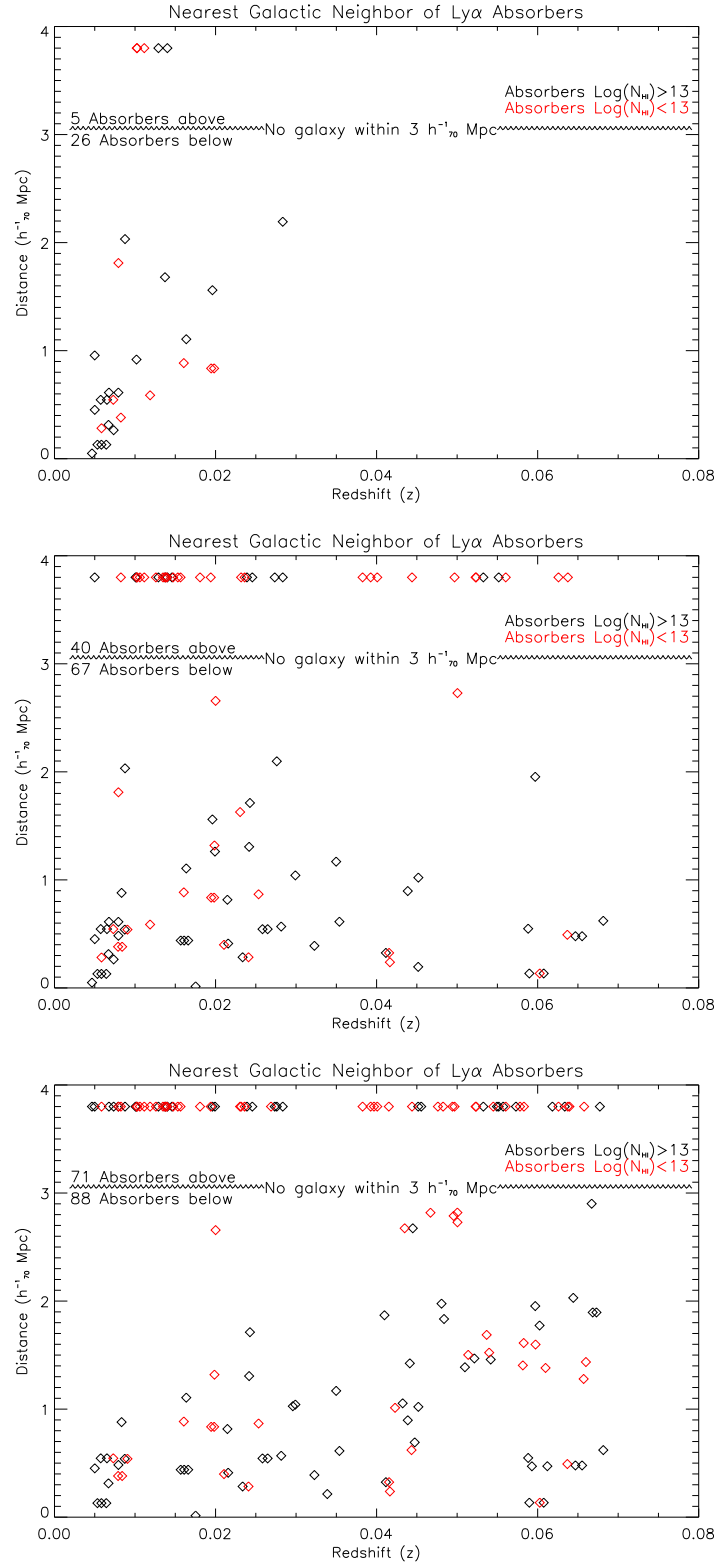


Figure 4.14: The nearest galactic neighbor for each Ly $\alpha$  absorber and this spatial separation of them for the three luminosity cutoff regimes,  $0.1L_{\star}$  (top),  $0.5L_{\star}$  (center), and  $L_{\star}$  (bottom). The data points are split between strong and weak Ly $\alpha$  column densities ( $\text{Log}(N_{HI})=13.0$ ).

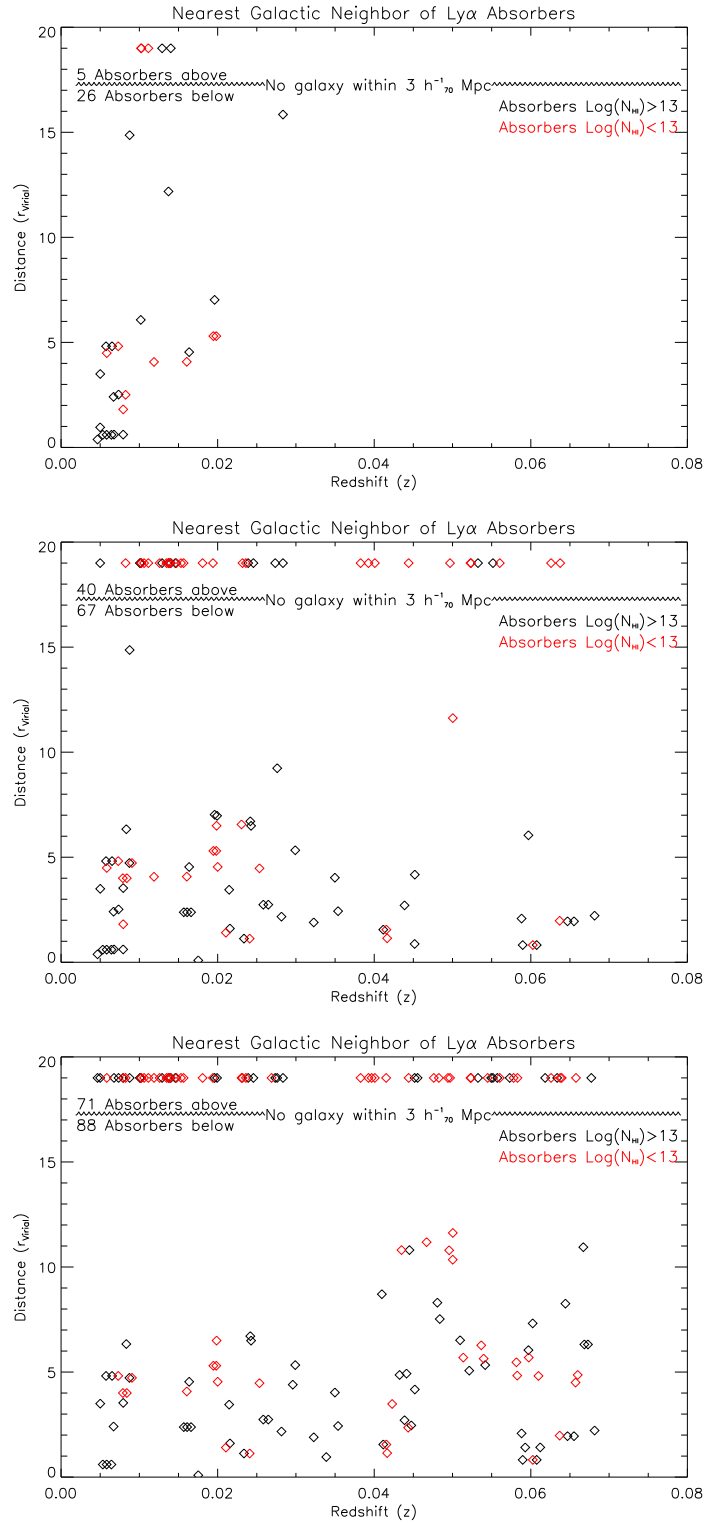


Figure 4.15: The nearest galactic neighbor for each Ly $\alpha$  absorber and this spatial separation based on the number of virial radii of each galaxy for the three luminosity cutoff regimes,  $0.1L_{\star}$  (top),  $0.5L_{\star}$  (center), and  $L_{\star}$  (bottom). The data points are split between strong and weak Ly $\alpha$  column densities ( $\text{Log}(N_{\text{HI}}) = 13.0$ ).

galaxies below  $L_\star$  were not excised from the sample. In this case, I found 35 of 159 (22.0%) were now without a galactic neighbor, matching Penton et al. (2002) well.

Figures 4.14 and 4.15 that are restricted to  $0.1L_\star$  match the study done by Wakker & Savage (2009) with the exception of the “retarded velocity” explained above. Instead of using a fixed value for this correction, Wakker & Savage (2009) list their results for multiple velocities; notably  $\pm 200$  km/sec and  $\pm 400$  km/sec (I used  $\pm 300$  km/sec). Applying the same luminosity criteria over “almost” (the exact quantity is not stated, Wakker & Savage, 2009) the full range of their study, they find 72% ( $\pm 200$  km/sec) and 81% ( $\pm 400$  km/sec) of Ly $\alpha$  absorbers have a galaxy within three megaparsecs when the  $0.1L_\star$  limit is applied. Here, I find 26/31 (84%,  $\pm 300$  km/sec) of absorbers in the same situation for the  $0.1L_\star$  sample. Again, this study matches previous work well and suggests that three populations (mine, Penton et al., 2002; Wakker & Savage, 2009) are all drawn from the same underlying population.

My final examination turned to the relationship between the nearest galactic neighbor and the column density of the Ly $\alpha$  absorber. Figures 4.16 and 4.17 show the scatter plot of this data, again split by distance and virial radius of the specific galaxy over the three galactic luminosity cutoffs. I expected to find an inverse correlation between column density and distance from the nearest galaxy. While the upper right corners of each plot are less populated, the measured correlation is weak or non-existent. Table 4.4 shows the Pearson correlation coefficient for numerous subsets of the data. For those absorbers that have nearest neighbors, there is not a strong correlation between distance and column density for any subset selected. For those Ly $\alpha$  absorbers that do not have a galactic neighbor (i.e. no galaxy within three megaparsecs, voids), I used an alternate method. I binned the number of void absorbers into  $\Delta \text{Log}(N_{HI}) = 0.2$  and correlated the number of absorbers in each bin with the column density strength of that bin.  $0.5L_\star$  and  $L_\star$  cutoffs both show a tight inverse correlation for the number of void absorbers versus the absorber column density for the stronger column density half of the sample, -0.883 and -0.870 respectively. While the  $0.1L_\star$  sample does not contain enough points to make this calculation, the trend from the rest of the subset is clear. The higher in column density a Ly $\alpha$  absorber is, the less likely it is to be found in a  $0.5L_\star$

or  $L_*$  galactic void. Once it passes this  $3 h_{70}^{-1}$  Mpc threshold, however, the relationship becomes less clear.

	$0.1L_*$	$0.5L_*$	$L_*$	$0.1L_*$	$0.5L_*$	$L_*$
All absorbers	-0.27 (26)	-0.22 (67)	-0.29 (88)	-0.36 (5)	-0.60 (40)	-0.63 (71)
Weak absorbers	+0.45 (8)	-0.01 (21)	-0.29 (32)	1. (3)	+0.43 (27)	+0.73 (42)
Strong absorbers	-0.47 (18)	-0.26 (46)	-0.24 (56)	0. (2)	-0.88 (13)	-0.87 (29)

Table 4.4: The Pearson correlation coefficient for subsets of the Ly $\alpha$  absorber-galaxy dataset. The absorbers are split into weak and strong column densities by  $\text{Log}(N_{HI})=13.0$  and the population is limited by the galactic criteria  $0.1L_*$ ,  $0.5L_*$  and  $L_*$ . The left half of the table uses Ly $\alpha$  absorbers that had a galaxy within the  $3 h_{70}^{-1}$  Mpc cutoff and correlates between  $N_{HI}$  and nearest neighbor galactic distance. The right half of the table are the opposing void absorbers that had no galaxy within  $3 h_{70}^{-1}$  Mpc. For these, since there is no galactic distance, the correlation is between column density and the number of void absorbers in  $\Delta\text{Log}(N_{HI})=0.2$  bins. The values in parentheses are the number of Ly $\alpha$  absorbers in each subset.

#### 4.4.1 Nearest galactic neighbor discussion

I have compared my Ly $\alpha$  absorber-galaxy dataset to a few key results presented by Penton et al. (2002) and Wakker & Savage (2009). For both, I found that their statistical conclusions are substantiated by my data when the proper criteria are applied. While Wakker & Savage (2009) make the claim that Ly $\alpha$  absorbers are associated with  $L > 0.1L_*$  galaxies, I find 19% (5 of 26) of absorbers in  $0.1L_*$  complete regions to be located in galactic voids without a neighbor within at least  $3 h_{70}^{-1}$  Mpc. In addition, the median distance in this same  $0.1L_*$  regime between an absorber and the nearest galaxy is  $\sim 5r_{virial}$ . At that range, it is more likely that the Ly $\alpha$  absorber-galaxy connection is a cross-correlation to the underlying large scale density fluctuations within the IGM.

Several studies (e.g. Chen et al., 2001; Bowen et al., 2002; Wakker & Savage, 2009; Prochaska et al., 2011b) examine the absorber-galaxy connection from the other direction. Locating galaxies that are close to QSO sightlines, they identify associated Ly $\alpha$  absorbers. When a galaxy is within a few hundred kiloparsecs, the detection rate of a corresponding Ly $\alpha$  absorber is nearly 100%. Therefore, there must be at least two distinct populations of Ly $\alpha$  absorbers, those closely associated with galaxies and those with no clear association. However, since the division between these two

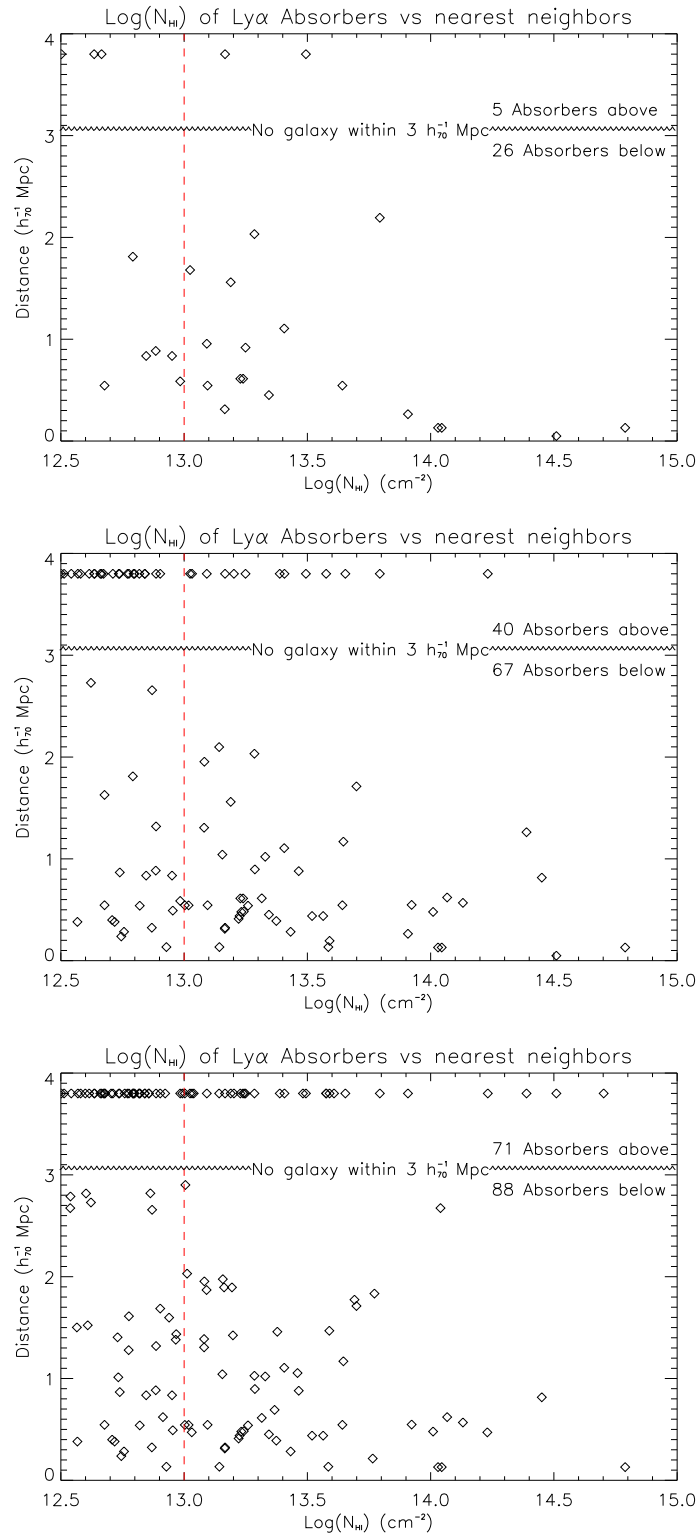


Figure 4.16: The column density ( $N_{HI}$ ) and nearest neighbor galaxy distance, if the absorber has one, of each Ly $\alpha$  absorber. The luminosity limits are  $0.1L_*$  (top),  $0.5L_*$  (middle) and  $L_*$  (bottom). The median column density ( $\text{Log}(N_{HI})=13.0$ ) that divides strong and weak absorbers is marked with a dashed vertical line.

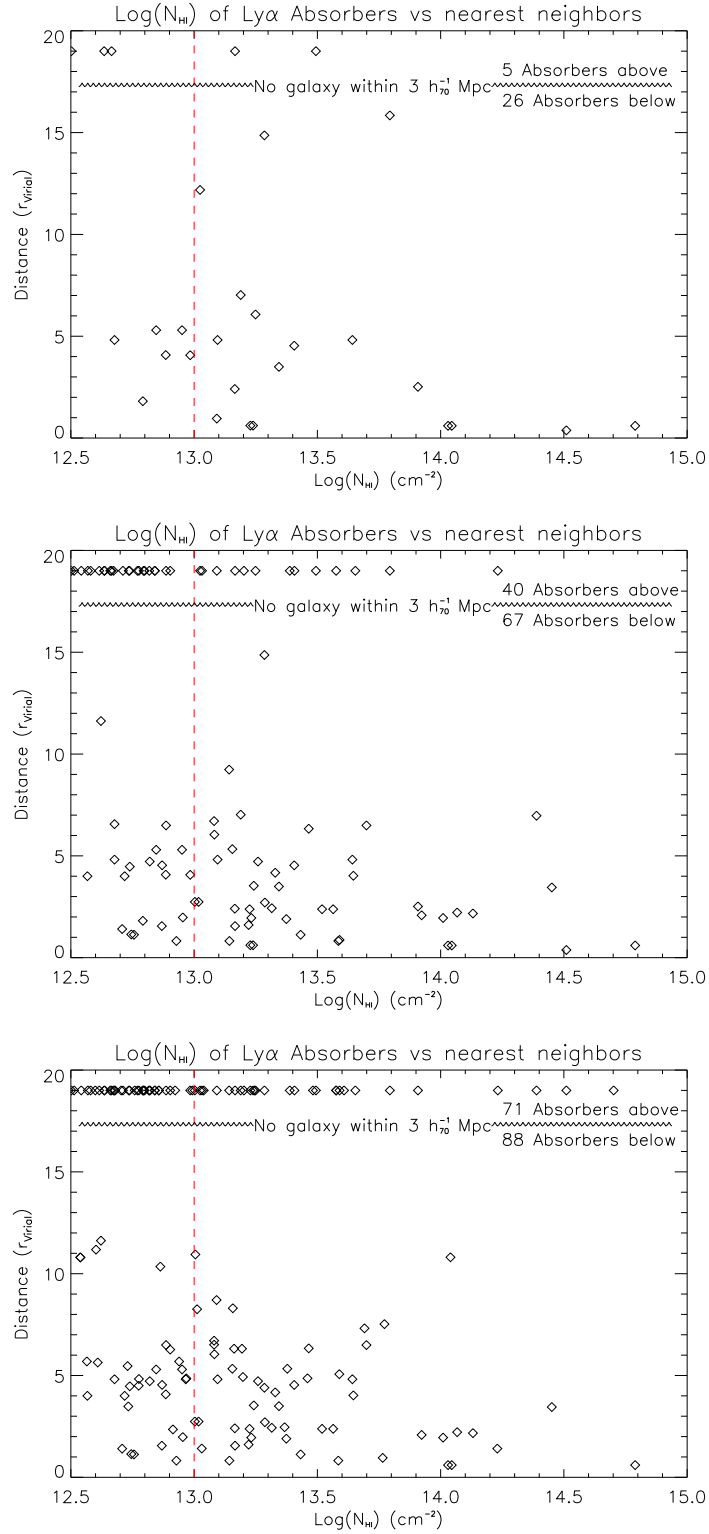


Figure 4.17: The column density ( $N_{HI}$ ) and nearest neighbor galaxy, if the absorber has one, distance in units of the individual galaxy's virial radius. The luminosity limits are  $0.1L_*$  (top),  $0.5L_*$  (middle) and  $L_*$  (bottom). The median column density (Log( $N_{HI}$ )= 13.0) that divides strong and weak absorbers is marked with a dashed vertical line.

populations is not immediately obvious, there are two more likely categories of absorbers: those that are independent but randomly close to a galaxy and those that are materially associated with a galaxy at a larger distance. These last two are mixed in the current observations and, as of yet, there is no reliable way to separate them.

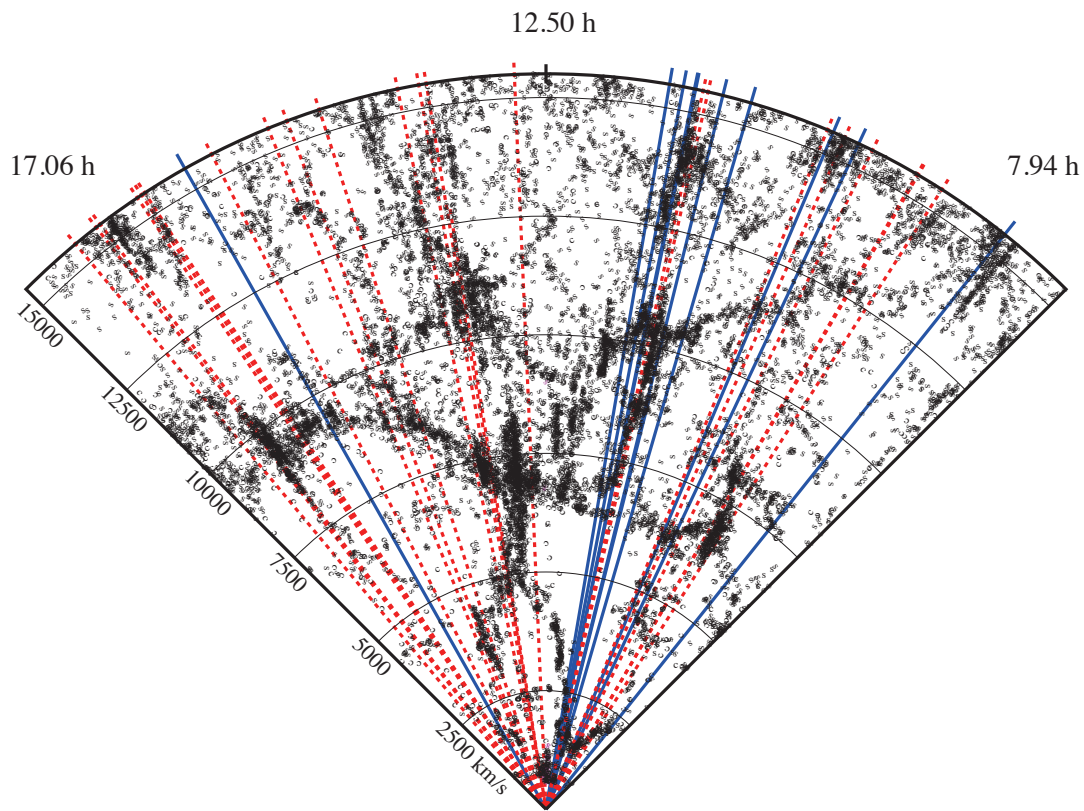
## 4.5 Future work

While this thesis covers several important aspects of the Ly $\alpha$  absorber-galaxy examination, there is always more work to be done. Here I cover the three points that I did not have time to accomplish but feel would add significantly to the results above. While one requires nothing more than existing data and another is likely solvable by an extended literature search compilation, the third pulls in COS spectra I cannot currently access.

With more time to continue work on this data, I would focus on a few key aspects. First, I did not study the reversed approach between galaxies and Ly $\alpha$  absorbers, that is, locating all the galaxies within a certain distance of the QSO sightline and then checking for a matching Ly $\alpha$  absorber. While this would require a more exact detection limit at each galaxy location on the spectra than I have currently calculated, the rest of the data can be immediately pulled out of the existing sample on hand. Mentioned above, several previous authors have investigated this association and the rate of Ly $\alpha$  absorber presence when a galaxy is within a few hundred kiloparsecs of a sightline is nearly 100%. The actual sample numbers, however, are still small and increasing the population will help strengthen the result.

Second, many of the results claimed by Wakker & Savage (2009) may be appropriate for the near universe ( $z < 0.017$ ), but their extension outward can be examined further. Specifically, since the Ly $\alpha$  absorber-galaxy relationship depends on  $\sim 0.1L_*$  galaxies, what is the prevalence of these galaxies further back in time and does that relationship to absorbers remain constant? Prochaska et al. (2011b) has started this examination with 14 QSOs, but further work in this area is required to solidify the results. This may be accomplished by a literature search or a compilation of disparate galaxy surveys along QSO sightlines.

Finally, while the comparison between Ly $\alpha$  absorber densities and galactic densities examined in §4.3 showed promise, it was hampered by small number statistics as one approached the expected column density strength needed to demonstrate a solid relationship between the two parameters. There are twenty-seven other QSO sightlines that have already been observed by COS for other purposes and are currently entering the public domain. All twenty-seven are in the same region of the universe as those discussed in this thesis and Figure 4.18 shows the sightlines relative to the ones studied here. While this is not a trivial amount of work, the amount of effort decreases significantly for each additional target one adds to the sample. This would produce approximately 250% more Ly $\alpha$  absorbers and increase the significance of the results substantially.



$\alpha$  wedge for  $\delta = 32.00 \pm 4.0^\circ$

Figure 4.18: The same map as Figure 3.1 with the eleven QSO sightlines of this thesis (blue lines) and the twenty-seven additional QSO sightlines that could be added to the sample (dashed lines). Adding in all twenty-seven sightlines would increase the number of Ly $\alpha$  absorbers by an estimated 250%. I suggest that this expansion of the sample should be one of the next steps taken in the continued study of the Ly $\alpha$  absorber-galaxy examination. Note: the declination wedge shown does not cover every sightline drawn on the plot.

## Bibliography

- Bahcall, J. N., Jannuzi, B. T., Schneider, D. P., Hartig, G. F., Bohlin, R., & Junkkarinen, V. 1991, *ApJ*, 377, L5
- Bahcall, J. N., et al. 1996, *ApJ*, 457, 19
- Batcheldor, D., Robinson, A., Axon, D., Hines, D. C., Sparks, W., & Tadhunter, C. 2006, *PASP*, 118, 642
- Bianchi, L., Clayton, G. C., Bohlin, R. C., Hutchings, J. B., & Massey, P. 1996, *ApJ*, 471, 203
- Bianchi, L., et al. 2005, *ApJ*, 619, L71
- Blanton, M. R., et al. 2003, *ApJ*, 592, 819
- Bohlin, R. C., Colina, L., & Finley, D. S. 1995, *AJ*, 110, 1316
- Bowen, D. V., Pettini, M., & Blades, J. C. 2002, *ApJ*, 580, 169
- Buat, V., Takeuchi, T. T., & Iglesias-Parámo, J. 2008, in *Astronomical Society of the Pacific Conference Series*, Vol. 381, *Infrared Diagnostics of Galaxy Evolution*, ed. R.-R. Chary, H. I. Teplitz, & K. Sheth, 136
- Burgarella, D., Buat, V., Donas, J., Milliard, B., & Chapelon, S. 2001, *A&A*, 369, 421
- Bush, S. J., Cox, T. J., Hayward, C. C., Thilker, D., Hernquist, L., & Besla, G. 2010, *ApJ*, 713, 780
- Calzetti, D., Kinney, A. L., & Storchi-Bergmann, T. 1994, *ApJ*, 429, 582
- Cen, R., & Ostriker, J. P. 1999, *ApJ*, 514, 1
- Chakrabarti, S., Kimble, R., & Bowyer, S. 1984, *J. Geophys. Res.*, 89, 5660
- Chen, H.-W., Lanzetta, K. M., & Webb, J. K. 2001, *ApJ*, 556, 158
- Chen, H.-W., Lanzetta, K. M., Webb, J. K., & Barcons, X. 1998, *ApJ*, 498, 77
- Chen, H.-W., & Mulchaey, J. S. 2009, *ApJ*, 701, 1219
- Clayton, G. C. 2004, in *Astronomical Society of the Pacific Conference Series*, Vol. 309, *Astrophysics of Dust*, ed. A. N. Witt, G. C. Clayton, & B. T. Draine, 57
- Danforth, C. W. 2012, In Prep.
- Danforth, C. W., Keeney, B. A., Stocke, J. T., Shull, J. M., & Yao, Y. 2010, *ApJ*, 720, 976
- Danforth, C. W., Stocke, J. T., Keeney, B. A., Penton, S. V., Shull, J. M., Yao, Y., & Green, J. C. 2011, *ApJ*, 743, 18
- Davé, R., Hernquist, L., Katz, N., & Weinberg, D. H. 1999, *ApJ*, 511, 521
- Davé, R., Oppenheimer, B. D., Katz, N., Kollmeier, J. A., & Weinberg, D. H. 2010, *MNRAS*, 408, 2051
- dell'Antonio, I. P., Geller, M. J., & Bothun, G. D. 1996, *AJ*, 112, 1780
- Dixon, W. V. et al. 2011, *Cosmic Origins Spectrograph Instrument Handbook Ver. 4*, Tech. rep., Baltimore: STScI
- Elmegreen, B. G. 2002, in *Astronomical Society of the Pacific Conference Series*, Vol. 285, *Modes of Star Formation and the Origin of Field Populations*, ed. E. K. Grebel & W. Brandner, 425

- Fechner, C. 2011, *A&A*, 532, A62
- Feldman, P. D., Sahnou, D. J., Kruk, J. W., Murphy, E. M., & Moos, H. W. 2001, *J. Geophys. Res.*, 106, 8119
- Fitzpatrick, E. L. 2004, in *Astronomical Society of the Pacific Conference Series*, Vol. 309, *Astrophysics of Dust*, ed. A. N. Witt, G. C. Clayton, & B. T. Draine, 33
- Fitzpatrick, E. L., & Massa, D. 1990, *ApJS*, 72, 163
- Froning, C. S., & Green, J. C. 2009, *Astrophys. Space. Sci.*, 320, 181
- Fukugita, M., & Peebles, P. J. E. 2006, *ApJ*, 639, 590
- Geller, M. J. 1997, in *Reviews in Modern Astronomy*, Vol. 10, *Reviews in Modern Astronomy*, ed. R. E. Schielicke, 159–178
- Geller, M. J., & Huchra, J. P. 1989, *Science*, 246, 897
- Ghavamian, P., et al. 2009, *Preliminary Characterization of the Post- Launch Line Spread Function of COS*, Tech. rep.
- Gnedin, O. Y., Brown, W. R., Geller, M. J., & Kenyon, S. J. 2010, *ApJ*, 720, L108
- Gordon, K. D., Calzetti, D., & Witt, A. N. 1997, *ApJ*, 487, 625
- Green, J., Jelinsky, P., & Bowyer, S. 1990, *ApJ*, 359, 499
- Green, J. C. 2001, in *Society of Photo-Optical Instrumentation Engineers (SPIE) Conference Series*, Vol. 4498, *Society of Photo-Optical Instrumentation Engineers (SPIE) Conference Series*, ed. O. H. Siegmund, S. Fineschi, & M. A. Gummin, 229–238
- Green, J. C., et al. 2012, *ApJ*, 744, 60
- Gundersen, K., Wilkinson, E., Green, J. C., & Barstow, M. A. 2001, *ApJ*, 562, 992
- Hjerting, F. 1938, *ApJ*, 88, 508
- Holberg, J. B., & Bergeron, P. 2006, *AJ*, 132, 1221
- Johnson, B. D., et al. 2007, *ApJS*, 173, 392
- Keeney, B. A., Danforth, C. W., & Green, J. C. 2012, in prep.
- Keski-Kuha, R. A., Osantowski, J. F., Leviton, D. B., Saha, T. T., Wright, G. A., Boucarut, R. A., Fleetwood, C. M., & Madison, T. J. 1995, in *Society of Photo-Optical Instrumentation Engineers (SPIE) Conference Series*, Vol. 2543, *Society of Photo-Optical Instrumentation Engineers (SPIE) Conference Series*, ed. M. A. Ealey, 173–179
- Keski-Kuha, R. A. M., Larruquert, J. I., Gum, J. S., & Fleetwood, C. M. 1999, in *Astronomical Society of the Pacific Conference Series*, Vol. 164, *Ultraviolet-Optical Space Astronomy Beyond HST*, ed. J. A. Morse, J. M. Shull, & A. L. Kinney, 406
- Kriss, G. A. 2011, *Improved Medium Resolution Line Spread Functions for COS FUV Spectra*, Tech. rep.
- Lairson, B. M., Grove, D., Smith, R., Lopez, H., Ayers, T., Gantner, B. L., & Beasley, M. N. 2010, in *Society of Photo-Optical Instrumentation Engineers (SPIE) Conference Series*, Vol. 7732, *Society of Photo-Optical Instrumentation Engineers (SPIE) Conference Series*
- Lambrecht, W. R. L., et al. 1994, *Phys. Rev. B*, 50, 10722
- Lanzetta, K. M., Bowen, D. V., Tytler, D., & Webb, J. K. 1995, *ApJ*, 442, 538
- McClure, M. 2009, *ApJ*, 693, L81
- McLin, K. M., Stocke, J. T., Weymann, R. J., Penton, S. V., & Shull, J. M. 2002, *ApJ*, 574, L115
- McMillan, P. J. 2011, *MNRAS*, 414, 2446
- Meiksin, A. A. 2009, *Rev. Mod. Phys.*, 81, 1405
- Morris, S. L., Weymann, R. J., Dressler, A., McCarthy, P. J., Smith, B. A., Terrile, R. J., Giovanelli, R., & Irwin, M. 1993, *ApJ*, 419, 524
- Morris, S. L., Weymann, R. J., Savage, B. D., & Gilliland, R. L. 1991, *ApJ*, 377, L21
- Morrissey, P., et al. 2007, *ApJS*, 173, 682

- Morton, D. C. 2003, *ApJS*, 149, 205
- Noll, S., Pierini, D., Pannella, M., & Savaglio, S. 2007, *A&A*, 472, 455
- Nozawa, T., et al. 2009, in *Astronomical Society of the Pacific Conference Series*, Vol. 414, *Cosmic Dust - Near and Far*, ed. T. Henning, E. Grün, & J. Steinacker, 247
- Penton, S. V., Shull, J. M., & Stocke, J. T. 2000a, *ApJ*, 544, 150
- Penton, S. V., Stocke, J. T., & Shull, J. M. 2000b, *ApJS*, 130, 121
- . 2002, *ApJ*, 565, 720
- . 2004, *ApJS*, 152, 29
- Prochaska, J. X., Weiner, B., Chen, H.-W., Cooksey, K. L., & Mulchaey, J. S. 2011a, *ApJS*, 193, 28
- Prochaska, J. X., Weiner, B., Chen, H.-W., Mulchaey, J., & Cooksey, K. 2011b, *ApJ*, 740, 91
- Rauch, M., Carswell, R. F., Chaffee, F. H., Foltz, C. B., Webb, J. K., Weymann, R. J., Bechtold, J., & Green, R. F. 1992, *ApJ*, 390, 387
- Rosenberg, J. L., Ganguly, R., Giroux, M. L., & Stocke, J. T. 2003, *ApJ*, 591, 677
- Rosenberg, J. L., & Putman, M. E. 2002, in *Astronomical Society of the Pacific Conference Series*, Vol. 276, *Seeing Through the Dust: The Detection of HI and the Exploration of the ISM in Galaxies*, ed. A. R. Taylor, T. L. Landecker, & A. G. Willis, 473
- Sahnou, D. J., et al. 2000, *ApJ*, 538, L7
- Sargent, W. L. W., Young, P. J., Boksenberg, A., & Tytler, D. 1980, *ApJS*, 42, 41
- Sargsyan, L. A., & Weedman, D. W. 2009, *ApJ*, 701, 1398
- Savage, B. D., Lehner, N., & Narayanan, A. 2011, *ApJ*, 743, 180
- Sembach, K. R., Tripp, T. M., Savage, B. D., & Richter, P. 2004, *ApJS*, 155, 351
- Shull, J. M. 2002, in *Astronomical Society of the Pacific Conference Series*, Vol. 254, *Extragalactic Gas at Low Redshift*, ed. J. S. Mulchaey & J. T. Stocke, 51
- Shull, J. M., Smith, B. D., & Danforth, C. W. 2011, *ArXiv e-prints*
- Siegmund, O. 2009, *Private Communications*
- Siegmund, O. H. W., & Gaines, G. A. 1990, *Appl. Opt.*, 29, 4677
- Sitko, M. L., Bernstein, L. S., & Glinski, R. J. 2008, *ApJ*, 680, 1426
- Sommer-Larsen, J. 2006, *ApJ*, 644, L1
- Songaila, A. 2001, *ApJ*, 561, L153
- Stocke, J. T., Penton, S. V., Danforth, C. W., Shull, J. M., Tumlinson, J., & McLin, K. M. 2006, *ApJ*, 641, 217
- Stone, R. P. S. 1996, *ApJS*, 107, 423
- Tepper-García, T. 2006, *MNRAS*, 369, 2025
- Tikhonov, N. A., Galazutdinova, O. A., & Tikhonov, E. N. 2009, *Astronomy Letters*, 35, 599
- Tripp, T. M., Aracil, B., Bowen, D. V., & Jenkins, E. B. 2006, *ApJ*, 643, L77
- Tripp, T. M., Lu, L., & Savage, B. D. 1998, *ApJ*, 508, 200
- Tripp, T. M., Savage, B. D., & Jenkins, E. B. 2000, *ApJ*, 534, L1
- Tripp, T. M., Sembach, K. R., Bowen, D. V., Savage, B. D., Jenkins, E. B., Lehner, N., & Richter, P. 2008, *ApJS*, 177, 39
- Tumlinson, J., Shull, J. M., Giroux, M. L., & Stocke, J. T. 2005, *ApJ*, 620, 95
- Ulmer, A. 1996, *ApJ*, 473, 110
- Wakker, B. P., & Savage, B. D. 2009, *ApJS*, 182, 378
- Wakker, B. P., & van Woerden, H. 1991, *A&A*, 250, 509
- Williams, R. J., Mulchaey, J. S., Kollmeier, J. A., & Cox, T. J. 2010, *ApJ*, 724, L25
- Witt, A. N., & Gordon, K. D. 2000, *ApJ*, 528, 799

## Appendix A

### COS spectra and Ly $\alpha$ absorbers

This appendix contains the spectrum for each of the eleven QSO sightlines and the Ly $\alpha$  absorbers found therein. The table lists these Ly $\alpha$  absorbers by QSO and includes their line-center wavelength, the significance level of the detection, and the equivalent width, doppler parameter and column density of the voigt profile fit to the feature. There are a total of 167 Ly $\alpha$  absorbers within the redshift search range of  $0.0035 < z < 0.07$  (1220-1300 Å for Ly $\alpha$  absorbers). Only Mrk421 is within this redshift range itself and absorbers that may be intrinsic to the QSO have been excluded. Errors listed are the  $1\sigma$  standard deviation of the fit of the individual parameter. Each is calculated by reducing the covariance matrix of the full population of fit parameters that are allowed to float during the fitting process.

PG0832+251 has a Ly $\alpha$  absorber that is treated separately from the rest of the sample ( $\lambda = 1236.9$  Å). As previously stated, it has been excluded from some statistical conclusions that require an equivalent width, doppler parameter or column density. This is because it is poorly constrained by the fitting techniques applied. However, it has been included in samples comparing the nearest neighbor galaxies since this only requires an accurate redshift. The feature used in this manner is marked in Figure A.4 and listed in Table A.1 and is confirmed at that wavelength by multiple higher Lyman lines and metal species. While it appears to be the product of at least two saturated absorbers, a second absorber could not be reconciled with the FUSE data at shorter wavelengths and the lack of a corresponding Ly $\beta$  feature. This feature confusion is probably due to the extreme proximity of nearby galaxies and the blending of several component environments.

There is a  $0.1 L_{\star}$  galaxy that may be as close as  $14 h_{70}^{-1}$  kpc (when the retarded velocity is set to 300 km/sec) and another galaxy that is  $0.65 L_{\star}$  and  $53 h_{70}^{-1}$  kpc away.

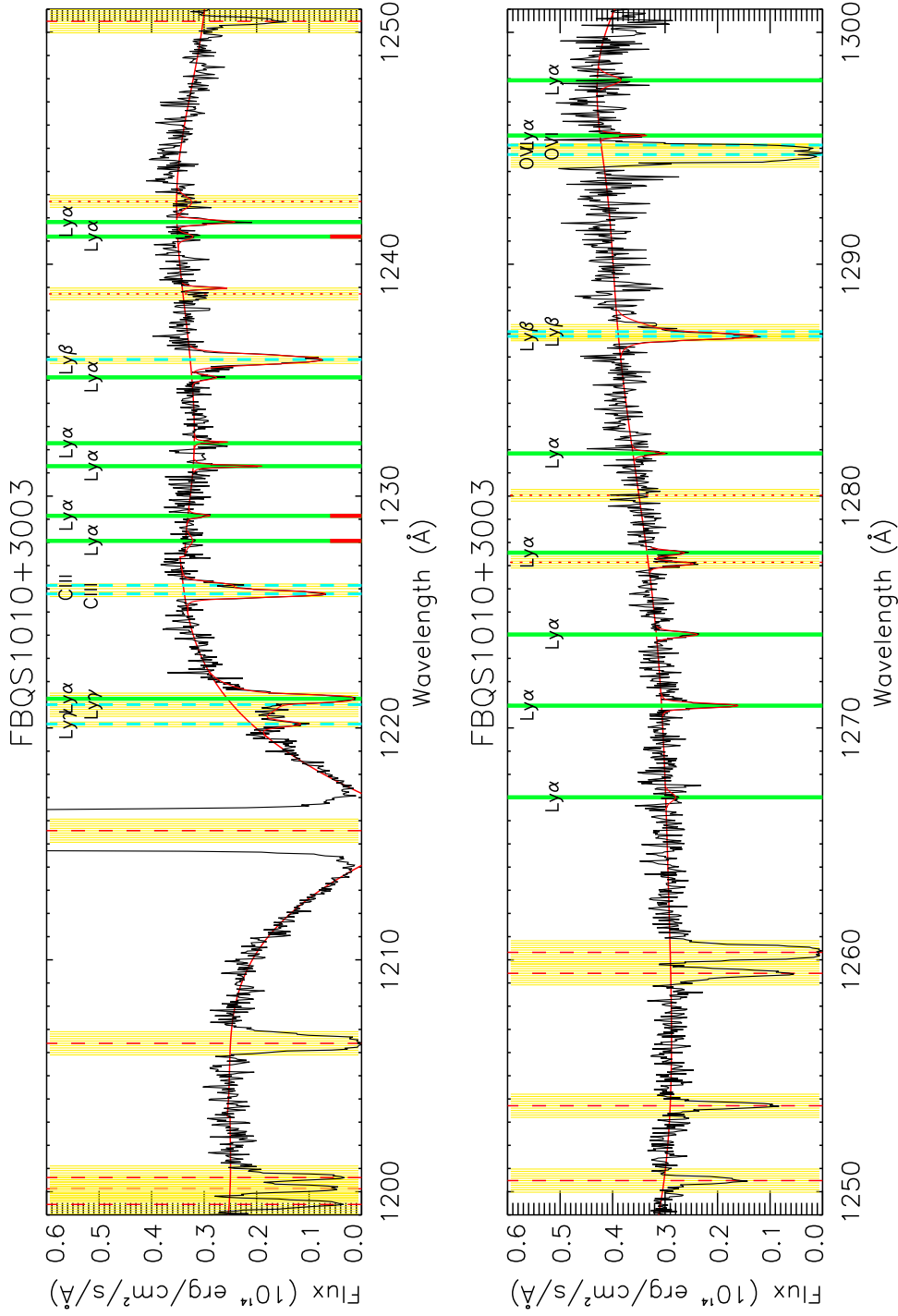


Figure A.1: The  $0.0035 < z < 0.07$  (1220-1300 Å) range of the FBQS1010+3003 spectrum. Solid green vertical lines mark (and are labeled) Ly $\alpha$  absorbers, while dashed blue lines (also labeled) mark other Lyman or metal lines from Ly $\alpha$  absorber systems at higher redshifts. Ly $\alpha$  absorber green lines with a red marker at the bottom are “marginal” ( $3\sigma < SL < 4\sigma$ ). Red dashed and dotted vertical lines show the location of common galactic absorption lines, which are not always present. The red continuum fit is augmented by the voigt profile fit of each absorber. Finally, each non-Ly $\alpha$  feature is surrounded by a yellow box that denotes the region in which a Ly $\alpha$  absorber could not be found due to the obscuration.

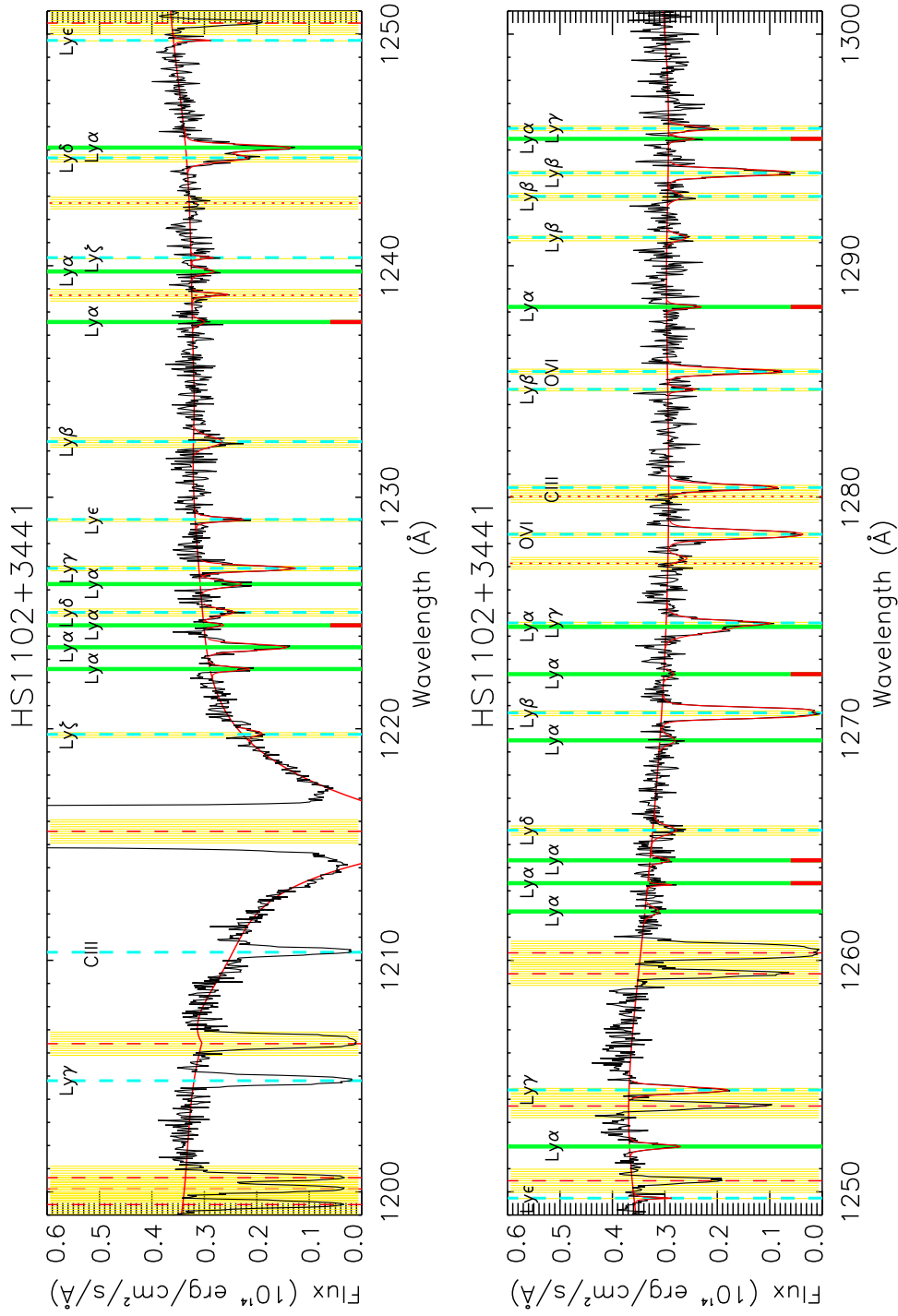


Figure A.2: The continuation of Figure A.1 for the HS1102+3441 spectrum.

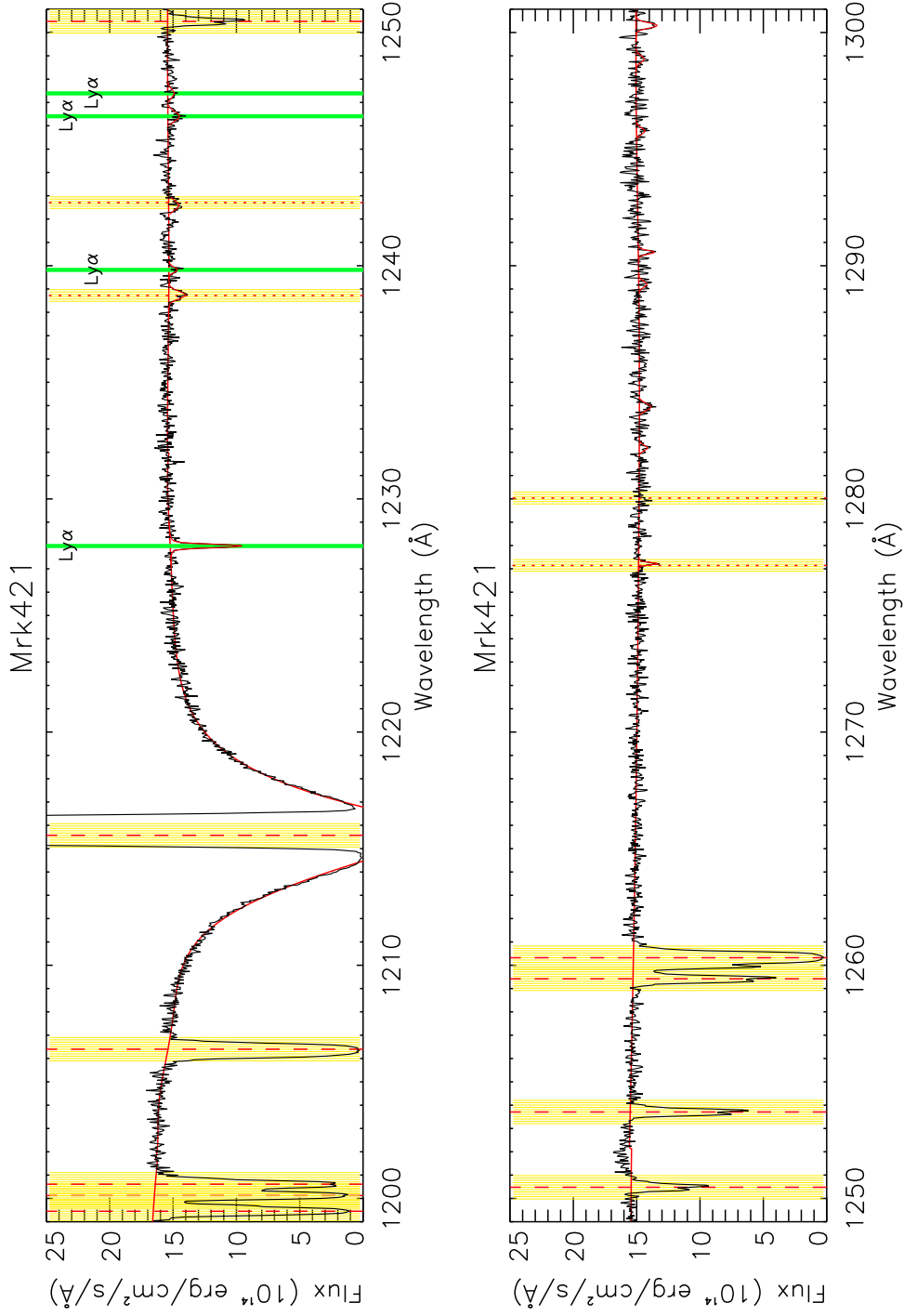


Figure A.3: The continuation of Figure A.1 for the Mrk421 spectrum. Note: the QSO is located at  $z = 0.03$  ( $1252 \text{ \AA}$  for  $\text{Ly}\alpha$ ), limiting the  $\text{Ly}\alpha$  search.



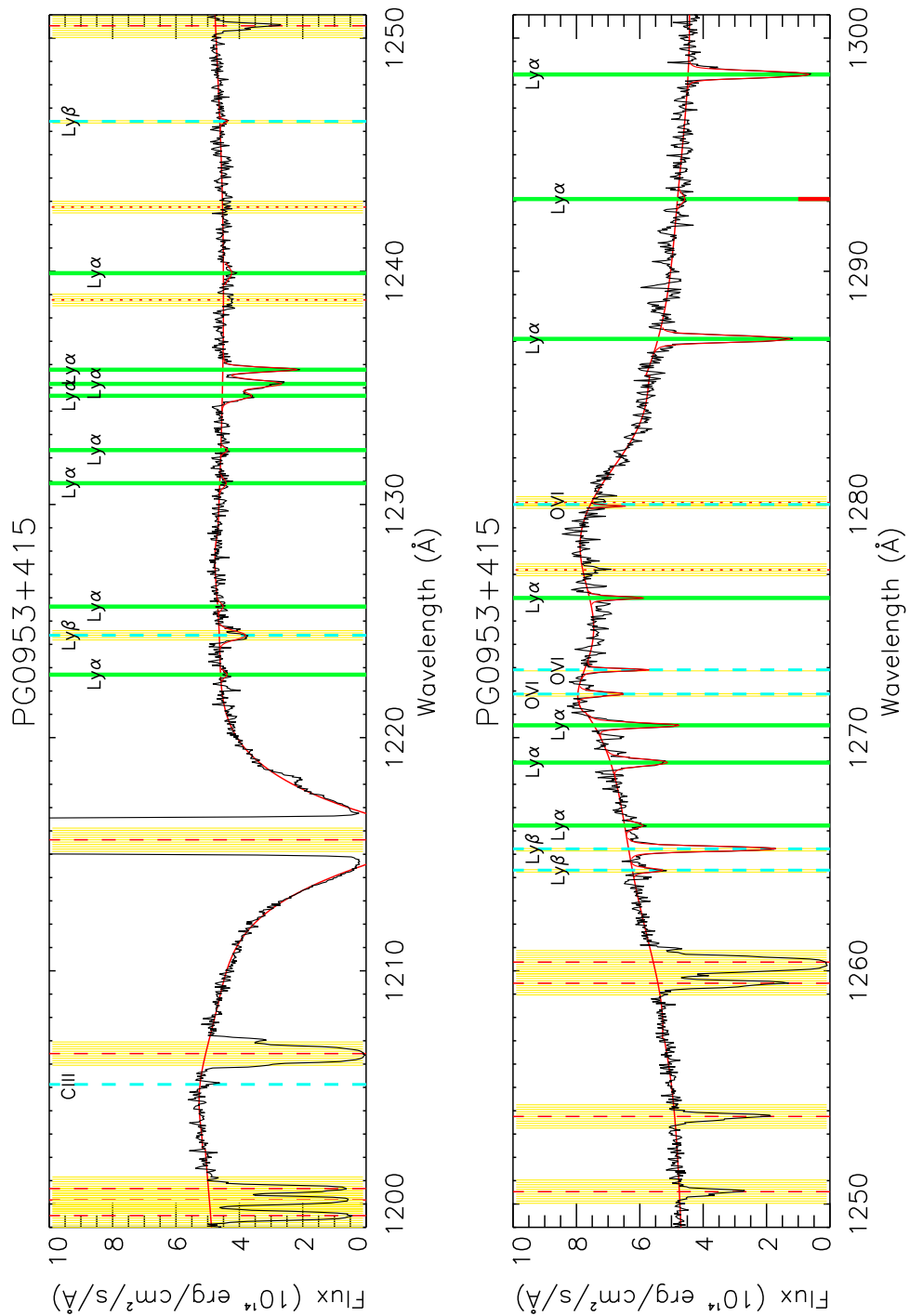


Figure A.5: The continuation of Figure A.1 for the PG0953+415 spectrum.

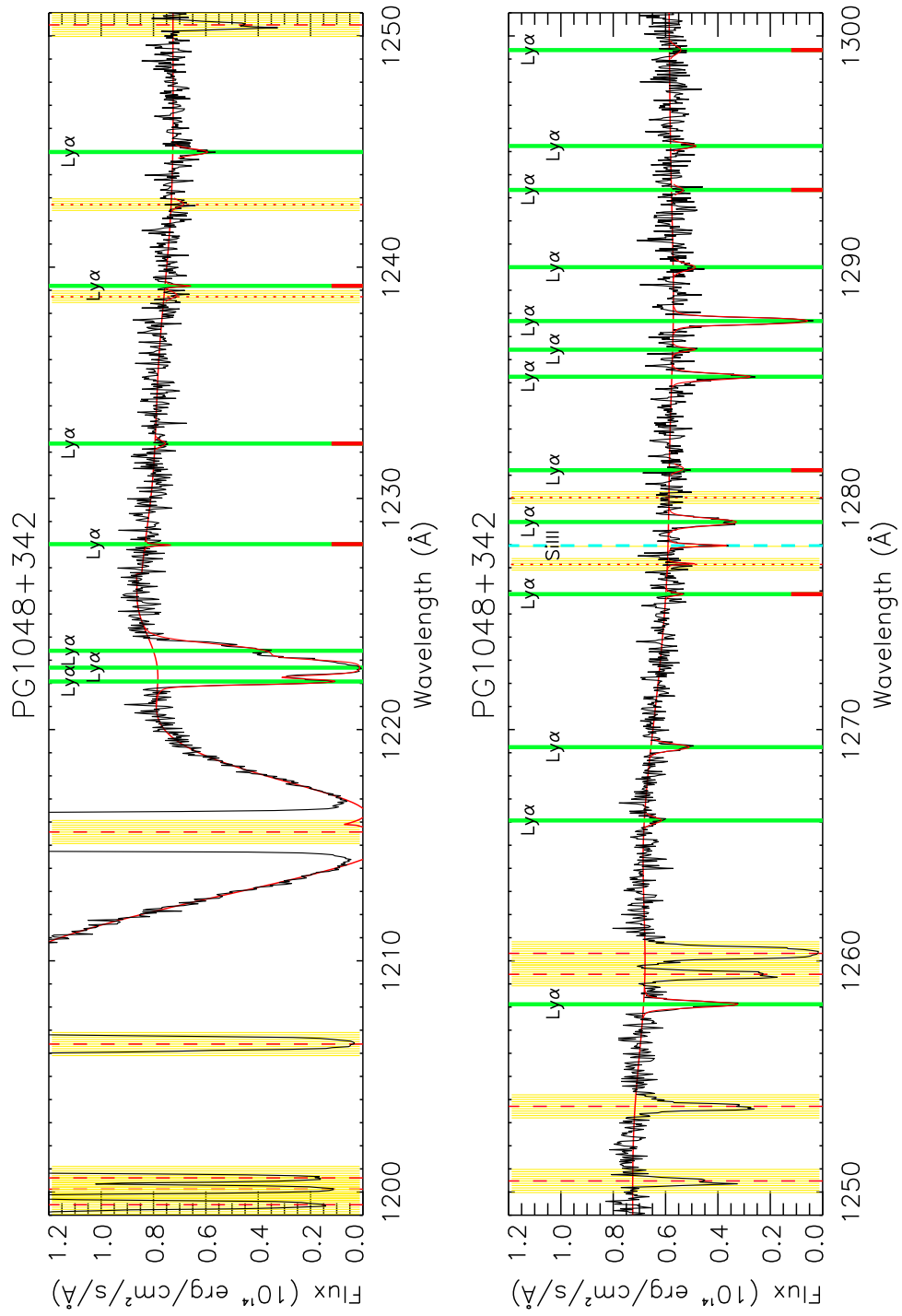


Figure A.6: The continuation of Figure A.1 for the PG1048+342 spectrum.

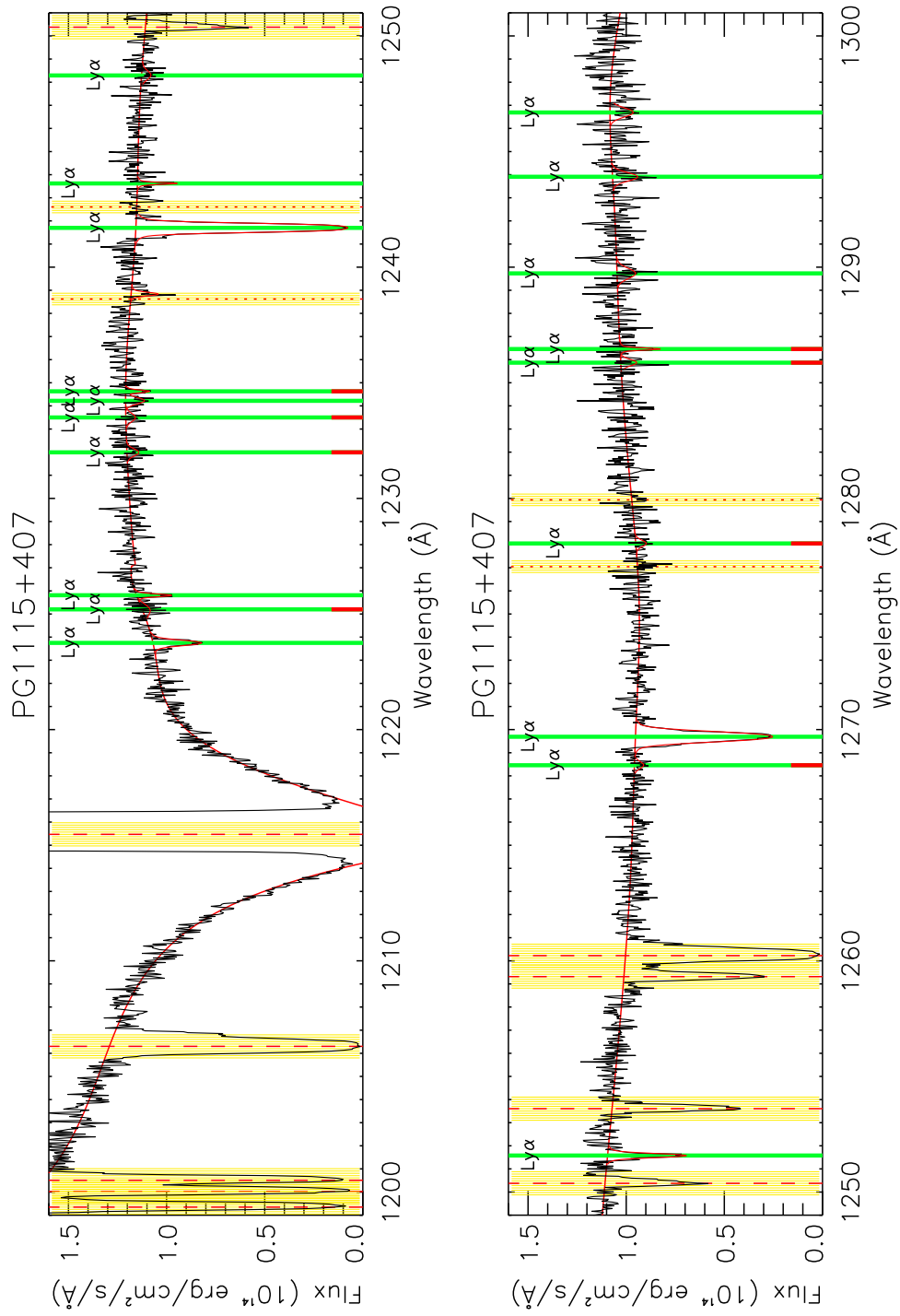


Figure A.7: The continuation of Figure A.1 for the PG1115+407 spectrum.

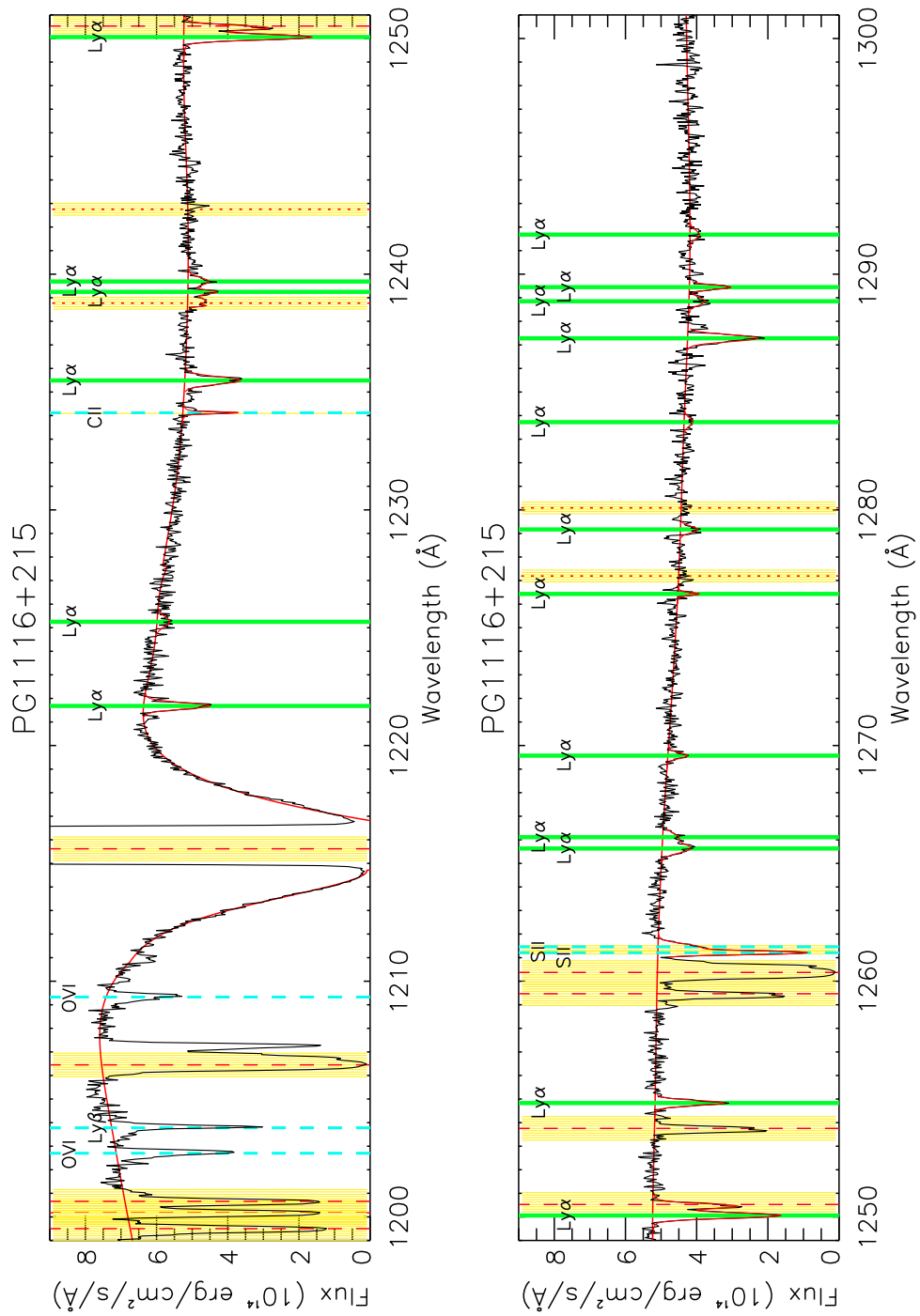


Figure A.8: The continuation of Figure A.1 for the PG1116+215 spectrum.

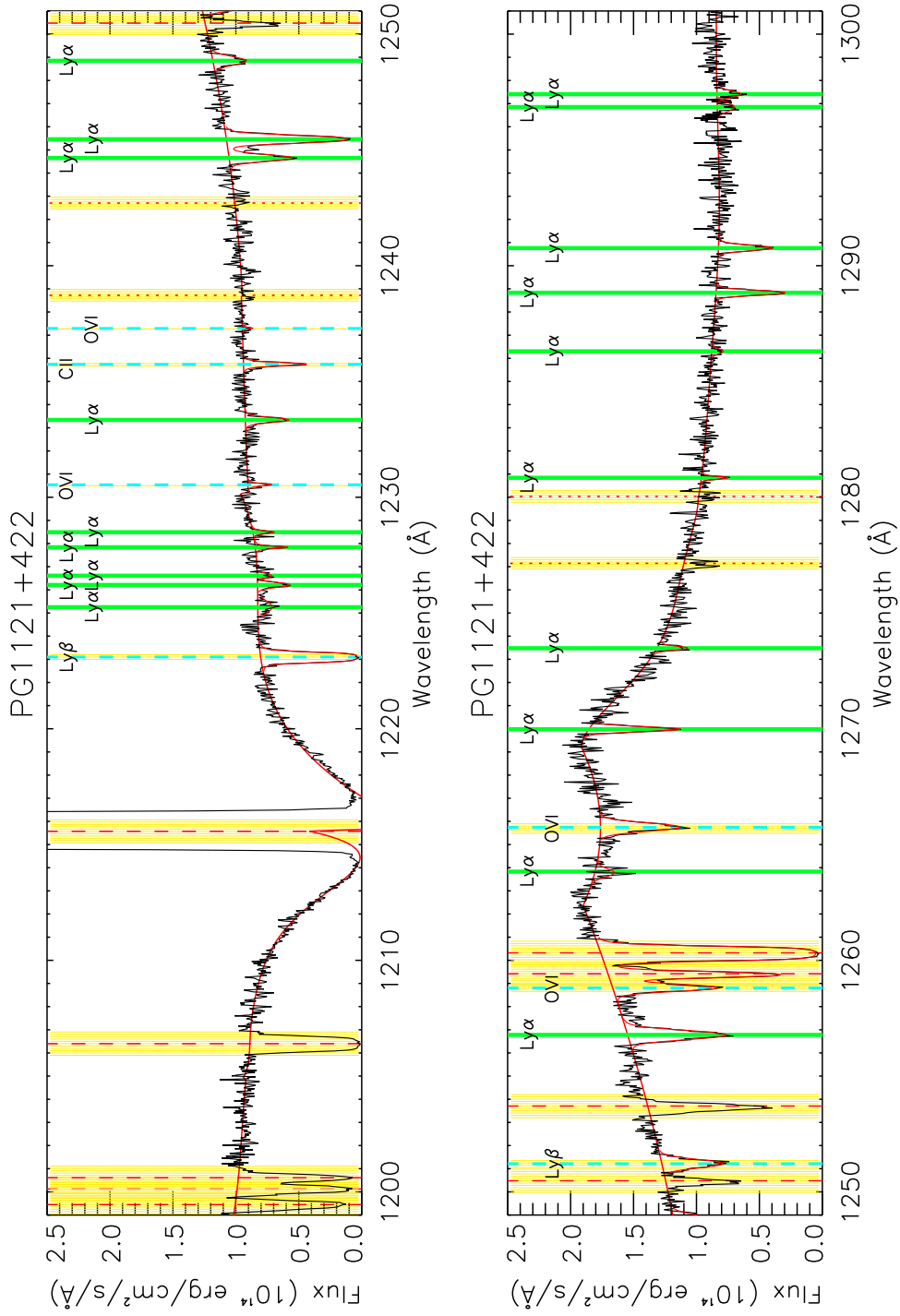


Figure A.9: The continuation of Figure A.1 for the PG1121+422 spectrum.

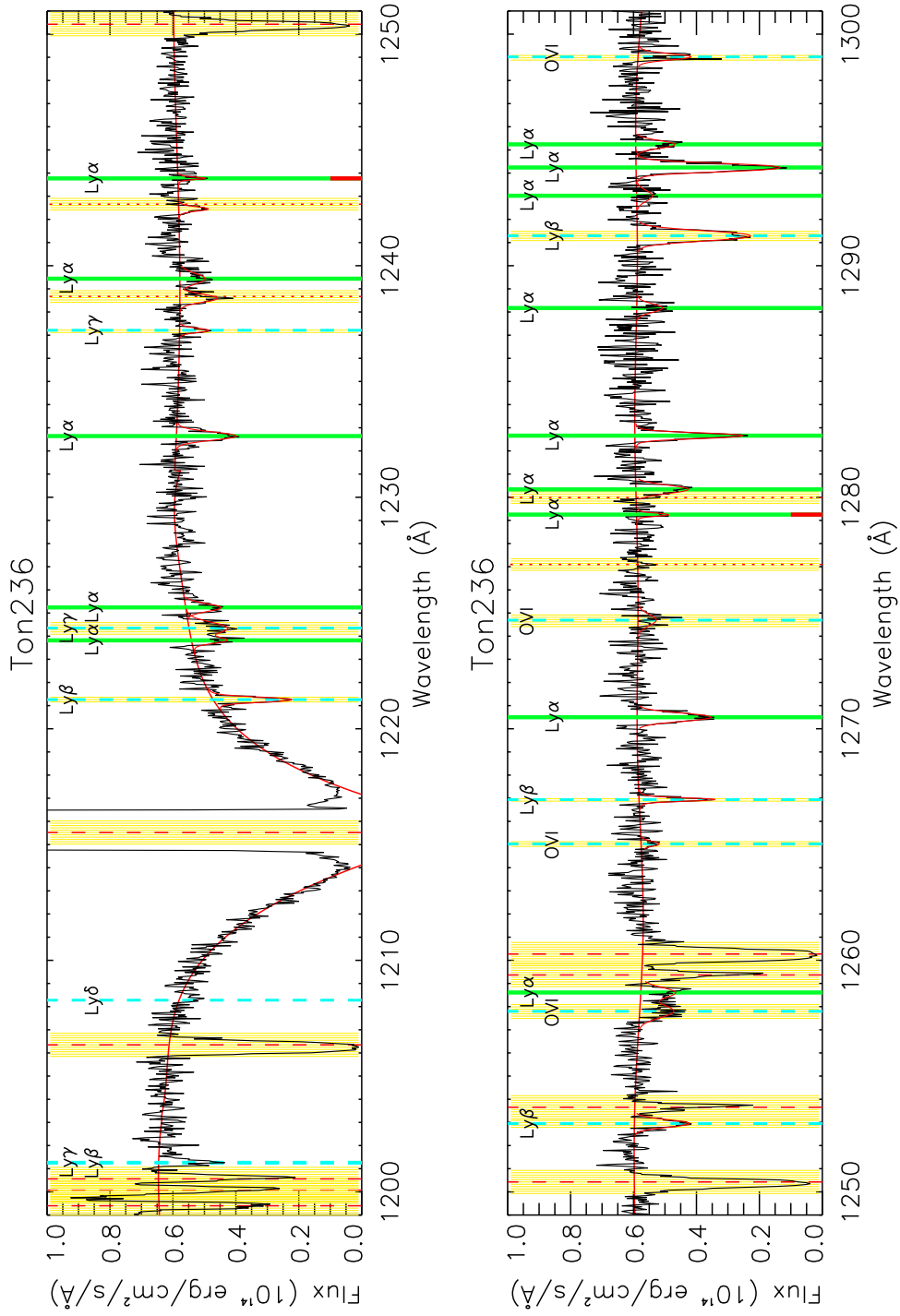


Figure A.10: The continuation of Figure A.1 for the Ton236 spectrum.

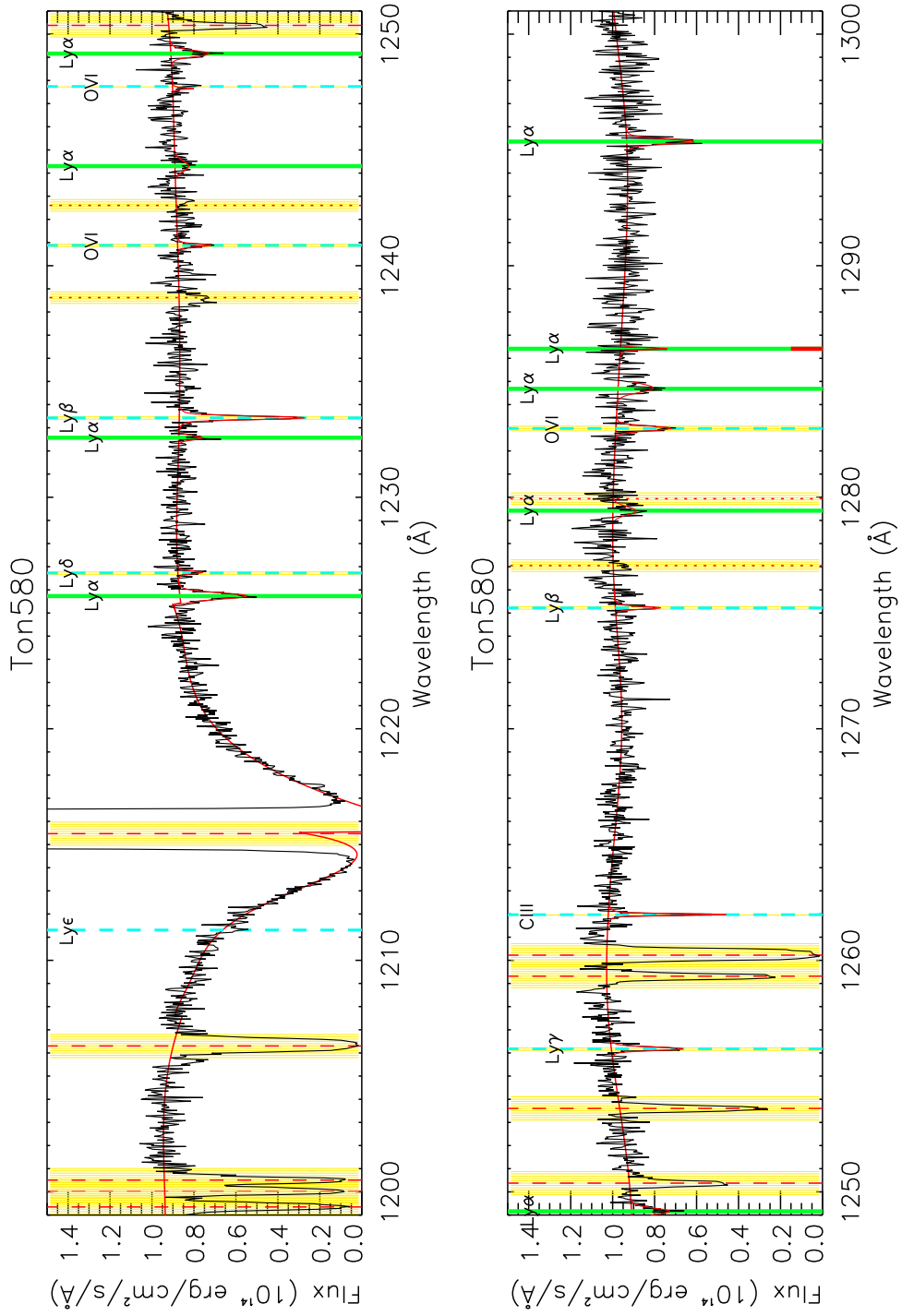


Figure A.11: The continuation of Figure A.1 for the Ton580 spectrum.

Table A.1: A list of all the Ly $\alpha$  absorbers identified in this study. The  $\mathscr{W}$  listed is the measured equivalent width, not the rest frame equivalent width.

Target	Wavelength ( $\text{\AA}$ )	SL ( $\sigma$ )	$\mathscr{W}$ (m $\text{\AA}$ )	$b$ (km/sec)	$\text{Log}(N_{HI})$ $\text{Log}(\text{cm}^{-2})$
FBQS1010+3003	1221.26	56	$373.45 \pm 65.87$	$28.65 \pm 3.44$	$14.510 \pm .171$
FBQS1010+3003	1228.07	3.6	$23.16 \pm 45.50$	$74.03 \pm 63.67$	$12.635 \pm .642$
FBQS1010+3003	1229.15	3.7	$23.55 \pm 17.03$	$18.23 \pm 12.00$	$12.665 \pm .250$
FBQS1010+3003	1231.29	8.7	$54.97 \pm 15.92$	$9.41 \pm 3.35$	$13.166 \pm .080$
FBQS1010+3003	1232.28	8.9	$54.37 \pm 35.54$	$48.68 \pm 15.03$	$13.024 \pm .219$
-----	-----	-----	-----	-----	-----
FBQS1010+3003	1235.12	6.4	$39.11 \pm 29.02$	$30.34 \pm 11.58$	$12.885 \pm .245$
FBQS1010+3003	1241.19	3.5	$26.84 \pm 28.86$	$38.21 \pm 21.13$	$12.708 \pm .363$
FBQS1010+3003	1241.82	10.1	$76.89 \pm 20.12$	$25.89 \pm 4.56$	$13.221 \pm .087$
FBQS1010+3003	1267.01	4.0	$28.71 \pm 44.88$	$56.76 \pm 33.74$	$12.733 \pm .620$
FBQS1010+3003	1270.96	16.4	$122.00 \pm 20.25$	$26.07 \pm 2.86$	$13.482 \pm .058$
-----	-----	-----	-----	-----	-----
FBQS1010+3003	1274.03	9.34	$69.53 \pm 24.47$	$31.88 \pm 6.43$	$13.157 \pm .117$
FBQS1010+3003	1277.56	7.9	$59.33 \pm 23.38$	$31.38 \pm 7.63$	$13.081 \pm .131$
FBQS1010+3003	1281.84	4.4	$33.05 \pm 24.27$	$19.86 \pm 9.05$	$12.821 \pm .226$
FBQS1010+3003	1295.55	4.5	$35.02 \pm 27.85$	$16.67 \pm 11.47$	$12.857 \pm .234$
FBQS1010+3003	1297.93	4.1	$52.58 \pm 57.84$	$63.97 \pm 30.27$	$13.003 \pm .370$
-----	-----	-----	-----	-----	-----
HS1102+3441	1222.58	8.9	$59.10 \pm 22.67$	$23.25 \pm 6.55$	$13.095 \pm .124$
HS1102+3441	1223.52	26.9	$179.34 \pm 26.51$	$37.57 \pm 3.14$	$13.642 \pm .055$
HS1102+3441	1224.47	3.6	$24.35 \pm 20.53$	$20.12 \pm 12.48$	$12.677 \pm .255$
HS1102+3441	1226.25	13.9	$93.48 \pm 31.48$	$42.88 \pm 7.36$	$13.285 \pm .115$
HS1102+3441	1237.57	3.8	$21.78 \pm 28.54$	$36.23 \pm 24.26$	$12.615 \pm .435$
-----	-----	-----	-----	-----	-----
HS1102+3441	1239.75	6.9	$39.42 \pm 35.14$	$33.38 \pm 12.37$	$12.886 \pm .278$
HS1102+3441	1245.10	33.1	$189.72 \pm 19.79$	$33.24 \pm 2.87$	$13.699 \pm .035$
HS1102+3441	1251.96	9.2	$68.19 \pm 21.11$	$27.77 \pm 5.12$	$13.155 \pm .104$
HS1102+3441	1262.11	4.2	$33.19 \pm 56.26$	$52.55 \pm 23.51$	$12.799 \pm .424$
HS1102+3441	1263.33	3.4	$27.14 \pm 32.04$	$45.13 \pm 24.14$	$12.711 \pm .373$
-----	-----	-----	-----	-----	-----
HS1102+3441	1264.32	3.9	$30.88 \pm 36.99$	$29.80 \pm 13.21$	$12.776 \pm .325$
HS1102+3441	1269.50	6.6	$43.04 \pm 41.49$	$58.78 \pm 21.97$	$12.914 \pm .340$
HS1102+3441	1272.36	3.1	$21.25 \pm 31.77$	$41.21 \pm 31.14$	$12.602 \pm .482$
HS1102+3441	1274.40	38.8	$265.28 \pm 76.53$	$77.39 \pm 6.54$	$13.772 \pm .110$
HS1102+3441	1288.22	3.9	$42.04 \pm 23.61$	$19.06 \pm 8.04$	$12.939 \pm .178$
-----	-----	-----	-----	-----	-----
HS1102+3441	1295.48	3.2	$29.64 \pm 28.56$	$17.07 \pm 12.55$	$12.775 \pm .288$
-----	-----	-----	-----	-----	-----
Mrk421	1227.98	30.2	$76.52 \pm 6.77$	$19.05 \pm 1.35$	$13.249 \pm .029$
Mrk421	1239.82	5.1	$13.11 \pm 14.10$	$35.34 \pm 14.93$	$14.389 \pm .307$
Mrk421	1246.41	11.3	$29.21 \pm 15.09$	$63.67 \pm 13.86$	$12.739 \pm .172$
Mrk421	1247.39	6.2	$15.48 \pm 16.35$	$61.47 \pm 24.98$	$12.459 \pm .344$

Table A.2: A list of all the Ly $\alpha$  absorbers identified in this study (continued).

Target	Wavelength (Å)	SL ( $\sigma$ )	$\mathcal{W}$ (mÅ)	$b$ (km/sec)	Log( $N_{HI}$ ) Log(cm $^{-2}$ )
PG0832+251	1221.67	6.3	53.08 $\pm$ 26.69	13.00 $\pm$ 6.81	13.092 $\pm$ .148
PG0832+251	1224.53	26.5	237.02 $\pm$ 26.59	28.61 $\pm$ 2.49	13.908 $\pm$ .043
PG0832+251	1230.03	4.8	42.99 $\pm$ 42.92	12.14 $\pm$ 6.24	12.984 $\pm$ .277
PG0832+251	1236.9	100	1977.28 $\pm$ 101.0	45.51 $\pm$ 12.12	18.755 $\pm$ .588
PG0832+251	1244.00	13.2	130.68 $\pm$ 43.62	58.38 $\pm$ 8.88	13.432 $\pm$ .117
-----	-----	-----	-----	-----	-----
PG0832+251	1244.89	3.2	29.08 $\pm$ 26.86	22.91 $\pm$ 13.80	12.756 $\pm$ .278
PG0832+251	1247.00	5.4	49.86 $\pm$ 27.23	27.78 $\pm$ 9.34	13.003 $\pm$ .175
PG0832+251	1247.78	5.6	51.64 $\pm$ 28.61	28.84 $\pm$ 9.37	13.018 $\pm$ .185
PG0832+251	1249.82	38.7	346.35 $\pm$ 20.82	37.24 $\pm$ 1.73	14.131 $\pm$ .025
PG0832+251	1265.41	4.8	57.68 $\pm$ 25.03	20.73 $\pm$ 6.23	13.091 $\pm$ .141
-----	-----	-----	-----	-----	-----
PG0832+251	1268.16	11.6	140.49 $\pm$ 52.09	66.45 $\pm$ 10.24	13.460 $\pm$ .131
PG0832+251	1274.26	3.6	34.40 $\pm$ 74.71	45.69 $\pm$ 28.21	12.817 $\pm$ .471
PG0832+251	1275.67	4.8	46.74 $\pm$ 25.81	18.50 $\pm$ 7.59	12.993 $\pm$ .178
PG0832+251	1276.42	3.9	38.34 $\pm$ 53.44	55.02 $\pm$ 33.91	12.863 $\pm$ .487
PG0832+251	1281.45	8.7	116.58 $\pm$ 62.26	56.23 $\pm$ 12.07	13.378 $\pm$ .186
-----	-----	-----	-----	-----	-----
PG0832+251	1282.39	35.4	510.34 $\pm$ 53.07	37.91 $\pm$ 3.30	14.702 $\pm$ .150
PG0832+251	1283.34	5.3	73.52 $\pm$ 26.86	16.51 $\pm$ 5.10	13.245 $\pm$ .118
PG0832+251	1292.63	3.2	42.95 $\pm$ 34.60	8.12 $\pm$ 7.33	13.039 $\pm$ .186
PG0832+251	1295.82	3.1	41.30 $\pm$ 28.69	11.53 $\pm$ 8.17	12.968 $\pm$ .205
PG0832+251	1298.33	3.7	50.11 $\pm$ 38.71	23.44 $\pm$ 12.08	13.013 $\pm$ .254
-----	-----	-----	-----	-----	-----
PG0953+415	1222.70	4.9	15.49 $\pm$ 15.28	42.91 $\pm$ 19.83	12.462 $\pm$ .316
PG0953+415	1225.62	4.3	13.74 $\pm$ 15.43	46.03 $\pm$ 22.70	12.408 $\pm$ .363
PG0953+415	1230.91	6.4	20.34 $\pm$ 18.41	57.82 $\pm$ 20.58	12.580 $\pm$ .287
PG0953+415	1232.33	4.0	12.82 $\pm$ 12.34	32.26 $\pm$ 15.82	12.380 $\pm$ .290
PG0953+415	1234.66	26	83.94 $\pm$ 15.26	50.75 $\pm$ 5.38	13.225 $\pm$ .059
-----	-----	-----	-----	-----	-----
PG0953+415	1235.17	50	162.80 $\pm$ 11.24	45.43 $\pm$ 2.25	13.564 $\pm$ .023
PG0953+415	1235.78	40	129.51 $\pm$ 7.82	24.37 $\pm$ 1.07	13.519 $\pm$ .021
PG0953+415	1239.92	11.6	39.49 $\pm$ 25.43	89.66 $\pm$ 21.13	12.870 $\pm$ .230
PG0953+415	1266.23	9.0	29.17 $\pm$ 14.98	39.24 $\pm$ 6.90	12.745 $\pm$ .165
PG0953+415	1268.93	28	93.68 $\pm$ 11.12	41.96 $\pm$ 2.15	13.287 $\pm$ .043
-----	-----	-----	-----	-----	-----
PG0953+415	1270.53	30	96.05 $\pm$ 8.27	28.33 $\pm$ 1.26	13.329 $\pm$ .031
PG0953+415	1275.99	12	38.38 $\pm$ 6.35	16.36 $\pm$ 2.09	12.903 $\pm$ .054
PG0953+415	1287.10	42.2	253.44 $\pm$ 9.09	31.62 $\pm$ .75	13.923 $\pm$ .014
PG0953+415	1293.10	3.9	23.16 $\pm$ 22.73	63.15 $\pm$ 23.74	12.637 $\pm$ .346
PG0953+415	1298.44	49.2	287.41 $\pm$ 9.81	30.01 $\pm$ .79	14.067 $\pm$ .015

Table A.3: A list of all the Ly $\alpha$  absorbers identified in this study (continued).

Target	Wavelength ( $\text{\AA}$ )	SL ( $\sigma$ )	$\mathcal{W}$ (m $\text{\AA}$ )	$b$ (km/sec)	$\text{Log}(N_{HI})$ $\text{Log}(\text{cm}^{-2})$
PG1048+342	1222.08	53.5	$264.66 \pm 16.87$	$27.06 \pm 1.52$	$14.045 \pm .026$
PG1048+342	1222.68	151	$767.26 \pm 47.96$	$60.11 \pm 3.16$	$14.789 \pm .043$
PG1048+342	1223.41	96.	$447.50 \pm 70.10$	$100.09 \pm 8.25$	$14.030 \pm .055$
PG1048+342	1228.02	3.3	$16.69 \pm 15.54$	$23.33 \pm 15.77$	$12.502 \pm .230$
PG1048+342	1232.37	3.2	$15.88 \pm 25.04$	$38.22 \pm 28.53$	$12.474 \pm .451$
-----					
PG1048+342	1239.19	3.0	$15.24 \pm 11.05$	$7.76 \pm 9.40$	$12.492 \pm .168$
PG1048+342	1244.98	11.9	$60.60 \pm 22.86$	$39.65 \pm 7.71$	$13.081 \pm .126$
PG1048+342	1258.12	31.6	$178.76 \pm 19.00$	$36.27 \pm 2.23$	$13.646 \pm .039$
PG1048+342	1266.07	5.7	$32.51 \pm 23.82$	$40.73 \pm 14.97$	$12.793 \pm .262$
PG1048+342	1269.24	13.6	$77.83 \pm 23.54$	$41.30 \pm 6.34$	$13.198 \pm .102$
-----					
PG1048+342	1275.86	3.1	$17.79 \pm 24.08$	$15.61 \pm 12.94$	$12.539 \pm .343$
PG1048+342	1278.98	29.4	$168.75 \pm 25.88$	$43.31 \pm 3.93$	$13.589 \pm .054$
PG1048+342	1281.22	3.4	$19.82 \pm 28.57$	$9.60 \pm 9.49$	$12.609 \pm .298$
PG1048+342	1285.26	22.5	$164.94 \pm 26.99$	$34.09 \pm 3.11$	$13.608 \pm .061$
PG1048+342	1286.43	4.1	$30.22 \pm 25.03$	$21.08 \pm 11.85$	$12.776 \pm .263$
-----					
PG1048+342	1287.67	41.8	$306.55 \pm 25.40$	$27.18 \pm 1.90$	$14.230 \pm .060$
PG1048+342	1290.00	7.5	$54.90 \pm 45.42$	$44.76 \pm 16.87$	$13.031 \pm .263$
PG1048+342	1293.34	3.2	$25.22 \pm 35.96$	$40.28 \pm 33.02$	$12.679 \pm .443$
PG1048+342	1295.24	5.5	$43.52 \pm 27.47$	$30.21 \pm 11.41$	$12.935 \pm .202$
PG1048+342	1299.39	3.7	$31.33 \pm 47.28$	$53.00 \pm 32.33$	$12.773 \pm .488$
-----					
PG1115+407	1223.75	13.7	$71.32 \pm 23.59$	$34.68 \pm 6.15$	$13.165 \pm .110$
PG1115+407	1225.20	3.8	$19.81 \pm 41.53$	$72.19 \pm 58.36$	$12.567 \pm .659$
PG1115+407	1225.81	5.0	$26.08 \pm 14.12$	$15.54 \pm 7.43$	$12.718 \pm .166$
PG1115+407	1231.99	3.7	$19.77 \pm 30.28$	$48.62 \pm 31.59$	$12.569 \pm .488$
PG1115+407	1233.50	3.6	$18.69 \pm 34.45$	$58.45 \pm 41.19$	$12.542 \pm .581$
-----					
PG1115+407	1234.22	5.5	$28.85 \pm 24.08$	$44.73 \pm 19.10$	$12.738 \pm .268$
PG1115+407	1234.63	3.2	$16.82 \pm 12.28$	$16.01 \pm 10.59$	$12.513 \pm .219$
PG1115+407	1241.70	76	$406.56 \pm 19.37$	$33.23 \pm 1.38$	$14.451 \pm .050$
PG1115+407	1243.62	5.2	$22.55 \pm 11.57$	$8.84 \pm 6.08$	$12.677 \pm .139$
PG1115+407	1248.29	4.8	$21.30 \pm 39.40$	$64.57 \pm 42.60$	$12.599 \pm .521$
-----					
PG1115+407	1251.58	21.5	$85.64 \pm 16.63$	$23.88 \pm 2.96$	$13.285 \pm .067$
PG1115+407	1268.46	3.7	$18.43 \pm 31.73$	$47.23 \pm 32.43$	$12.538 \pm .525$
PG1115+407	1269.69	74	$371.29 \pm 20.34$	$53.29 \pm 1.76$	$14.040 \pm .022$
PG1115+407	1278.05	3.4	$19.54 \pm 45.05$	$41.95 \pm 31.40$	$12.565 \pm .667$
PG1115+407	1285.87	3.5	$26.65 \pm 32.28$	$41.50 \pm 28.28$	$12.704 \pm .339$

Table A.4: A list of all the Ly $\alpha$  absorbers identified in this study (continued).

Target	Wavelength ( $\text{\AA}$ )	SL ( $\sigma$ )	$\mathscr{W}$ (m $\text{\AA}$ )	$b$ (km/sec)	$\text{Log}(N_{HI})$ $\text{Log}(\text{cm}^{-2})$
PG1115+407	1286.46	3.5	$27.22 \pm 17.65$	$10.62 \pm 7.76$	$12.759 \pm .187$
PG1115+407	1289.73	5.9	$48.63 \pm 49.95$	$68.80 \pm 28.72$	$12.966 \pm .372$
PG1115+407	1293.91	6.3	$53.26 \pm 48.16$	$55.07 \pm 19.11$	$13.012 \pm .334$
PG1115+407	1296.69	6.3	$52.74 \pm 41.61$	$61.01 \pm 23.24$	$13.005 \pm .257$
PG1116+215	1221.68	30.8	$104.75 \pm 11.82$	$40.94 \pm 2.18$	$13.344 \pm .040$
PG1116+215	1225.25	9.7	$33.00 \pm 18.29$	$71.66 \pm 14.99$	$12.792 \pm .184$
PG1116+215	1235.49	38.1	$120.67 \pm 13.45$	$47.36 \pm 2.38$	$13.406 \pm .040$
PG1116+215	1239.25	10.4	$35.41 \pm 4.97$	$24.12 \pm 5.25$	$12.846 \pm .063$
PG1116+215	1239.69	13.6	$46.35 \pm 5.26$	$49.38 \pm 7.86$	$12.951 \pm .048$
PG1116+215	1250.06	52.5	$207.65 \pm 7.15$	$29.17 \pm .80$	$13.794 \pm .012$
PG1116+215	1254.83	35.2	$105.75 \pm 9.00$	$30.21 \pm 1.50$	$13.374 \pm .030$
PG1116+215	1265.63	20.5	$74.65 \pm 3.50$	$57.84 \pm 5.73$	$13.166 \pm .036$
PG1116+215	1266.11	11.4	$41.50 \pm 13.81$	$62.68 \pm 13.36$	$12.869 \pm .079$
PG1116+215	1269.57	9.5	$34.03 \pm 11.76$	$34.30 \pm 5.81$	$12.818 \pm .114$
PG1116+215	1276.43	5.7	$41.16 \pm 8.14$	$14.48 \pm 4.79$	$12.622 \pm .120$
PG1116+215	1279.17	9.7	$36.10 \pm 14.50$	$39.72 \pm 7.56$	$12.841 \pm .133$
PG1116+215	1283.72	4.4	$24.36 \pm 21.44$	$55.31 \pm 19.21$	$12.660 \pm .292$
PG1116+215	1287.28	29.6	$164.37 \pm 15.27$	$39.66 \pm 1.80$	$13.585 \pm .035$
PG1116+215	1288.85	5.5	$44.15 \pm 19.05$	$51.55 \pm 10.42$	$12.928 \pm .143$
PG1116+215	1289.45	8.3	$66.15 \pm 11.05$	$26.40 \pm 2.92$	$13.143 \pm .055$
PG1116+215	1291.68	5.3	$28.84 \pm 20.42$	$57.71 \pm 17.59$	$12.735 \pm .230$
PG1121+422	1225.25	11.1	$90.08 \pm 50.64$	$85.12 \pm 20.43$	$13.242 \pm .194$
PG1121+422	1226.21	10.4	$84.51 \pm 22.57$	$29.63 \pm 4.82$	$13.259 \pm .090$
PG1121+422	1226.61	5.6	$33.80 \pm 20.56$	$28.03 \pm 11.34$	$12.820 \pm .192$
PG1121+422	1227.84	7.8	$47.16 \pm 14.97$	$12.47 \pm 4.05$	$13.032 \pm .095$
PG1121+422	1228.49	5.6	$33.85 \pm 20.49$	$16.77 \pm 7.00$	$12.840 \pm .183$
PG1121+422	1233.34	18.0	$109.29 \pm 22.06$	$31.35 \pm 3.66$	$13.388 \pm .070$
PG1121+422	1244.65	26.5	$158.41 \pm 21.40$	$36.04 \pm 2.67$	$13.576 \pm .050$
PG1121+422	1245.46	58.5	$350.38 \pm 15.29$	$32.91 \pm 1.17$	$14.232 \pm .024$
PG1121+422	1248.85	12.6	$79.39 \pm 27.03$	$47.08 \pm 7.12$	$13.202 \pm .118$
PG1121+422	1256.78	30.2	$243.35 \pm 23.56$	$54.71 \pm 2.24$	$13.765 \pm .039$
PG1121+422	1263.83	9.8	$37.86 \pm 27.34$	$54.53 \pm 14.39$	$12.857 \pm .247$
PG1121+422	1269.98	14.7	$103.00 \pm 14.03$	$28.20 \pm 2.30$	$13.367 \pm .048$
PG1121+422	1273.48	6.1	$41.64 \pm 17.39$	$23.90 \pm 6.75$	$12.923 \pm .134$
PG1121+422	1280.84	6.2	$38.42 \pm 17.85$	$16.54 \pm 5.96$	$12.903 \pm .145$
PG1121+422	1286.30	4.5	$27.94 \pm 36.33$	$31.09 \pm 20.17$	$12.730 \pm .353$

Table A.5: A list of all the Ly $\alpha$  absorbers identified in this study (continued).

Target	Wavelength ( $\text{\AA}$ )	SL ( $\sigma$ )	$\mathscr{W}$ (m $\text{\AA}$ )	$b$ (km/sec)	Log( $N_{HI}$ ) Log(cm $^{-2}$ )
PG1121+422	1288.83	27.4	171.33 $\pm$ 18.70	25.73 $\pm$ 2.21	13.691 $\pm$ .038
PG1121+422	1290.76	16.9	152.32 $\pm$ 22.50	31.10 $\pm$ 3.02	13.576 $\pm$ .052
PG1121+422	1296.85	6.8	73.94 $\pm$ 60.76	56.82 $\pm$ 16.72	13.162 $\pm$ .289
PG1121+422	1297.41	7.1	76.97 $\pm$ 46.89	40.13 $\pm$ 10.17	13.194 $\pm$ .213
Ton236	1223.82	8.2	65.45 $\pm$ 8.71	39.26 $\pm$ 13.03	13.228 $\pm$ .144
Ton236	1225.24	10.9	86.73 $\pm$ 38.39	52.81 $\pm$ 10.32	13.239 $\pm$ .151
Ton236	1232.64	20.0	146.22 $\pm$ 39.06	53.61 $\pm$ 5.82	13.494 $\pm$ .098
Ton236	1239.44	12.3	79.71 $\pm$ 47.47	73.34 $\pm$ 17.04	13.189 $\pm$ .208
Ton236	1243.77	3.6	23.51 $\pm$ 25.63	13.98 $\pm$ 9.17	12.673 $\pm$ .291
-----	-----	-----	-----	-----	-----
Ton236	1258.61	14.4	103.89 $\pm$ 16.60	68.80 $\pm$ 13.66	13.315 $\pm$ .068
Ton236	1270.50	20.9	174.83 $\pm$ 29.15	51.35 $\pm$ 4.18	13.590 $\pm$ .060
Ton236	1279.25	3.6	30.93 $\pm$ 20.38	17.43 $\pm$ 9.13	12.795 $\pm$ .210
Ton236	1280.34	14.2	122.82 $\pm$ 39.14	52.95 $\pm$ 7.64	13.407 $\pm$ .133
Ton236	1282.66	19.9	172.45 $\pm$ 24.83	30.73 $\pm$ 2.83	13.654 $\pm$ .053
-----	-----	-----	-----	-----	-----
Ton236	1288.17	7.1	62.15 $\pm$ 52.95	55.46 $\pm$ 20.70	13.082 $\pm$ .283
Ton236	1293.02	5.6	47.41 $\pm$ 58.87	71.69 $\pm$ 34.06	12.954 $\pm$ .496
Ton236	1294.24	37.9	319.01 $\pm$ 26.07	41.19 $\pm$ 2.22	14.010 $\pm$ .033
Ton236	1295.24	10.1	84.83 $\pm$ 49.83	49.08 $\pm$ 11.70	13.232 $\pm$ .197
Ton580	1225.73	27.4	131.91 $\pm$ 26.35	39.97 $\pm$ 4.10	13.465 $\pm$ .071
Ton580	1232.57	6.25	30.21 $\pm$ 19.43	26.04 $\pm$ 11.25	12.770 $\pm$ .203
Ton580	1244.30	5.92	40.74 $\pm$ 43.64	74.10 $\pm$ 30.27	12.886 $\pm$ .370
Ton580	1249.16	10.63	69.15 $\pm$ 28.14	40.52 $\pm$ 7.73	13.142 $\pm$ .137
Ton580	1279.42	9.47	49.51 $\pm$ 12.01	56.26 $\pm$ 18.10	12.978 $\pm$ .103
-----	-----	-----	-----	-----	-----
Ton580	1284.68	10.87	75.17 $\pm$ 17.57	54.54 $\pm$ 16.86	13.177 $\pm$ .097
Ton580	1286.41	3.6	27.08 $\pm$ 23.70	7.58 $\pm$ 7.51	12.784 $\pm$ .173
Ton580	1295.36	14.55	98.24 $\pm$ 28.68	31.53 $\pm$ 5.49	13.331 $\pm$ .099

## Appendix B

### Acronym list

Table B.1: A list of acronyms used in this thesis.

Acronym	Meaning
$b$	doppler parameter
CALCOS	Calibration software for COS
CfA	Center for Astrophysics
COS	Cosmic Origins Spectrograph
FIRE	Far-ultraviolet Imaging Rocket Experiment
FUSE	Far Ultraviolet Spectroscopic Explorer
FUV	Far-ultraviolet
IGM	Intergalactic Medium
GALEX	Galaxy Evolution Explorer
HST	Hubble Space Telescope
MAST	Multimission Archive at STScI
MCP	Micro-Channel Plate
NUV	Near-ultraviolet
$N_{HI}$	column depth
QSO	Quasi-Stellar Objects
SDSS	Sloan Digital Sky Survey
SL	Significance Level
TPCF	Two-Point Correlation Function
UV	Ultraviolet
$\mathcal{W}$	equivalent width
WHIM	Warm-Hot Intergalactic Medium
$z$	redshift

## Appendix C

### Nearest Galaxy Neighbor List

This appendix contains a tabular list of all Ly $\alpha$  absorbers in this thesis and their nearest galaxy neighbor. Also included are the column density of the absorber and the galaxy luminosity and distance in virial radii of the galaxy.

Table C.1: A list of all Ly $\alpha$  absorbers and their nearest galactic neighbor.

QSO Sightline	Absorber Wavelength ( $\text{\AA}$ )	Column Density ( $\text{Log}(N_{HI})$ )	Galaxy Name	Galaxy Luminosity ( $L_{\star}$ )	Distance (virial radii)
fbqs1010+3003	1221.26	14.51	10066+3024	0.04	0.38
fbqs1010+3003	1228.07	12.63	None	0.00	0.00
fbqs1010+3003	1229.15	12.66	None	0.00	0.00
fbqs1010+3003	1231.29	13.17	SDR8-O1237665369038455025	0.05	13.06
fbqs1010+3003	1232.28	13.02	SDR8-O1237665369038455025	0.05	12.19
fbqs1010+3003	1235.12	12.88	10050+2943	0.49	4.08
fbqs1010+3003	1241.19	12.71	SDR8-O1237665127994949685	1.87	1.41
fbqs1010+3003	1241.82	13.22	10069+3034	1.12	1.61
fbqs1010+3003	1267.01	12.73	SDR8-O1237665097393635493	2.13	3.48
fbqs1010+3003	1270.96	13.48	None	0.00	0.00
fbqs1010+3003	1274.03	13.16	SDR8-O1237665096857026674	0.78	8.30
fbqs1010+3003	1277.56	13.08	SDR8-O1237665097393635603	0.45	6.51
fbqs1010+3003	1281.84	12.82	None	0.00	0.00
fbqs1010+3003	1295.55	12.86	None	0.00	0.00
fbqs1010+3003	1297.93	13.00	None	0.00	0.00
hs1102+3441	1223.52	13.64	11084+3450	0.02	4.82
hs1102+3441	1222.58	13.10	11084+3450	0.02	4.82
hs1102+3441	1224.47	12.68	11084+3450	0.02	4.82
hs1102+3441	1226.25	13.29	SDR8-O1237664336640016466	0.05	14.86
hs1102+3441	1237.57	12.62	None	0.00	0.00
hs1102+3441	1239.75	12.89	SDR8-O1237665016850219064	0.35	6.50
hs1102+3441	1245.10	13.70	11022+3538	1.30	6.49
hs1102+3441	1251.96	13.15	SDR8-O1237665129610805339	0.29	5.33
hs1102+3441	1262.11	12.80	SDR8-O1237665016849629309	0.37	13.60
hs1102+3441	1263.33	12.71	SDR8-O1237665016849629309	0.37	11.68
hs1102+3441	1264.32	12.78	SDR8-O1237665016849629309	0.37	11.68
hs1102+3441	1269.50	12.91	SDR8-O1237665129611067521	1.31	2.35
hs1102+3441	1272.36	12.60	SDR8-O1237664337175511231	1.04	11.18
hs1102+3441	1274.40	13.77	SDR8-O1237665017386827884	0.88	7.52
hs1102+3441	1288.22	12.94	SDR8-O1237665017386631220	1.79	5.69
hs1102+3441	1295.48	12.78	SDR8-O1237665017386696938	1.90	4.50
mrk421	1227.98	13.25	SDR8-O1237662226208456813	0.08	6.07
mrk421	1239.82	14.39	SDR8-O1237664667365474437	0.20	6.97
mrk421	1246.41	12.74	SDR8-O1237662224060973257	0.28	4.47
mrk421	1247.39	12.46	SDR8-O1237662224060973257	0.28	0.87

Table C.2: A list of all Ly $\alpha$  absorbers and their nearest galactic neighbor (Continued).

QSO Sightline	Absorber Wavelength ( $\text{\AA}$ )	Column Density ( $\text{Log}(N_{HI})$ )	Galaxy Name	Galaxy Luminosity ( $L_*$ )	Distance (virial radii)
pg0832+251	1221.67	13.09	SDR8-O1237674370756313946	0.00	0.96
pg0832+251	1224.53	13.91	SDR8-O1237664668960948568	0.01	2.52
pg0832+251	1230.03	12.98	SDR8-O1237664093972463858	0.06	4.07
pg0832+251	1236.9	18.75	SDR8-O1237664668424274030	0.10	0.09
pg0832+251	1244.00	13.43	08332+2517	1.05	1.13
pg0832+251	1244.89	12.76	08332+2517	1.05	1.13
pg0832+251	1247.00	13.00	SDR8-O1237664668424339577	0.32	2.74
pg0832+251	1247.78	13.02	SDR8-O1237664668424339577	0.32	2.74
pg0832+251	1249.82	14.13	08337+2519	1.25	2.17
pg0832+251	1265.41	13.09	SDR8-O1237664093972398439	0.47	8.71
pg0832+251	1268.16	13.46	SDR8-O1237664093435462023	0.49	4.86
pg0832+251	1274.26	12.82	None	0.00	0.00
pg0832+251	1275.67	12.99	None	0.00	0.00
pg0832+251	1276.42	12.86	SDR8-O1237664092898918802	1.54	10.35
pg0832+251	1281.45	13.38	SDR8-O1237664668961210528	1.57	5.33
pg0832+251	1282.39	14.70	SDR8-O1237664093972398409	0.69	8.84
pg0832+251	1283.34	13.24	SDR8-O1237664093972398409	0.69	8.80
pg0832+251	1292.63	13.04	SDR8-O1237664092898722034	0.88	4.02
pg0832+251	1295.82	12.97	SDR8-O1237664668961079561	2.30	4.86
pg0832+251	1298.33	13.01	SDR8-O1237664092898525529	1.06	7.20
pg0953+415	1222.70	12.46	SDR8-O1237660635456143485	0.00	4.49
pg0953+415	1225.62	12.41	09517+4203	0.08	2.51
pg0953+415	1230.91	12.58	None	0.00	0.00
pg0953+415	1232.33	12.38	SDR8-O1237660343937990679	0.22	6.63
pg0953+415	1234.66	13.22	SDR8-O1237660343937990679	0.22	2.38
pg0953+415	1235.17	13.56	SDR8-O1237660343937990679	0.22	2.38
pg0953+415	1235.78	13.52	SDR8-O1237660343937990679	0.22	2.38
pg0953+415	1239.92	12.87	A095851.35+425921.9	70.32	4.54
pg0953+415	1266.23	12.74	SDR8-O1237660343401119885	0.40	1.14
pg0953+415	1268.93	13.29	SDR8-O1237660343400988821	4.08	2.71
pg0953+415	1270.53	13.33	SDR8-O1237660634918944944	0.90	4.17
pg0953+415	1275.99	12.90	None	0.00	0.00
pg0953+415	1287.10	13.92	SDR8-O1237660635455946846	1.29	2.08
pg0953+415	1293.10	12.64	None	0.00	0.00
pg0953+415	1298.44	14.07	SDR8-O1237660635455815833	1.76	2.22

Table C.3: A list of all Ly $\alpha$  absorbers and their nearest galactic neighbor (Continued).

QSO Sightline	Absorber Wavelength ( $\text{\AA}$ )	Column Density ( $\text{Log}(N_{HI})$ )	Galaxy Name	Galaxy Luminosity ( $L_*$ )	Distance (virial radii)
pg1048+342	1222.08	14.04	N3442	0.49	0.60
pg1048+342	1222.68	14.79	N3442	0.49	0.60
pg1048+342	1223.41	14.03	N3442	0.49	0.60
pg1048+342	1228.02	12.50	None	0.00	0.00
pg1048+342	1232.37	12.47	None	0.00	0.00
pg1048+342	1239.19	12.49	None	0.00	0.00
pg1048+342	1244.98	13.08	SDR8-O1237665017922060475	0.29	6.71
pg1048+342	1258.12	13.65	10475+3353	2.12	4.02
pg1048+342	1266.07	12.79	SDR8-O1237665129609625817	0.01	12.94
pg1048+342	1269.24	13.20	SDR8-O1237664336637132912	2.07	4.93
pg1048+342	1275.86	12.54	A1047+3445	1.18	10.80
pg1048+342	1278.98	13.59	SDR8-O1237664336637198464	2.10	5.07
pg1048+342	1281.22	12.61	SDR8-O1237664336637198456	1.47	5.64
pg1048+342	1285.26	13.61	None	0.00	0.00
pg1048+342	1286.43	12.78	SDR8-O1237665129609691245	4.23	4.83
pg1048+342	1287.67	14.23	SDR8-O1237665129609691245	4.23	1.41
pg1048+342	1290.00	13.03	SDR8-O1237665129609691245	4.23	1.41
pg1048+342	1293.34	12.68	None	0.00	0.00
pg1048+342	1295.24	12.94	None	0.00	0.00
pg1048+342	1299.39	12.77	SDR8-O1237664817669603398	2.56	7.89
pg1115+407	1223.75	13.16	SDR8-O1237664670051336378	0.04	2.41
pg1115+407	1225.81	12.72	SDR8-O1237662226210160806	0.01	4.00
pg1115+407	1225.20	12.57	SDR8-O1237662226210160806	0.01	4.00
pg1115+407	1231.99	12.57	None	0.00	0.00
pg1115+407	1233.50	12.54	None	0.00	0.00
pg1115+407	1234.22	12.74	None	0.00	0.00
pg1115+407	1234.63	12.51	None	0.00	0.00
pg1115+407	1241.70	14.45	11185+4037	0.76	3.45
pg1115+407	1243.62	12.68	11137+4121	0.96	6.56
pg1115+407	1248.29	12.60	SDR8-O1237662194521079980	0.43	12.49
pg1115+407	1251.58	13.29	SDR8-O1237662193984471223	0.71	4.40
pg1115+407	1268.46	12.54	SDR8-O1237661966350942302	0.95	10.81
pg1115+407	1269.69	14.04	SDR8-O1237661966350942302	0.95	10.81
pg1115+407	1278.05	12.56	SDR8-O1237662193984602274	1.31	5.69
pg1115+407	1286.46	12.76	None	0.00	0.00
pg1115+407	1285.87	12.70	None	0.00	0.00
pg1115+407	1289.73	12.97	SDR8-O1237664670051139726	1.99	4.82
pg1115+407	1293.91	13.01	SDR8-O1237664670050943093	0.92	8.26
pg1115+407	1296.69	13.01	SDR8-O1237662226210029694	1.34	10.94

Table C.4: A list of all Ly $\alpha$  absorbers and their nearest galactic neighbor (Continued).

QSO Sightline	Absorber Wavelength ( $\text{\AA}$ )	Column Density ( $\text{Log}(N_{HI})$ )	Galaxy Name	Galaxy Luminosity ( $L_*$ )	Distance (virial radii)
pg1116+215	1221.68	13.34	11111+2148	0.04	3.50
pg1116+215	1225.25	12.79	A1121+1932	0.00	1.81
pg1116+215	1235.49	13.41	N3650	0.88	4.54
pg1116+215	1239.25	12.85	SDR8-O1237667734502899919	0.10	5.30
pg1116+215	1239.69	12.95	SDR8-O1237667734502899919	0.10	5.30
pg1116+215	1250.06	13.79	A1116+2118A	0.05	15.85
pg1116+215	1254.83	13.37	SDR8-O1237667782291620073	0.38	1.90
pg1116+215	1266.11	12.87	PROCHASKA-12-2663	0.41	1.55
pg1116+215	1265.63	13.17	PROCHASKA-12-2663	0.41	1.55
pg1116+215	1269.57	12.82	None	0.00	0.00
pg1116+215	1276.43	12.62	SDR8-O1237667781218074695	0.73	11.62
pg1116+215	1279.17	12.84	None	0.00	0.00
pg1116+215	1283.72	12.66	None	0.00	0.00
pg1116+215	1287.28	13.59	PROCHASKA-12-2071	0.12	0.82
pg1116+215	1288.85	12.93	PROCHASKA-12-2071	0.12	0.82
pg1116+215	1289.45	13.14	PROCHASKA-12-2071	0.12	0.82
pg1116+215	1291.68	12.73	PROCHASKA-12-674	0.12	8.18
pg1121+422	1225.25	13.24	SDR8-O1237661966888468671	0.05	3.53
pg1121+422	1226.21	13.26	SDR8-O1237661871325380682	0.02	4.72
pg1121+422	1226.61	12.82	SDR8-O1237661871325380682	0.02	4.72
pg1121+422	1227.84	13.03	SDR8-O1237661966889058401	0.10	4.22
pg1121+422	1228.49	12.84	SDR8-O1237661966889058401	0.10	4.22
pg1121+422	1233.34	13.39	None	0.00	0.00
pg1121+422	1244.65	13.58	SDR8-O1237662195058868398	0.18	0.69
pg1121+422	1245.46	14.23	SDR8-O1237662195058868398	0.18	0.69
pg1121+422	1248.85	13.20	SDR8-O1237661966888665106	0.37	7.04
pg1121+422	1256.78	13.77	SDR8-O1237661967962538112	0.58	0.95
pg1121+422	1263.83	12.86	None	0.00	0.00
pg1121+422	1269.98	13.37	SDR8-O1237661967962538029	1.80	2.46
pg1121+422	1273.48	12.92	None	0.00	0.00
pg1121+422	1280.84	12.90	1WGAJ1123.9+4135	1.44	6.27
pg1121+422	1286.30	12.73	SDR8-O1237661967425732746	1.15	5.46
pg1121+422	1288.83	13.69	SDR8-O1237662194522062944	0.86	7.32
pg1121+422	1290.76	13.58	None	0.00	0.00
pg1121+422	1296.85	13.16	SDR8-O1237662195059064962	2.49	6.32
pg1121+422	1297.41	13.19	SDR8-O1237662195059064962	2.49	6.32

Table C.5: A list of all Ly $\alpha$  absorbers and their nearest galactic neighbor (Continued).

QSO Sightline	Absorber Wavelength ( $\text{\AA}$ )	Column Density ( $\text{Log}(N_{HI})$ )	Galaxy Name	Galaxy Luminosity ( $L_*$ )	Distance (virial radii)
ton236	1223.82	13.23	A1528+2726	0.00	0.61
ton236	1225.24	13.24	A1528+2726	0.00	0.61
ton236	1232.64	13.49	None	0.00	0.00
ton236	1239.44	13.19	A1531+2818	0.55	7.02
ton236	1243.77	12.67	A1523+2920A	0.00	1.67
ton236	1258.61	13.31	SDR8-O1237662661603295421	1.04	2.43
ton236	1270.50	13.59	SDR8-O1237664854187639069	0.57	0.87
ton236	1279.25	12.79	None	0.00	0.00
ton236	1280.34	13.41	None	0.00	0.00
ton236	1282.66	13.65	None	0.00	0.00
ton236	1288.17	13.08	SDR8-O1237662661603164336	3.62	6.04
ton236	1293.02	12.95	SDR8-O1237664854187638981	0.98	1.98
ton236	1295.24	13.23	SDR8-O1237664854187639073	0.92	1.95
ton236	1294.24	14.01	SDR8-O1237664854187639073	0.92	1.95
ton580	1225.73	13.46	SDR8-O1237665330921799876	0.05	6.33
ton580	1232.57	12.77	None	0.00	0.00
ton580	1244.30	12.89	SDR8-O1237665329311449175	0.36	9.62
ton580	1249.16	13.14	SDR8-O1237667212672565373	0.62	9.24
ton580	1279.42	12.98	SDR8-O1237665367435051112	1.79	3.86
ton580	1284.68	13.18	SDR8-O1237665329311121511	0.79	7.24
ton580	1286.41	12.78	SDR8-O1237665367972249713	1.93	6.95
ton580	1295.36	13.33	None	0.00	0.00